Climate Variability of the Mid and High Latitudes of the Southern Hemisphere in Ensemble Simulations from 1500 to 2000 AD

Master Thesis

Faculty of Science
University of Bern

presented by
Sophie-Berenice Wilmes
June 2011

Supervisor:
PD Dr. Christoph C. Raible
Co-Supervisor:
Prof. Dr. Thomas F. Stocker

Climate and Environmental Physics
Institute of Physics of the University of Bern
Oeschger Centre for Climate Change Research, University of Bern

Abstract

Little is known about climatic changes in the Southern Hemisphere during the last millenium in comparison to the Northern Hemisphere due to the lack of reliable proxy records. Nevertheless, the available records point towards significant fluctuations in both temperature and precipitation occurring during the last millennium. Besides the climate proxy records/reconstructions, simulations of the past using coupled climate models provide a good opportunity for exploring these variations and distinguishing between impacts of external forcing and changes in internal variability and links between the two. Here, the focus is laid on the mid and high latitudes of the Southern Hemisphere as these are areas in which feedbacks with global impacts can occur.

In this study an ensemble of 4 transient simulations over the last 500 years from an atmosphere ocean general circulation model, i.e., Climate Community System Model (Version 3; CCSM3), is analyzed. The model is forced with solar irradiance, greenhouse gas (GHG) and volcanic aerosol reconstructions. The simulations only deviate in their initial conditions. The model's ability to simulate present day Southern Hemisphere climate is presented by comparing a control simulation with constant forcing at 1990 AD levels to reanalysis data from the ECMWF (ERA40).

Using the ensemble of transient simulations the Southern Hemispheric climate variations of the past millennium are investigated. For this, three different approaches are taken:

Firstly, we investigate changes in the leading atmospheric modes of internal climate variability - the Southern Annular Mode (SAM), the South Pacific Dipole (SPD), the Zonal Wave 3 (ZW3) and the El Niño - Southern Oscillation (ENSO) - and evaluate their temporal evolution and their impacts on regional climate, especially in the light of the varying external forcing. It can be seen that the SPD, ZW3 and ENSO variability remain stable whereas SAM shows a significant shift towards its positive state during the 20th century with possible influences on the strength of the Agulhas leakage. Furthermore, it can be seen that the teleconnection patterns, i.e. their relationship to temperature and precipitation, of all modes remain stable over time, thus, opening up possibilities for the reconstruction of these modes.

In a second step, a bottom-up approach is taken and investigated how temperature and precipitation in specific (proxy related) areas (e.g., South America, Australia, and South Africa) change over time and the underlying dynamics of the changes are evaluated. The results show that regional temperatures are strongly influenced by changing GHG concentrations and volcanic eruptions whereas precipitation shows no significant response to the varying external forcing. This stands in contrast to proxy records suggesting that significant changes in SH climate occurred during the last 500 years which were not directly related to changes in the external forcing. The underlying dynamics of the temperature changes generally point to a combination of several modes, thus, hampering the possibility for a regional reconstruction of one of the modes from proxy records.

Thirdly, the impact of the varying external forcing on mean climate in the Southern Hemisphere is analyzed. As expected an increase in the forcing corresponds to an increase in both surface and sea surface temperatures. Also, an increase in geopotential height at the 850 hPa level is found resulting in the positive trend in the SAM index. The changes in the mid latitude westerlies with increasing forcing are negligible, thus not corresponding with observations during the last 30 years. In particular, over the mid and high latitude land masses of the Southern Hemisphere precipitation is increased.

Contents

Chapter 1

Introduction

Present-day climate in the mid and high latitudes of the Southern Hemisphere is characterized by a high diversity of weather and climate patterns due to the considerable meridional extent of the landmasses of South America, Africa and Australia. The variability of the climate in this area on interannual to interdecadal scales is not only a result of distinct topographical features such as the Andes Cordillera, or the large water masses of the Southern Ocean, but also of a superposition of various tropical, subtropical and extratropical atmospheric variability patterns.

1.1 Present day climatic features of the Southern Hemisphere mid and high latitudes

One of the most important features of the Southern Hemisphere mid and high latitudes is the Southern Annular Mode (SAM), also known as the Antarctic Oscillation, which appears as the leading mode of low frequency variability in the troposphere between 20°S and 90°S [*Kidson*, 1999; *Thompson and Wallace*, 2000]. This mode of the extratropical circulation shows an approximately zonally symmetric structure and represents fluctuations in both the strength and location of the mid latitude westerly winds and hence shifts in atmospheric mass between the low and high latitudes. A positive (negative) SAM index is associated with negative (positive) pressure anomalies over Antarctica and positive (negative) anomalies over the mid latitudes and thus stronger (weaker) circumpolar westerlies [*Thompson and Wallace*, 2000]. The change in phase generally occurs around 45°S (a southward shift to 60°S can be seen around the Drake Passage) and centers of action generally appear over the midlatitude Atlantic, Pacific and Indian Oceans. Due to its hemispheric nature, SAM shows impacts on various aspects of Southern Hemisphere climate such as temperatures over Antarctica [*Kwok and Comiso*, 2002; *Marshall*, 2007], temperatures and precipitation in the mid latitudes of the Southern Hemisphere [*Gillett*, 2006; *Jones and Widmann*, 2003] and the sea ice - ocean system [*Lefebvre and Goosse*, 2005] through changes in strength of the westerly winds and altered storm tracks [*Marshall et al.*, 2006]. Recently, a positive trend in the Southern Annular Mode has been observed for the last three decades of the twentieth century [*Marshall*, 2003] which has been attributed to the changes in both ozone and greenhouse gases [*Thompson and Solomon*, 2002; *Arblaster and Meehl*, 2006].

Variability in the tropics is dominated by the El Niño - Southern Oscillation (ENSO), a coupled atmosphere-ocean phenomenon rooted in the tropical Pacific. It is characterized by fluctuations between its positive (El Niño) and negative (La Niña) state occurring on timescales of 2-7 years. A full review on ENSO can be found in *Diaz and Markgraf* [1992]. ENSO is associated with changes in the Walker circulation making up the atmospheric component of this mode and changes in SST as the oceanic component. During an El Niño event the trade winds which are part of the Walker Circulation weaken which results in reduced upwelling of cold and nutrient rich water off the west coast of South America. The overall pattern of this event is associated with a warming of these regions and hence increased convection and precipitation during this phase in the northern and south-eastern parts of South America. In contrary, Indonesia and Australia generally experience dryer conditions due to large scale subsidence over the western Pacific. During a La Niña event the opposite changes can be observed. However, not only changes in the tropics but also anomalies in the mid and high latitudes can be seen as indirect effects through atmospheric teleconnections. For example, in southern Chile ENSO causes precipitation anomalies which are related to a decrease in storm frequency and an increase in blocking events in the South Pacific [*Montecinos et al.*, 2000]. Also, ENSO appears to modify several atmospheric variability modes such as the Pacific decadal oscillation (PDO), the Pacific North American Pattern (PNA) (both not considered in this study), and the South Pacific Dipole (SPD).

The South Pacific Dipole (SPD), also known as the Pacific South America teleconnection, is the dominating mode of climate variability in the extratropical South Pacific. It is associated with three alternating centers of pressure anomalies in the south Pacific, the polar southeast Pacific, and polar South Altlantic [*Yuan and Li*, 2008]. It has been suggested that it is part of a Rossby wave train originating in the tropics which is driven by changing tropical convection, especially due to ENSO [*Kiladis and Mo*, 1998; *Garreaud and Battisti*, 1999]. Increased SST during an El Niño event strengthen tropical convection and enhance the meridional temperature gradient which results in an contraction and strengthening of the Hadley Cell. This leads to a southward shift of the westerlies over the South Pacific, so that during the positive phase of ENSO the SPD pattern generates a persistent high pressure anomaly in the Amundsen Sea and a negative anomaly arises over the Weddell Sea [*Rind*, 2002]. During a La Niña event anomalies of the opposite sign prevail. Climatic effects related to this teleconnections pattern are precipitation variations over New Zealand, alterations in the type and frequency of blocking events over the polar South Pacific. Also the SPD has a significant effect on creating the anomalies in sea ice concentrations with opposite signs in the Weddell and Ross Seas [*Renwick and Revell*, 1999; *Kwok and Comiso*, 2002; *Renwick*, 2002].

The Zonal Wave 3 (ZW3) is associated with the meridional component of the mostly zonally symmetric atmospheric circulation in the mid and high latitudes of the Southern Hemisphere. The ridges and rests are quasi-stationary with the ridges located downstream of the midlatitude continents [*van Loon and Jenne*, 1972]. The ZW3 shows considerable variability on daily [*Kidson*, 1999], seasonal and interannual timescales [*Karoly*, 1989], and has been associated with blocking events on the longer timescales [*Trenberth and Mo*, 1985]. Because of its relation to the meridional transport in the Southern Hemisphere it plays an important role in the north/south transport of heat through the atmosphere [*Raphael*, 2004]. A link between the ZW3 and Antarctic sea ice concentrations has been reported by several studies [*Raphael*, 2007; *Holland et al.*, 2006].

Next to the atmospheric variability, of course, variability of the ocean system also plays an important role. In this respect the Southern Ocean has a unique role in the global climate system as is the only ocean through which the Atlantic, the Pacific and the Indian Ocean are connected. The Antarctic Circumpolar Current (ACC) is the predominant current system of the Southern Ocean and is known as the "mightiest current system of the world" [*Pickard and Emery*, 1992] transporting more water than any other current. The mean transport through the Drake Passage has been estimated at 134±13 Sv [*Whitworth*, 1983; *Whitworth and Peterson*, 1985]. An important feature of the Southern Ocean is the absence of continental boundaries at its northern margin preventing a net meridional geostrophic flow across the mid latitudes. Tilted isopycnals bring mid depth waters in contact with the ocean surface. Waters mix preferentially along lines of equal density, thus these two effects isolate the Antarctic continent to some extent from the climate variability of the mid and low latitudes and prevent heat exchanges between the tropics and the pole, thus contributing to Antarctica's glacial climate [*Rintoul et al.*, 2001; *Gille*, 2002].

Three main effects of the ACC on climate have been noted. Firstly, it links the three major oceans and thus contributes the redistribution of heat and other properties between them. Secondly, due to the tilted isopycnals, cold Antarctic surface waters reach the deep ocean and thus contribute to the renewal of deep water. Thirdly, the Southern Ocean is a major reservoir for both heat and carbon which is in exchange with the atmosphere and can thus, contribute to changes in global climate by the uptake or release of carbon [*Russell et al.*, 2006].

A further important current in the mid-latitude Southern Hemisphere ocean systems with implications for the global climate system is the Agulhas current which is the major western boundary current of the Southern Hemisphere [*Lutjeharms*, 2006]. It is an important part of the global overturning circulation controlling the return flow of warm and saline waters into the Atlantic Ocean occurring as the Agulhas leakage [*Gordon*, 1986]. The Agulhas leakage results from a complex non-linear interplay between the Aguhlas current, vigorous mesoscale features in its source regions and south of Cape Horn where large parts of the Agulhas current waters are retroflected back into the Indian Ocean. Two main mechanisms have been proposed by which the Agulhas leakage can affect the Atlantic meridional overturning circulation (AMOC). Firstly, wave processes induced through the mesoscale activity in the retroflection area can dynamically modify the AMOC on decadal timescales [*Biastoch et al.*, 2008]. Secondly, salinity anomalies being advected northward through the Atlantic may influence deep water formation in the high-latitude North Atlantic [*Weijer et al.*, 2002], thus possibly inducing changes that by far exceed regional significance.

1.2 Past climate variations

Climate throughout the Holocene, i.e. the present interglacial from $\sim 11,600$ years BP (before present) [*Wanner et al.*, 2008], appears more stable than during the last ice age; nevertheless significant fluctuations can be seen during the last 10,000 years in, for example, temperature records from Antarctica on timescales from decades to millennia [*Masson et al.*, 2000], inter alia, induced by changes in orbital geometry and global ice mass. When restricting the attention to the last millennium these boundary conditions did not change to a great extent thus suggesting that internal variability played a more significant role during this

period before the influence of humans became noticeable [*Jones and Mann*, 2004]. Thus this period provides the opportunity of placing the recent global climatic change into a longer term context and evaluating the impact of both the anthropogenic external forcing (increase in human-generatred greenhouse gasses (GHG) and aerosol mass concentrations) and the natural external forcing (variations in insolation and volcanic eruptions). Focusing on this period permits the comparison with recently established high-resolution archives of climate variability such as presented in *Jones et al.* [2001]. This study shall focus on the latter half of the past millennium. This period is marked by several pronounced solar minima such as the Maunder Minimum around 1700 AD and the Dalton Minimum around 1800 AD and the significant increase in greenhouse gas concentrations beginning at the end of the 18th century.

Little is known about climatic changes in the Southern Hemisphere during the last millennium in comparison to the Northern Hemisphere due to the low density of proxy records in this area [*Villalba et al.*, 2009]. Nevertheless, the few available records point towards significant fluctuations in both temperature and precipitation occurring during this time period [*Jones and Mann*, 2004; *Masiokas et al.*, 2009; *Tonello et al.*, 2009]. Recently, a first attempt to reconstruct patterns for Southern South America was presented by *Neukom et al.* [2010]. They find cold summer conditions between 1350 AD and 1700 AD which is followed by a relatively warm period up to 1850 AD when shift to colder temperatures occurred. The reconstructed winter temperatures generally lie below the 20th century level. Their precipitation reconstructions show a show a trend to dryer condition during the winter months for the past centuries whereas for the summer less spatial coherency and more variability is present. Thus these reconstructions point to a number of climatic variations occurring during this time period.

Besides the climate proxy records/reconstructions, simulations of the past using coupled climate models provide a good opportunity for exploring these variations and distinguishing between impacts of external forcing and changes in internal variability and links between the two [*Yoshimori et al.*, 2005; *Raible et al.*, 2006]. This study shall focus on the mid- and high-latitudes because changes in the atmospheric circulation in this region also show feedbacks to the ocean circulation and sea ice distribution and hence exceed regional importance [*Lefebvre et al.*, 2004; *Biastoch et al.*, 2009].

1.3   Relevance

Understanding past changes in climatic patterns and the dynamics behind them is key to assessing the possible changes taking place in the future [*Jansen et al.*, 2007] and providing high quality advice to societies for mitigation. For this it is important to gain knowledge how past changes in external forcing impacted on both the global mean climate but more importantly the regional climate as it is the regional climate that is critical for ecosystem dynamics and human societies. Past examples show that changes in e.g. precipitation can have catastrophic impacts on highly developed societies as was suggested for seen for the Mayas around 900 AD [*Haug et al.*, 2003] and other cultures. Improved knowledge about the internal dynamics of the climate system and the impact of the external forcing also helps improve the model physics and, hence, contributes to better projections of future climate.

1.4   Aims of the study

In this study an ensemble of 4 transient simulations over the last 500 years from an atmosphere ocean general circulation model, i.e., the Climate Community System Model (Version 3; CCSM3), is analyzed. The model is forced with solar irradiance, greenhouse gas and volcanic aerosol reconstructions (details can be found in *Hofer* [2010]). The simulations only differ in their initial conditions. The model's ability to simulate present day Southern Hemisphere climate is presented by comparing a control simulation with constant forcing at 1990 AD levels to reanalysis data from the ECMWF (ERA40).

Using the ensemble of transient simulations the Southern Hemispheric climate variations of the past millennium are investigated. For this, three different approaches are taken: Firstly, changes in the leading atmospheric modes of internal climate variability - the Southern Annular Mode (SAM) [*Thompson and Wallace*, 2000], South Pacific Dipole (SPD) [*Kiladis and Mo*, 1998] and the Zonal Wave 3 [*Raphael*, 2004] - are investigated and their temporal evolution and their impacts on temperature and precipitation signals, especially in the light of the varying external forcing are evaluated. In addition it is analyzed whether changes in the oceanic circulation, namely the ACC and the Agulhas current occur and how Antarctic sea ice concentrations evolve. In a second step, a bottom-up approach is taken and it is investigated how temperature and precipitation in specific, proxy covered areas (e.g., South America, Australia, and South Africa) are linked to the large-scale atmospheric circulation and in which regions temperature and precipitation variations may provide potential for reconstructing SAM, SPD and ZW3. Thirdly, it is analyzed which areas of the mid- and high-latitudes in the Southern Hemisphere are most sensitive to the external forcing. For this a similar technique as *Yoshimori et al.* [2005] used is applied, and it is explored in which areas the signal-to-noise (external forcing-to-internal variations) ratio is largest and significant. The focus shall lie on temperature and moisture changes, as these are the variables most strongly affecting both ecosystems and human societies [*Parry et al.*, 2007] and have the potential to be related to proxy archives.

Chapter 2

Model and experimental design

This chapter provides detailed information on the climate model that was used to perform a set of experiments, namely simulations with both perpetual and time varying external forcing, which shall also be introduced in the following sections. Furthermore, the observational data shall be described and problems arising from these data sets will be pointed out. In the last section a set of methods used in this study shall be introduced.

2.1 Model description

The simulations were performed with the fully coupled Community Climate System Model Version 3.0.1 (CCSM3) which was developed at the National Centre for Atmospheric Research (NCAR). The code and information about the model are freely available from the CCSM website (http://www.ccsm.ucar.edu/models) and a detailed description of the model can be found in *Collins et al.* [2006]. The general circulation model consists of four components for the atmosphere, ocean, sea ice, and land surface, which are connected by a coupler (CCSM Coupler Version 6.0) through which fluxes and state information are exchanged. No flux corrections are applied. The model can be run in a variety of resolutions and multiple combinations of resolutions are possible between the different components. The three most commonly used settings which have also been physically evaluated are a low resolution (T31x3), a medium (T42x1) and a high resolution (T85x1) version. In this study the low resolution configuration was chosen.

The atmosphere component which is based on the primitive equations is the Community Atmosphere Model Version 3.1 (CAM3). The atmospheric general circulation model CAM3 consists of a Eulerian dynamical core which is based on the hydrostatic primitive equations, and is coupled to sub-grid scale parametrizations of physical processes such as boundary layer turbulence, gravity wave drag, or reflection and absorption of long and short wave radiation. The model applies a triangular spectral truncation at 31 wave numbers (T31) which corresponds to a resolution of approximately $3.75° \times 3.75°$ in latitude and longitude, respectively, and 26 unevenly spaced hybrid sigma-pressure levels in the vertical, ranging up to 2.9 hPa. The hybrid grid is a pure, terrain following sigma level at the ground, above 83 hPa coordinates purely follow pressure level, and in the middle of the atmosphere a transition between both schemes is used. Time discretisation is performed with both semi-implicit Eulerian and semi-implicit semi-Lagrangian schemes.

The land surface model in CCSM3, the Community Land Model (CLM3), is integrated on the same horizontal grid as the atmospheric component, and each grid box is subdivided into hierarchies of land types (glacier, wetland, lake, urban, and vegetated), soil columns, and plant types. CLM3 calculates moisture and temperature in 10 vertical levels of the soil column; furthermore, up to five separate snow height dependent levels for snow cover can be resolved. River run-off is implemented into the land model via a separate river transport model on an independent higher resolution grid ($0.5° \times 0.5°$).

For the ocean the Parallel Ocean Program Version 1.4.3 (POP) which was developed at the Los Almos National Laboratory is implemented into CCSM. The ocean dynamics are based on the primitive equations which are implemented with the hydrostatic and Bousinesq approximations. Horizontal mixing is parametrised with the Gent-McWilliams isopycnal formulation, vertical mixing is quantified using the K-profile. The model uses a semi-analytic grid: in the northern hemisphere an irregular displaced-pole grid is implemented in which the North Pole is shifted to lie over Greenland; at the equator this then is joined smoothly to the standard Mercator grid in the southern hemisphere. POP has $3.6°$ resolution in longitude and a latitudinal resolution which ranges from $0.6°$ in the tropics and over Greenland to $2.8°$. In the vertical 26 levels are resolved, whose thicknesses increase from 8 m at the sea surface to 500 m in the deep ocean which has a maximum depth of 5000 m.

The sea ice model in CCSM3 is the Community Sea Ice Model Version 5 which runs on the same grid as the ocean model. It is a dynamic-thermodynamic model which combines energy-conserving thermodynamics with ice dynamics which are calculated based on the principles of elastic-viscous-plastic rheology. The model distinguishes five different ice-thickness categories which are further subdivided into four equally spaced layers in order to calculate vertical heat conduction.

2.2 Experimental design

For this and further studies [*Yoshimori et al.*, 2010; *Hofer et al.*, 2011] two types of simulations were performed: equilibrium simulations with constant external forcing and transient runs with time varying forcing. The equilibrium simulations are used in order to give the initial conditions for the transient simulations and to generate a reference state for a stable climate; whereas the transient simulations are used to evaluate the effects and feedbacks of variations in the external forcing on the climate system. For the subsequent analysis only monthly averaged data is considered. An overview of all experiments conducted can be found in Table 2.1.

2.2.1 Control experiments

Two control experiments were integrated for the study: one integration with constant external forcing corresponding to levels at 1990AD (CTRL1990) in order to evaluate the model performance for present day climate (a detailed analysis of the 1990 CTRL is carried out by *Yeager et al.* [2006]), and a simulation with an external forcing at 1500AD levels. For the CTRL1990 the present day control simulation performed by the NCAR with forcing levels according to 1990AD conditions was extended by several decades. The CTRL1500 run was branched from the extended CTRL1990 simulation. In order to allow for adjustments to the

Table 2.1: Overview of the simulations used in this study.

Simulation	Length (yrs)	Description
CTRL1990	480	Control simulation with constant external forcing at 1990AD levels
CTRL1500	652	Control simulation with constant external forcing at 1500AD levels
TR01 TR02 TR03 TR04	598	Transient simulations with time-varying external forcing ranging from 1500AD to 2098AD

changes in the external forcing, and climate to reach a stable state, the first 50 years of the CTRL1500 simulations are not used for analysis. Nevertheless, the simulation still shows a drift towards a colder climate which corresponds to an approximately linear trend in the atmosphere and at the sea surface sea surface and exhibits a decrease in strength over time in the deep ocean [*Hofer*, 2010]. In order to minimize the effect of the trends all variables are detrended using a least-squares quadratic fit (see section Handling of Trends for more details).
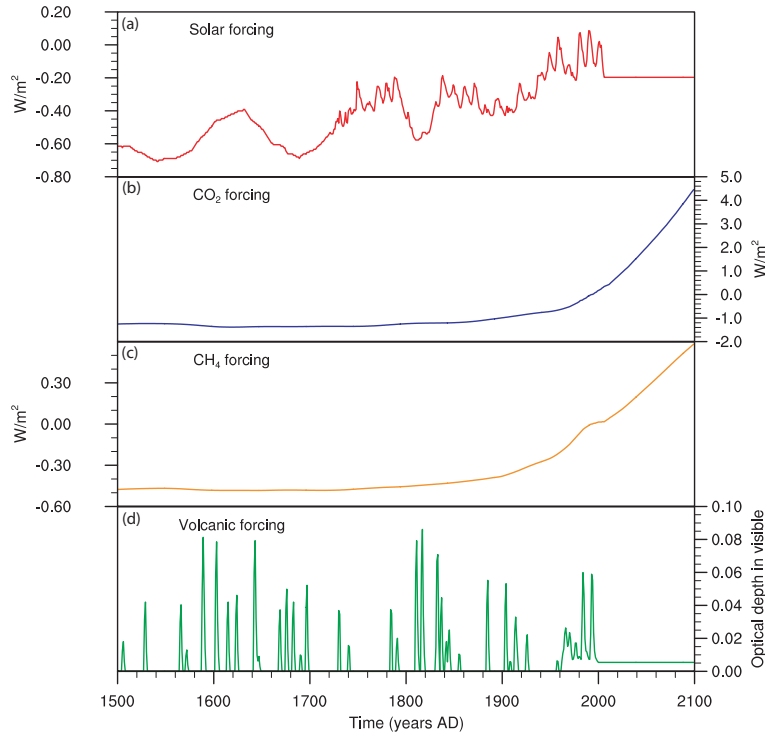
2.2.2 Transient simulations

In addition to the perpetual CTRL1990 and CTRL1500 simulations an ensemble of four transient simulations (TR01 through to TR04) with time varying forcing from 1500 to 2100 was conducted. The simulations were branched from different starting years within CTRL1500 in order to give different initial conditions at 1500AD for the TR1500 simulations. They are driven with reconstructions of the natural forcing which consists of solar irradiance variations, volcanic eruptions and greenhouse gasses for 1500AD to 2000AD; from 2000AD to 2098AD forcing was applied according to the IPPC SRES A2 scenario. The main natural and anthropogenic forcing are summarized in Figure 2.1.

For the solar forcing an updated [*Crowley*, 2000] reconstruction of net radiative forcing scaled to the *Lean et al.* [1995] timeseries was used. This record combines data on faculae darkening from the Greenwich Observatory back to 1884 with historical sun spot observations prior to this data. The timeseries was extended back to 1000AD by *Crowley* [2000] by splicing in estimates of solar irradiance variations which are based on fluctuation of the cosmogenic isotopes ^{10}Be and ^{14}C measured in ice cores and tree rings. It was scaled to fit the solar irradiance reconstruction L_{net} by *Lean et al.* [1995] using the following relation:

$$S = 1365.0635 \text{W m}^{-2} + 5.399 \cdot L_{net}. \tag{2.1}$$

As the *Lean et al.* [1995] reconstructions end in 1998AD, Active Cavity Radiometer Irradiance Monitor composite data [*Fröhlich and Lean*, 2004] was implemented for the subsequent 7 years. After 2006AD the solar forcing was kept constant at 1366.676 W m^{-2}.

Figure 2.1: Natural and anthropogenic forcing from 1500AD to 2100AD used for the transient simulations. (a) Solar irradiance changes according to [*Crowley*, 2000] scaled to the *Lean et al.* [1995] reconstruction, (b) CO_2 variations reconstructed by *Etheridge et al.* [1996], (c) CH_4 variations by *Blunier et al.* [1995], and (d) volcanic forcing shown as variations in optical depth (*Crowley* [2000] scaled to *Ammann and Naveau* [2003]).

Volcanic forcing is introduced by converting the volcanic forcing estimates by *Crowley* [2000] into aerosol mass distributions. This is done by applying a linear regression between *Crowley* [2000] and *Ammann and Naveau* [2003] for the six strongest eruptions from 1870AD to present. As the focus is lain on tropical eruptions the calculated total aerosol masses are distributed throughout the lower stratosphere using a latitudinal cosine weighting function in order to achieve highest concentrations at low latitudes. As the exact date of the eruption is not known for the majority of cases the volcanic aerosols are added throughout the entire year of the eruption. From the year 2000AD onwards no artificial volcanic activity is introduced, however, the total aerosol optical depth in the visible band is kept stable at a value of 0.00054.

The greenhouse gas forcing timeseries consisting of CO_2, CH_4 and N_2O originate from ice core reconstructions carried out by *Etheridge et al.* [1996], *Blunier et al.* [1995], *Flueckiger et al.* [1999] and *Flueckiger et al.* [2002] which were smoothed by a spline interpolation. For the time period 1970AD to 2005AD direct atmospheric measurements [*Dlugokencky et al.*, 2003; *Keeling*, 2005; *Thompson et al.*, 2004] are used, thereafter the greenhouse gas concentrations follow the IPCC SRES A2 scenario [*Nakicenovic et al.*, 2000].

2.3 Observational data

In addition to the data obtained from the CCSM3 simulations, also observational data is considered to evaluate the performance of the model for present day climate. For the atmosphere, reanalysis data from the ECMWF ERA-40 project is used for comparison; for sea ice and sea surface temperature, records obtained by the Met Office Hadley Centre are selected.

2.3.1 ECMWF ERA-40 data

The ECMWF ERA-40 reanalysis data set covers the time period from 1958AD to 2002AD and combines both observations and numerical weather prediction model output to a global data coverage. On the one hand this allows a uniform data coverage over the globe but also opens the possibility to obtain variables previously not measured. To obtain the reanalysis data the technique of data assimilation is applied: the meteorological forecast model is run for short time periods, usually six hours, and the output of each cycle is taken together with the set of observations valid for this specific point in time and assimilated to obtain a representation of the current conditions as accurate as possible. This analysis is then used as the initial condition of the next short-range forecast. The data assimilation scheme takes both errors in the model formulation as also in the observed values to minimise errors in the reanalysis. This procedure leads to a 'best fit' between model and observations. The set of initial conditions can subsequently be used as a record of meteorological conditions over the analysis period [*Uppala et al.*, 2005].

Here, monthly means of the ECMWF ERA-40 data are used. The data is interpolated to a resolution of 2.5° × 2.5° in latitude and longitude and is available for 23 pressure levels throughout the atmosphere (from 1000hPa at the surface up to 1hPa at the top of the atmosphere) on the ECMWF website (http://data-portal.ecmwf.int/data/d/era40_moda/).

2.3.2 Hadley Centre SST and SIC data

Data on sea surface temperature (SST) and sea ice concentration (SIC) were taken from the HadSST1 compilation [*Rayner et al.*, 2003]. Both have a resolution of 1° × 1° in latitude and longitude and span the time period 1870AD to 2010AD. The datasets were obtained by combining gridded observational datasets, removing systematical biases and then, for data sparse areas, applying the reduced space optimal interpolation (RSOI), an EOF-based technique in two steps. In the first stage long-term change patterns are reconstructed, in a second step the focus is laid on the residual interannual variability.

As both the ERA-40 and the Hadley Centre data sets are based on sparse observations in the Southern Hemisphere, especially at the beginning of the compilations, and previous studies, [*Bromwich and Fogt*, 2004] have shown large biases in these regions prior to satellite observations, the use of these two data sets is restricted to 1978AD to 2000AD.

2.4   Methods and Tools

2.4.1   Handling of Trends

Even though time was allowed for the CTRL1500 which was branched from the perpetual CTRL1990 simulation to adjust to the changes in the external forcing, the CTRL1500 still exhibits a trend which is approximately linear for the atmosphere and sea surface temperature, and is converging in the deep ocean. In order to reduce the effect of the trend both the CTRL1500 and the transient simulations are detrended. For this a quadratic least-squares fit was removed which yielded good results for both the atmosphere and ocean. In a first step the trend was calculated for the CTRL1500 simulation for each month and variable separately; secondly this trend was subtracted from each of the respective variables for the respective month. More details and information on the procedure can be found in *Hofer et al.* [2011].

2.4.2   EOF analyis

One frequently used method to analyse large data sets is empirical orthogonal function (EOF) analysis, also known as principle component analysis (PCA). The data is converted into a number of orthogonal, and hence uncorrelated principle components using orthogonal transformation. The conversion is carried out such that the first EOF or principle component explains the highest amount of variance within the dataset, the second less, the third even less and so forth. EOF analysis thus provides a tool for analysing the main variability found in a data set and allows to explore its temporal evolution. Algebraically, EOF can be considered as particular linear combinations of p random variables $X_1,...,X_p$. In a geometrical space, the coordinate system is rotated such that the linear combinations $Y_1,...,Y_p$ are selected as new coordinate axes. The new axes point into the direction with maximum variability and represent a more simple way of representing the sample covariance structure. Consider the random vector

$$\boldsymbol{X}' = (X_1,...,X_p) \tag{2.2}$$

which has the associated covariance matrix Σ with the corresponding eigenvalue-eigenvector pairs $(\lambda_1, e_1),\ldots,(\lambda_p, e)$ where $\lambda_1 \geq \cdots \geq \lambda_p \geq 0$. The i-th principle component is given by

$$Y_i = e'_i \boldsymbol{X} = \sum_{j=1}^{p} e_{i,j} X_j, \qquad i = 1,\ldots,p. \tag{2.3}$$

Hence, variance and covariance of Y_i are given by

$$Var(Y_i) = e'_i \, \Sigma \, e_i = \lambda_i, \qquad i = 1,\ldots,p \tag{2.4}$$

$$Cov(Y_i, Y_k) = e'_i \Sigma \, e_k = 0, \qquad i \neq k \tag{2.5}$$

The proportion of total population variance explained by the k-th principle component is calculated by

$$\frac{\lambda_k}{\sum_{i=1}^{p} \lambda_i}, \qquad k = 1,\ldots,p. \tag{2.6}$$

If a large proportion of the total sample variance for large p can be attributed to the first one, two or three EOFs, they may replace the original p variable as a reasonable approximation.

2.4.3   Determination of Significance

In order to determine whether correlation and regression coefficients obtained during analysis differed significantly from zero following significance tests were carried out:

Correlation

If two samples within a general population X and Y have a true correlation of $\rho = 0$, and the sample size N is equal or greater than 6, then r is related to t as

$$t = r/\sqrt{(1 - r^2)/(N - 2)}. \tag{2.7}$$

t follows a t-distribution with $N - 2$ degrees of freedom. Thus, this formulae can be applied to test whether a correlation coefficent comes from a population where $\rho = 0$. The formulae is solved for the appropriate N and the associated critical value of t for the chosen confidence level (e.g. $\alpha = 0.05$) can be found.

Regression

After carrying out a regression it is necessary to determine whether the slope B_1 of the regression line

$$Y = B_0 + B_1 X \tag{2.8}$$

where where B_0 is the intercept, B_1 is the slope (also called the regression coefficient), X is the value of the independent variable, and Y is the value of the dependent variable, differs significantly from zero. Here, this is done with a t-test. The t-score of the slope is calculated as

$$t = B_1/SE \tag{2.9}$$

where SE is the standard error of the regression line. SE is computed as

$$SE = sqrt\sum (y_i - \hat{y}_i)^2/(n - 2)/\sqrt{\sum (x_i - \bar{x})^2} \tag{2.10}$$

where y_i is the value of the dependent variable for observation i, $\hat{y}_i$ is estimated value of the dependent variable for observation i, x_i is the observed value of the independent variable for observation i, $\bar{x}$ is the mean of the independent variable, and n is the number of observations. The probability of the regression coefficient belonging to a slope that does not differ from zero can now be evaluated with a t-distribution. In this study, a significance level of $p = 0.05$ was chosen.

2.4.4   Spectral Analysis

Spectra of timeseries were computed with the NCL function specx_anal(). The function computes the spectra according to the following procedure. In a first step the timeseries is tapered. Here, a 10% taper was applied. In a next step the variance of the series is calculated. Then a forward FFT is applied and the real (C_r) and imaginary (C_i) coefficients are squared in order to obtain the peridiogram which is given $periodogram = {}_r^2 + {}_i^2$. The periodogram has an associated bandwidth of $1/N$ ($=$ delta frequency (df)) but is not statistically significant. In order to obtain the spectrum the periodogram is smoothed with a running average. Here, an x-point running average is used. In the last step the spectrum is normalized with respect

to the variance of the input series so that the area under the curve (f) is equal to the variance ($S(f)$) calculated in step 2 so that

$$area\_under\_curve = \sum S(f) \cdot df \cdot x \qquad (2.11)$$

where $x = 1.0$ except at the beginning and end values where $x = 0.5$. The theoretical Markow "red-noise" spectrum and the 5% and 95% confidence intervals were calculated with the function specx_ci() which uses the lag-1 autocorrelation returned as an attribute by the function specx_anal().

2.4.5   Wavelet Analysis

In order to gain information about amplitudes of periodic signals in a timeseries and their temporal variations wavelet analysis was applied. This technique decomposes the series into both the time and frequency space simultaneously. For the analysis the wavelet software in NCL was used which is an interface to the wavelt software provided by C. Torrence and G. Compo available at the URL: *http://paos.colorado.edu/research/wavelets/*. Following steps are performed during the calculation of the wavelet: first, a mother wavelet is chosen; here Morlet was used. Then, the Fourier transform for the mother wavelet is found. In a next step the same is done for the timeseries. Then the minimum scale s_0 and the other required scales s are selected in order to allow an adequate sampling of all frequencies present in the timeseries. Here, the timestep is one month, i.e. $dt = 1$, hence the smallest resolvable wavelet is $s_0 = 2dt = 2$. The larger scales are chosen as power of two-multiples-of-two of the smallest period. A further important parameter is the the wavenumber w_0. It gives the number of oscillations within the wavelet. One prerequisite is that the average of the wavelet must be zero. If $w_0 = 6$ is chosen then the errors due to the round-off errors are smaller than the common computer rounding errors. The largest possible scale J is half of the timeseries. The wavelet is computed as follows: The wavelet transformation into the Fourier domain is given by

$$W_n(s) = \sum_{k=0}^{N-1} \hat{x}_k \hat{\psi} \cdot (s\omega_k) e^{i\omega_k n\delta t} \qquad (2.12)$$

where ˆ indicates the Fourier transform (FT). The FT of the timeseries is given by

$$\hat{x}_k = 1/N \sum_{n=0}^{N-1} x_n e^{-2\pi ikn/N}. \qquad (2.13)$$

In order to compute the wavelet transform the FT transform of the wavelet function should be known analytically. Also, the wavelets need to be normalized as

$$\hat{\psi}(s\omega_k) = (2\pi s/\delta t)^{1/2} \hat{\psi}_0(s\omega_k). \qquad (2.14)$$

So, for each scale the daughter wavelet of the this scale is computed, then it is normalized by dividing through the square-root of the total variance. Then it is multiplied with the FT of the timeseries and is subsequently inverse transformed back into real space using the first of the three equations. Subsequently, the wavelet can be plotted. In order to avoid signals in the wavelet transform getting wrapped around to the other end the timeseries were padded with zeros at the end. The same amount of zeros as the lenth of the timeseries were added.

Chapter 3

Model evaluation

In this chapter the ability of the global atmosphere ocean general circulation model CCSM3 to simulate present day climate shall be evaluated. The first section analyzes the mean state of important atmospheric, oceanic and sea ice parameters; the second section focuses on the ability of the model to represent the most important atmospheric and oceanic variability modes of the high-latitude Southern Hemisphere and their impact on climate in this area. For this, the CTRL1990 simulation is compared to reanalysis data from the ERA40 ECMWF project and sea surface temperature and sea ice coverage data from the Hadley Centre. Section one shall focus on the mid and high latitudes of the Southern Hemisphere but also briefly touch on the Northern Hemisphere in order to give a more 'global' overview of the model performance.

3.1 Mean state of the climate system in the Southern Hemisphere

3.1.1 Atmosphere

Temperature

A correct representation of temperature distributions plays an important role in governing heat fluxes, moisture balances, and, of course, pressure and thus, winds. Therefore, the present day control simulation is compared to temperature patterns from the ERA40 reanalysis for both the surface but also throughout the atmosphere.

Figure 3.2 (b) shows the difference in global temperatures at the 850 hPa level between the CTRL1990 simulation and the ERA40 reanalysis. It can be seen that CCSM3 can represent the expected temperature patterns well. Especially in the Southern Hemisphere mid latitudes the temperature offsets appear small. Notable are the cold biases over the southern tips of Southern America and South Africa, and the warm biases over the equatorial western Pacific and the northern Andes. The colder than expected temperatures on the margins of Antarctica are presumably a result of the too high sea-ice extent in this region. On the 200 hPa level (Figure 3.2 (c)) the model simulates a too strong temperature gradient towards the poles, hence, underestimating the temperature at both poles which results in a temperature difference of up to 10°C between CTRL1990 and ERA40. These temperature biases can also clearly be seen when comparing the zonal mean of temperature throughout the troposphere

and stratosphere. In the region 700 hPa to 30 hPa the CTRL1990 shows a strong cold bias for the mid and high latitudes of the Southern Hemisphere. The surface levels over Antarctica appear warmer than expected from the ERA40 reanalysis. Strong warm anomalies can also be seen in the mid-latitude stratosphere.

When contrasting the simulated and expected temperature variability (Figure 3.1 (e)) it can be seen that again over the oceans the model performs well and that the temperature variability lies very close to the expected range. Larger biases occur again in mountainous regions such as the northern Andes, central Australia or central Antarctica. Areas in which the model strongly overestimates the temperature variability are the western Antarctic Peninsula and the West Antarctic ice sheet. However, the offset of the standard deviations is generally small and does not exceed 1°C. Thus, it can be concluded that CCSM3 is able to simulate the expected temperature patterns well close to the Earth's surface, that, however, the biases become larger over mountain ranges and towards the stratosphere, especially over the poles and in the stratosphere over the tropics.

Pressure, geopotential height and winds

Geopotential height at the 500 hPa height level (Figure 3.3 (a)) over eastern Antarctica corresponds well to observations; over western Antarctica and the Ross Sea the model overestimates the geopotential height. Over the Southern Ocean the opposite trend can be seen; here, a negative bias appears for geopotential height in the model. The biases appear to be barotropic: consistently too low SLPs (Figure 3.1 (b)) are found over the Southern Ocean, and too high SLPs are found over the Ross sea and over the Antarctic continent; thus, indicating that these biases are present throughout the lower troposphere. Areas of stronger than expected SLP variance are observed over the Southern Ocean and over areas with strong westerly winds. These model errors are also reflected in the wind patterns (Figure 3.1 (c), (d), (g) and (h)). The model overestimates both the strength of westerly winds located at 35°S to 50°S and of the easterly winds around the margins of Antarctica. This pattern is persistent not only for the surface winds but extends throughout the troposphere up into the stratosphere. Also, the variability of the zonal winds is much higher than for the ERA40 data; around Antarctica the variability (measured as the standard deviation) is increased by up to 2 °C. The meridional wind component shows only small offsets in comparison to the zonal wind where the biases are up to two orders of magnitude larger. In the area of the strong zonal westerly mid latitude winds of the SH the meridional winds simulated are too low, whereas they appear too strong on the south-eastern margin of Antarctica and around the Antarctic Peninsula. The variability of the north-south component of the winds lies well within the expected range and shows only small biases on the south-western margins of Antarctica.

Precipitation

Figure 3.4 shows the average precipitation for both the ERA40 reanalysis and the CTRL1990 simulation and the difference between the two. Generally the model is able to represent the precipitation patterns in the Southern Hemisphere well, that, however, it simulates much too strong precipitation especially in the tropics and over the Southern Ocean sector which may be linked to the too strong winds in this area. The biases over Australia appear small except for the most northern section whereas over South Africa precipitation values are systematically overestimated. Over Patagonia a similar problem occurs whereas over Argentine and
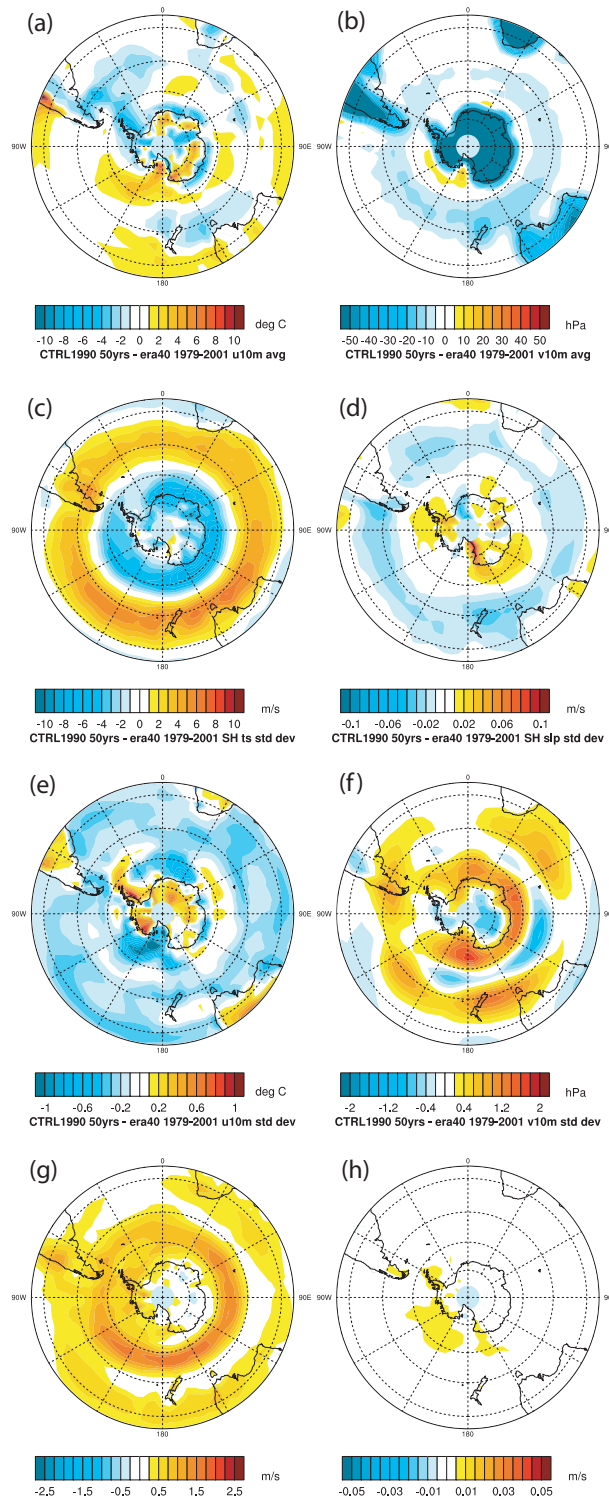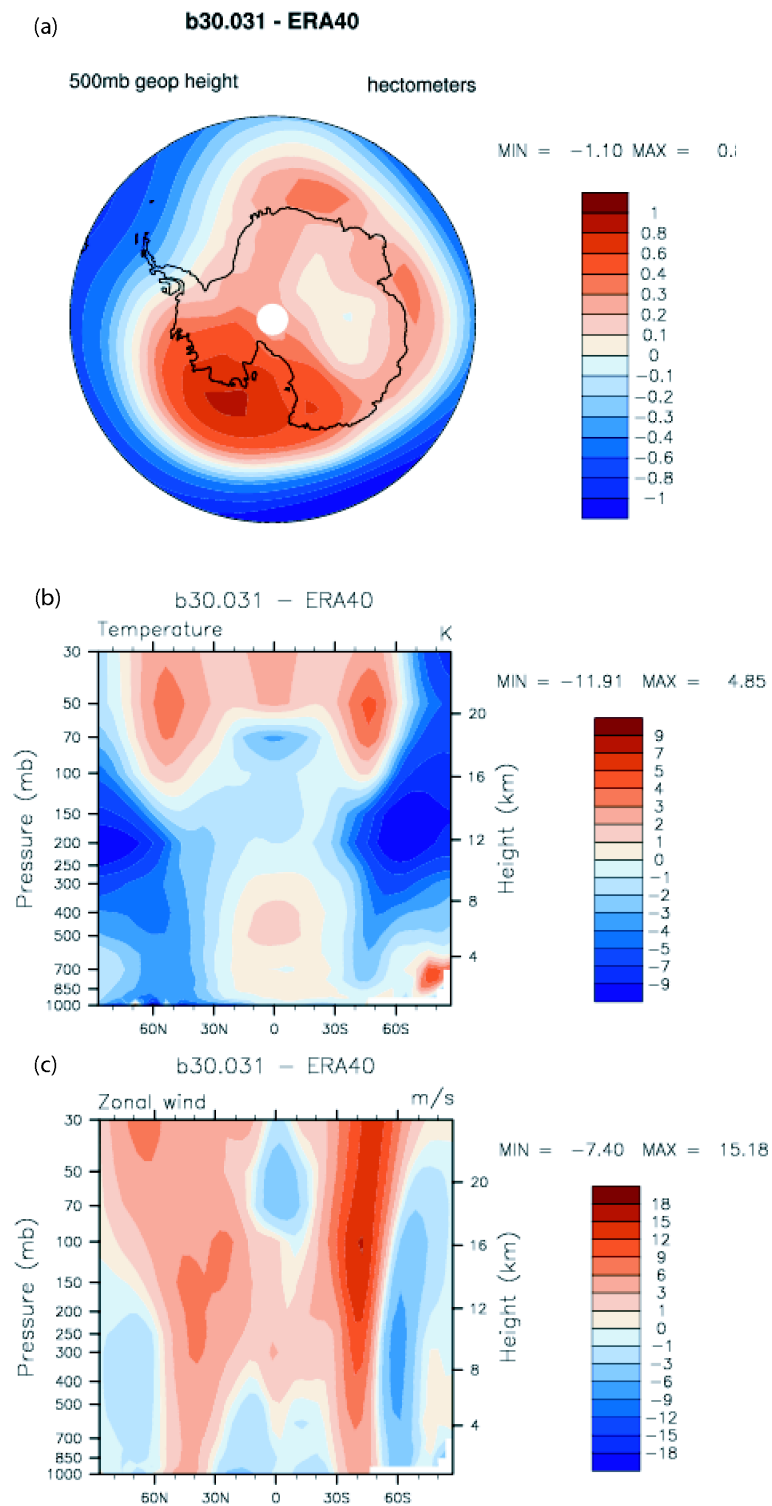
Figure 3.1: Difference between the CTRL1990 and the ERA40 mean (a) surface temperature, (b) surface pressure, (c) 10m zonal winds and (d) 10m meridional winds, and the standard deviation of (e) surface temperature, (f) surface pressure, (g) 10m zonal winds and (h) 10m meridional winds.
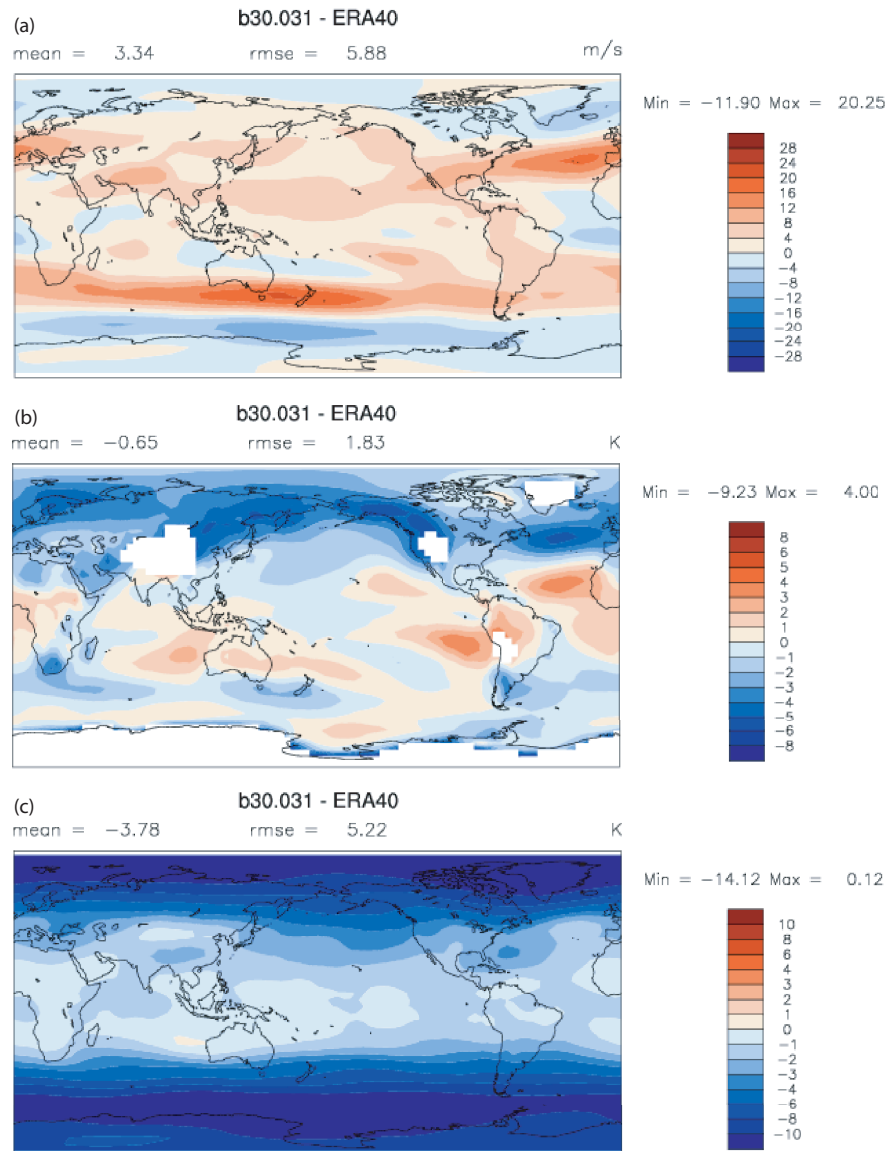
Figure 3.2: Difference between the CTRL1990 and the ERA40 mean (a) zonal winds at the 200hPa level (b) temperature at the 850hPa level, (c) temperature at the 200hPa level.

Figure 3.3: Difference between the CTRL1990 and the ERA40 mean (a) geopotential at 500hPa, (b) zonally averaged zonal winds, and (c) zonally averaged temperature.

central Chile the values appear much more accurate. Towards the north and hence increasing proximity to the tropics the biases become larger again. Thus, it can be concluded that the model is able to capture the general precipitation features well, but has severe problems in the magnitude of the precipitation.

3.1.2 Ocean

Antarctic Circumpolar Current

The ACC is one of the important features of the Southern Ocean as is prevents warm waters from the North reaching Antarctica and thus, of course impacts climate. Also, it may be influenced by changes in the climate system such alteration in the strength of the Southern Hemisphere westerlies or changes in temperature gradients. Here, the maximum barotropic stream function through the Drake Passage will serve as a measure of the strength of the current system. In the CTRL1990 simulation the ACC (Figure 3.5) has an average strength of 128.32 Sv and a standard deviation of 2.77 Sv giving a range from 125.55 Sv to 131.09 Sv in which 95% of the values lie.

Agulhas Current

In this study the strength of the Agulhas leakage is quantified as the strength of the barotrophic stream function in the area south of South Africa which is not influenced by the westerly flow of the ACC. For this the region 41.77°S to 39.05°S and 22.70°W to 33.50°W is selected and the barotrophic stream function is quantified. The calculations are performed for each of the summer and winter means in order to account for seasonal differences in the strength of the Agulhas leakage. The DJF mean in the CTRL1990 simulation yields a value of -50.39 Sv with a standard deviation of 1.96 Sv. Sv; for JJA a mean of -48.20 Sv is obtained with a corresponding standard deviation of 2.82 Sv. This gives a range from -46.47 to -54.31 Sv for DJF and one of -42.56 to -53.84 Sv for JJA in which 95% of the values, respectively, lie.
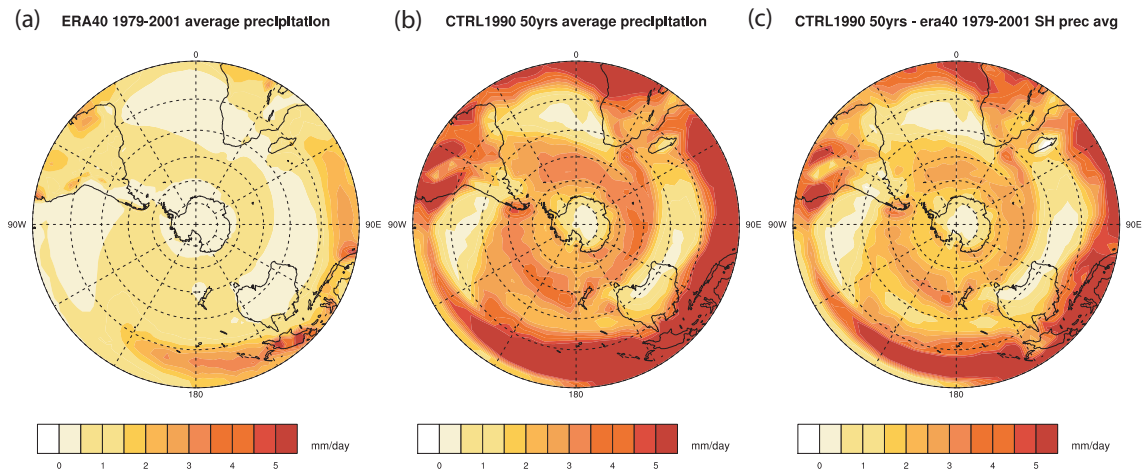
Figure 3.4: Average daily precipitation for (a) the ERA40 reanalysis, and (b) for the CTRL1990 simulation; (c) shows the difference between the two.
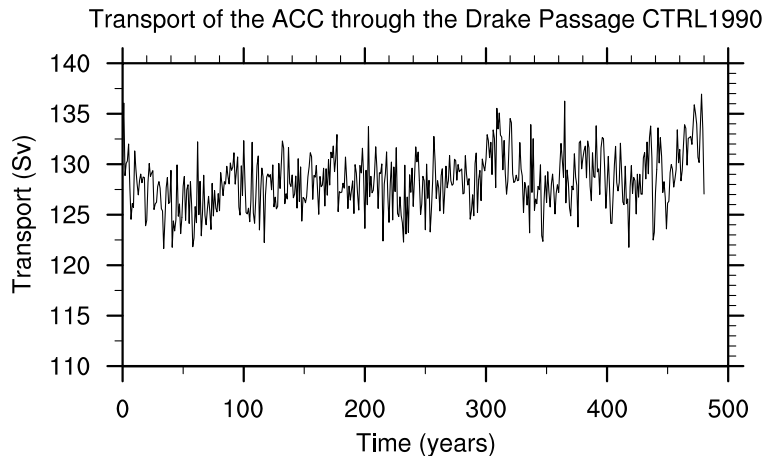
Figure 3.5: Transport through the Drake Passage [Sv] calculated for the CTRL1990 simulation.

3.1.3 Sea Ice

Sea ice is another important parameter for representing the variability within the climate system correctly. It influences albedo and hence the uptake or release of heat in the polar latitudes. Furthermore it impacts on the salt distribution in the proximity of Antarctica and can thus influence, e.g., deep water formation and the pathways and strength of ocean currents. CCSM3 gives an average sea ice area of 13.13 million km^2 with a standard deviation of 5.51 million km^2 for the CTRL1990 simulation. In comparison the HadISST dataset gives an average sea ice coverage of 9.82 million km^2 with a standard deviation of 0.21 million km^2. CCSM3 thus overestimates both the amount of sea ice and the associated variability. The average difference between the period of peak ice extent (September) and lowest ice extent (March) for the observations lies by 4.04 million km^2 whereas the CTRL1990 simulation gives a value of 14.22 million km^2. Again, the model shows an overestimation of the variability by a factor of about 3.5.

Applying an EOF analysis (Figure 3.8) on sea ice concentration (SIC) shows that the observed leading mode of variability has a dipole structure with the centers located over the Weddell and Ross Sea. The positive regression coefficients over the Ross Sea extend up to 35°E. In the model a dipole pattern also shows up, however, here the negative pole is shifted approximately 30° west. Also the second positive center of action which in the observations is strongly connected to the Ross Sea center is separated in the model. The variability explained by the first EOF for the observations lies by 22.1% whereas in the model the explained variance lies by only 12.5% thus suggesting that the main sea ice variability patterns are present if yet with a slightly shifted pattern and are not as dominant as in the observations. This is also evident when comparing the timeseries of the observational and model data. The timeseries of the sea ice variability for the HadISST dataset can be seen in Figure 3.7, the corresponding one for the model in Figure 3.6. If the timeseries of each the center of action over the Weddell and Ross Sea are contrasted then a clear anticorrelation of $r = -0.684$ which is highly significant is visible for the HadISST data. This, however, is not the case for the CTRL1990 simulation. Here, the timeseries correlate with $r = 0.956$ which again is highly significant. Also, the variability of Ross and Weddell Sea (180°W to 0°W) shows a very different and

independent behaviour from the remaining sea ice (0°W to 180°W). The hemispheric sea ice variations mainly reflect the variability in the extra-dipole area. In the model this clear separation however does not show up. Here, the Southern Hemisphere sea ice exhibits a much stronger coherency between the regions and the regional sea ice variability closely reflects the hemispheric variability. Thus, it can be concluded that the model is able to represent the total sea ice variability well, but shows deficits in simulating the interannual regional variability. It can be seen that the main variability pattern of Antarctic sea ice (Figure 3.8) takes place as a dipole pattern which CCSM3 is able to depict, however, it explains less variability than the observations and it is shifted in comparison to the observations. Thus regional changes in sea ice in the transient simulations need to be treated with care as the model has problems representing these.

3.2 Variability modes in the Southern Hemisphere

3.2.1 Southern Annular Mode

The Southern Annular Mode (SAM) is known as the leading mode of atmospheric variability in the Southern Hemisphere mid to high latitudes. SAM describes extra-seasonal variability in the extra-tropical flow on sub-monthly to inter-annual time scales. These variations express shifts of atmospheric mass between the middle and high latitudes which can clearly be seen in the surface pressure and geopotential height fields. It shows an approximately zonal structure in both the surface pressure and geopotential height field at 850 hPa and is characterised by a change in sign at approximately 45°S and 60°S [*Thompson et al.*, 2000; *Marshall*, 2003].

In this study, SAM is calculated as the leading empirical orthogonal function (EOF) in the geopotential height field at 850 hPa (Z850hPa) south of 20°S after removing the seasonal cycle and applying area weighting according to *Thompson et al.* [2000]. The time series of the principle component is obtained by projecting the spatial EOF-pattern onto the anomalies in geopotential height at 850 hPa. A further possibility to calculate the SAM index is given by *Gong and Wang* [1999]. They calculate SAM as the normalised difference between the zonally averaged SLP at 40°S and 65°S.

As the comparison between the two methods yields a highly significant correlation the analysis is restricted to the EOF method.

SAM Pattern

Figures 3.9(a) and 3.10(a) show the leading principle components of extra-tropical geopotential height at the 850 hPa level calculated for the ERA40 reanalysis and the CTRL1990 simulation, respectively, regressed onto SLP. On a year-round monthly basis SAM appears as the leading mode for both the reanalysis and the simulation. The model is able to represent the SAM pattern found in the ERA40 data well. In both cases, the change in sign is located at approximately 55°S and is shifted slightly northwards over the Amundsen-Bellingshausen Sea. The CTRL1990 pattern shows a more zonal structure than expected from the ERA40 reanalysis where three distinct centres of action are visible. They are located in the central southern Pacific, the central southern Atlantic and the central southern Indian Ocean at 45°S. In the CTRL1990 simulation the SAM imprint on SLP is stronger than in ERA40, especially in the region 120°W-80°W in the latitude band 45°S-30°S. The correlation between the two
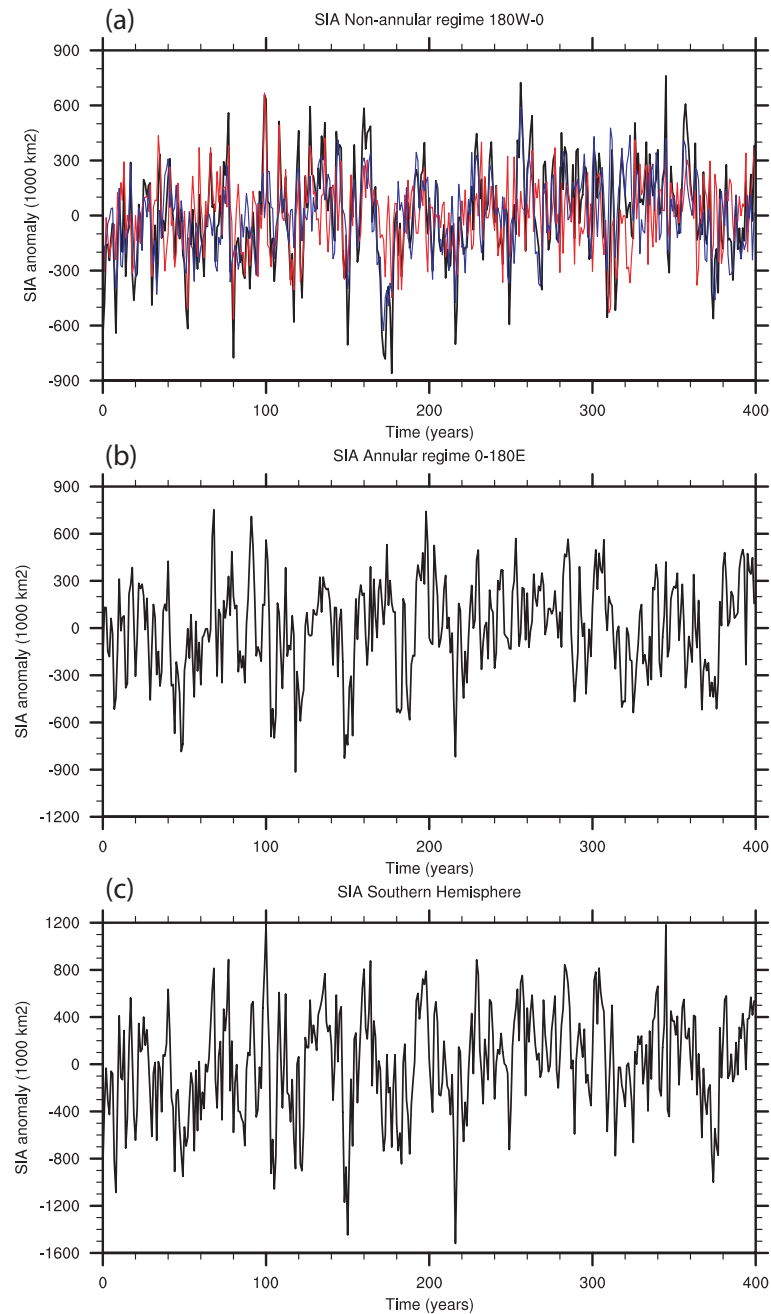
Figure 3.6: Yearly sea ice area anomalies (1000 km^2) in the CTRL1990 simulation calculated for (a) the dipole region (0:180°W) where red stands for the Bellingshausen-Weddel Sea, blue for the Amundsen-Ross Sea sector and black for the whole dipole region, (b) the extra-dipole region (0:180°E) and (c) the Southern Hemisphere mean.
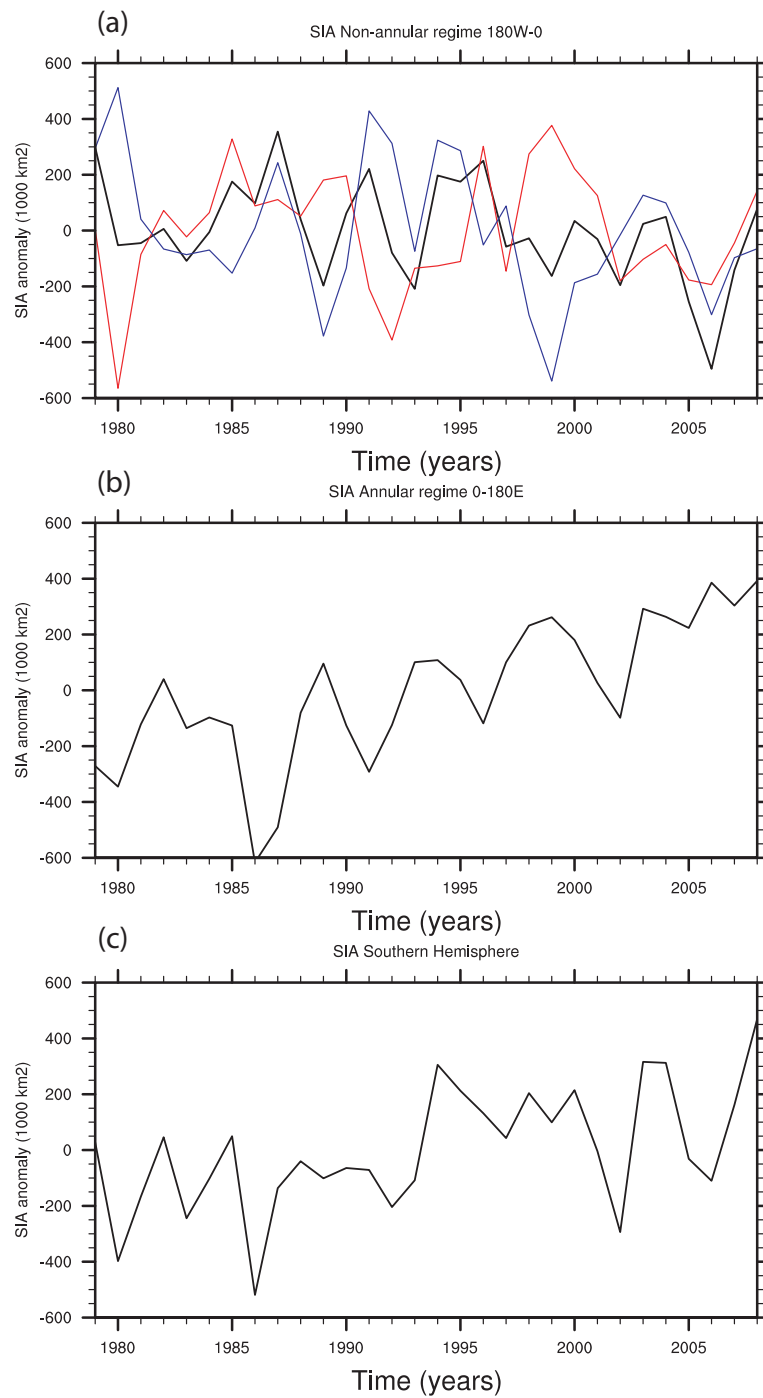
Figure 3.7: Yearly sea ice area anomalies (1000 km^2) for HadISST data from 1979-2008 calculated for (a) the dipole region (0:180°W) where red stands for the Bellingshausen-Weddel Sea, blue for the Amundsen-Ross Sea sector and black for the whole dipole region, (b) the extra-dipole region (0:180°E) and (c) the Southern Hemisphere mean.

CCSM3 CTRL1990 1st EOF of yearly SIC **1979-2008 1st EOF of yearly SIC**
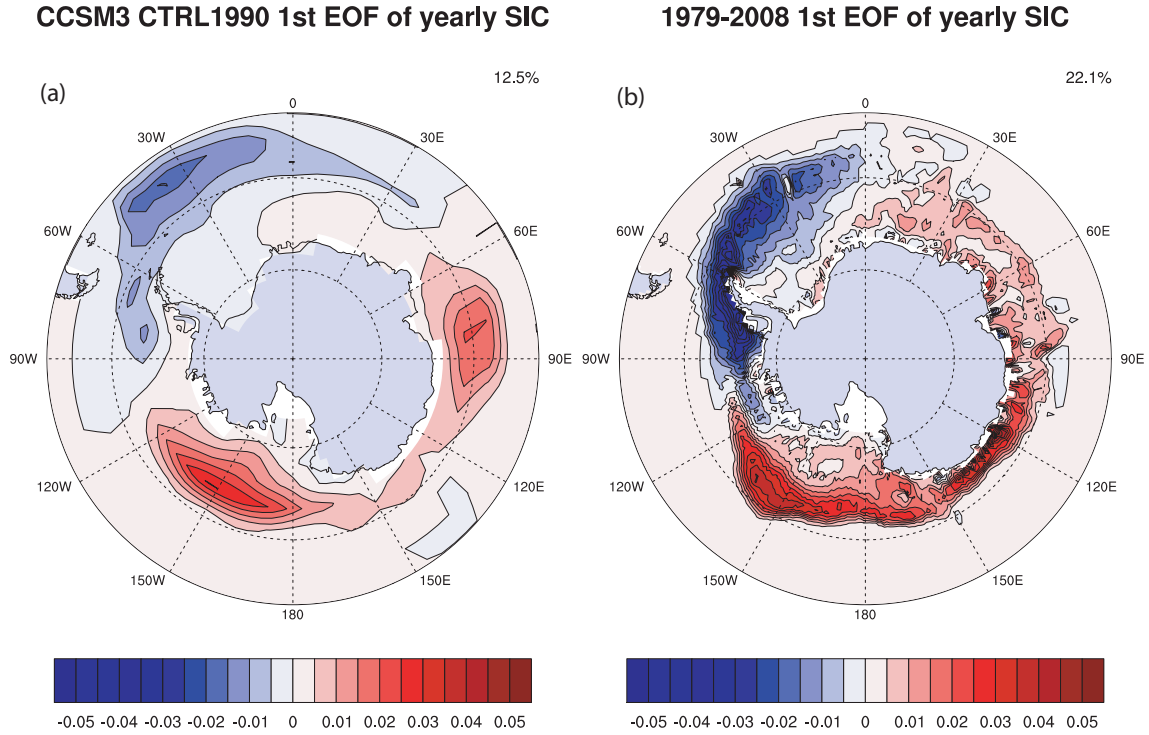

Figure 3.8: 1st EOF of Southern Hemisphere yearly sea ice concentration anomalies for (a) the CTRL1990 and (b) HadISST data from 1979-2008 shown as a regression of the timeseries of the 1st EOF onto SIC anomalies. The data was area-weighted prior to calculation of the EOFs and the annual cycle was removed.

patterns yields a value of $r = 0.89$ which is significant at the 1% level (df=1822). SAM explains 17.23% of the variance in the Z850hPa field in the ERA40 data and 27.54% in the CTRL1990 run; thus, the explained variance by SAM is overestimated by approximately 10% in CCSM3.

On a seasonal scale larger differences appear between the model and the observations. During the austral summer (DJF) SAM shows the largest impact on atmospheric variability: for ERA40 this corresponds to 31.60% explained variance and for CTRL1990 to 49.65% - again, the model overestimates the zonal variations. This pattern is consistent for the other three seasons. It correctly shows a decrease in the influence of SAM in these seasons, however, as previously seen the explained variance is increased by approximately 10% (Table 3.1). A

Table 3.1: Variance (%) of Z850hPa explained by SAM calculated as EOF1 Z850hPa in the region 20 °S - 90 °S applying area weighting for (a) 'all months' after seasonal cycle was removed, (b) December to February (DJF), (c) March to May (MAM), (d) June to August (JJA), and (e) September to November (SON) for both the ERA40 reanalysis and CTRL1990 simulation.

Data	All months	DJF	MAM	JJA	SON
ERA 40	17.23	31.60	21.95	19.53	19.51
CTRL 1990	27.54	49.65	30.15	29.34	32.62
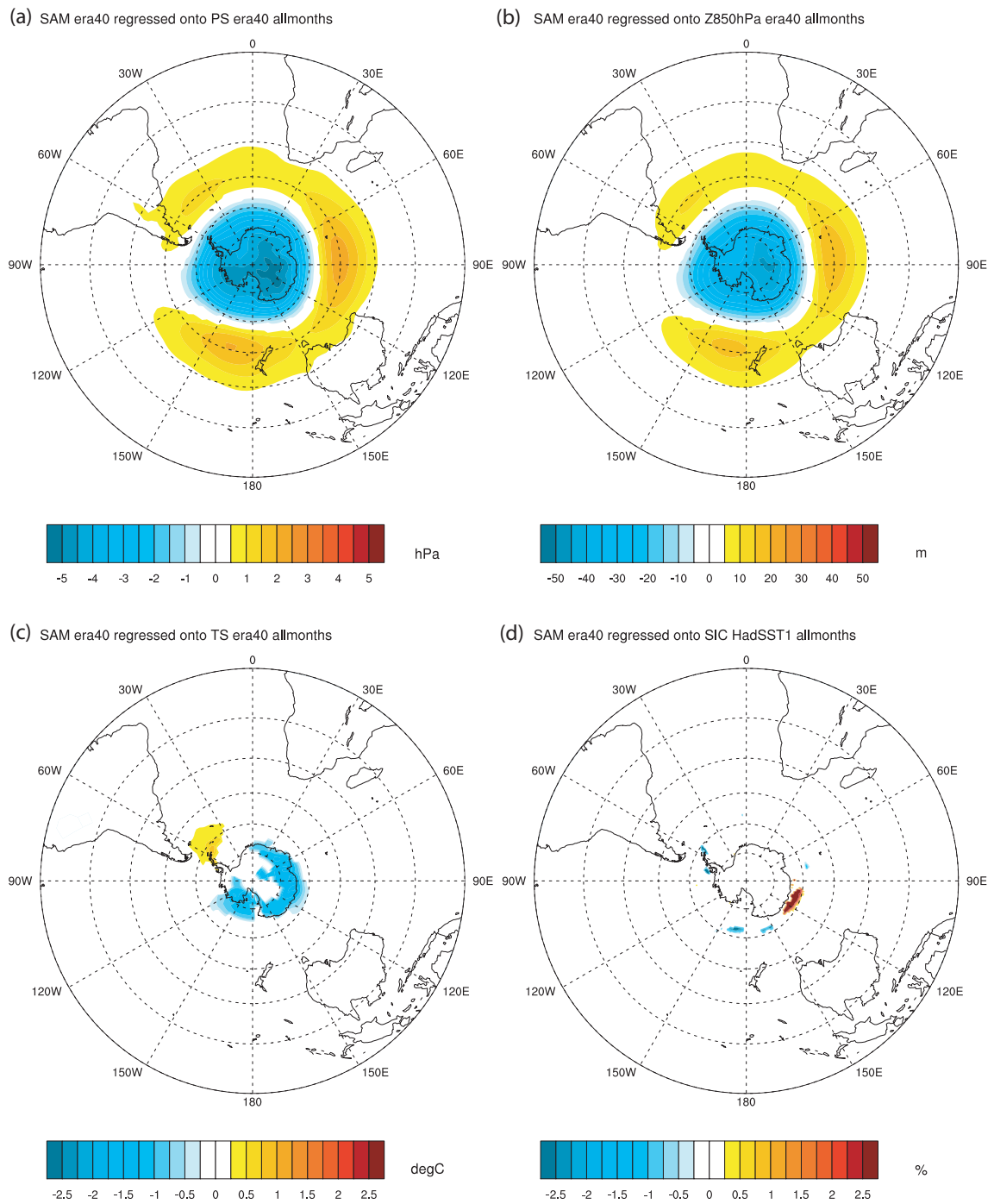
Figure 3.9: SAM timeseries calculated from EOF1 Z850hPa ERA40 regressed onto (a) sea level pressure, (b) Z850hPa, (c) surface temperature and (d) sea ice concentration. Only significant (at the 5% level) regression coefficients are shaded.
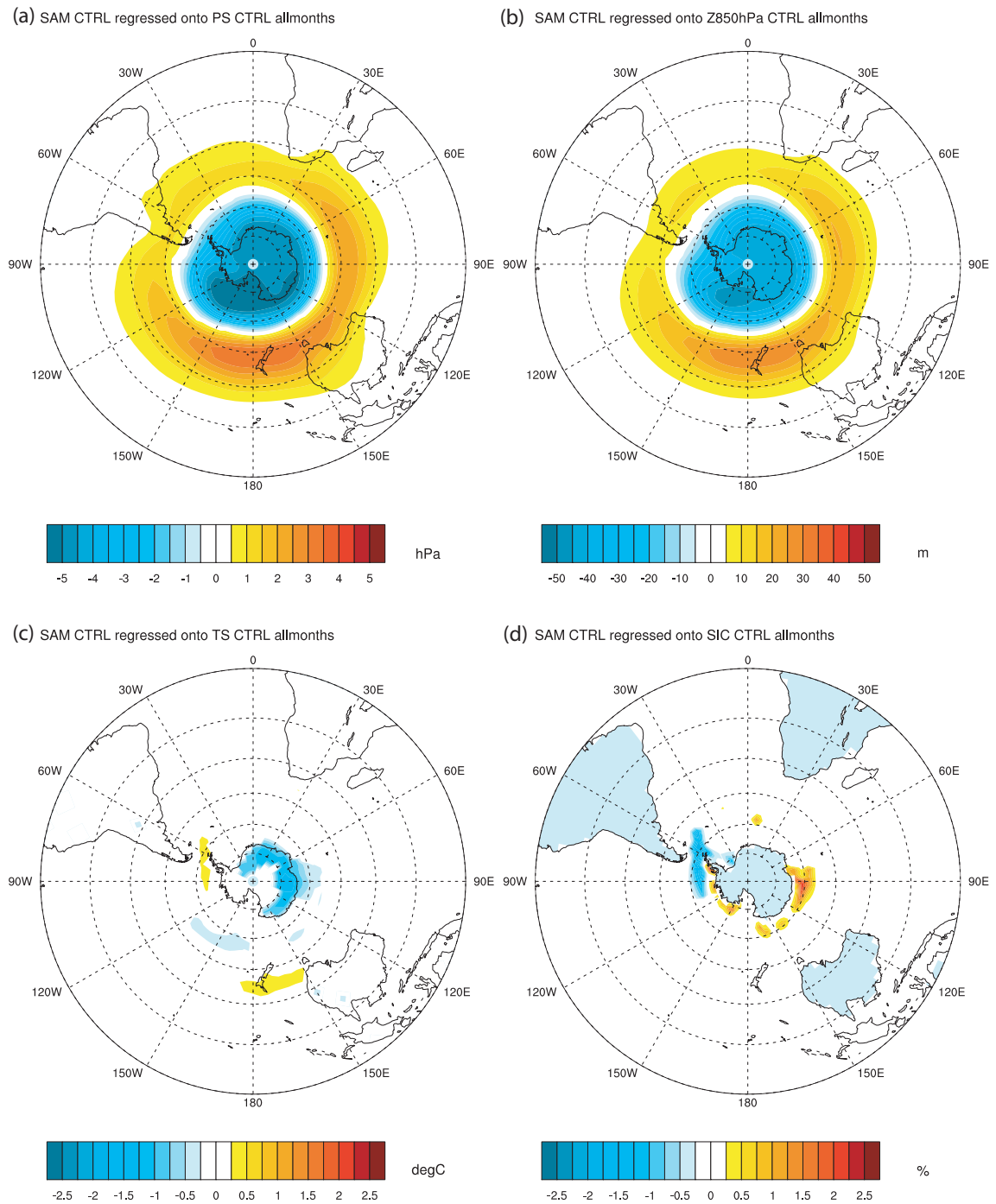
Figure 3.10: SAM timeseries calculated from EOF1 Z850hPa CTRL1990 regressed onto (a) sea level pressure, (b) Z850hPa, (c) surface temperature and (d) sea ice concentration anomalies. Only significant (at the 5% level) regression coefficients are shaded.
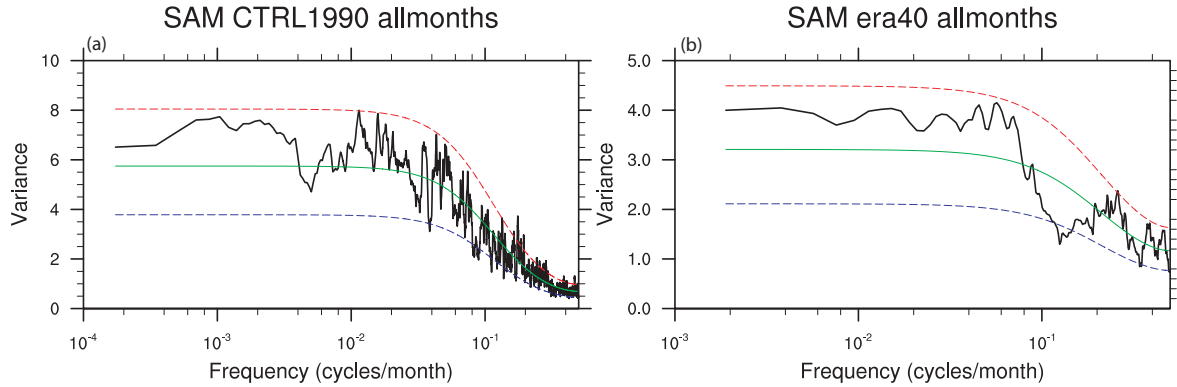
Figure 3.11: Spectra of the monthly SAM Index calculated for (a) the CTRL1990 simulation and for (b) ERA40 reanalysis data. The green line indicates the theoretical Markow red noise spectrum, dashed lines show its confidence bounds at the 5% and 95% levels, red indicates the upper boundary, blue indicates the lower boundary. Note the different scales of the two figures.

comparison between the SAM patterns between the respective seasons yields a good correspondence for DJF and JJA between model and observations, respectively. For austral spring (SON) and autumn (MAM), respectively, however, the first EOFs show the largest differences. For SON the patterns show large differences in the Western half of the Southern Ocean region: The model still simulates SAM as the dominant pattern of variability whereas in the ERA40 data consists of a pattern with two positive and two negative poles. During austral autumn (MAM) the patterns also differ strongly. ERA40 shows three distinct centres of action in the 45°S latitude band, whereas CTRL1990 only has a single circumpolar centre of action, but shows a distinct pole of opposite sign over the Amundsen-Bellingshausen Sea. Thus, hereafter SAM shall only be considered in approaches using 'all months' and the seasons DJF and JJA, respectively.

Temporal behaviour of SAM

Spectra (Figure 3.11 calculated for the month-to-month variations of the SAM index exhibit significant peaks at periods 5 months for ERA40 and at 2-6 months for CTRL1990 at the 95% confidence level, respectively, thus showing approximately the same frequency bands in which the variability takes place. On longer (interannual to decadal) timescales SAM calculated from both the observational data and the CTRL1990 simulation show a white spectrum which indicates that the model again is able to capture this variability mode accurately on a temporal scale. As mentioned earlier the model overestimates the variability explained by the SAM - at lower frequencies the variance calculated for SAM from the CTRL1990 lies around a value of 6 whereas it is only half as large for the ERA40 data.

Impacts of SAM

In Figures 3.9(c),(d) and 3.10(c),(d) the impacts of SAM on surface temperature (TS) and sea ice concentration (SIC) are shown. Years of SAM with positive sign are associated with temperatures which are decreased by 0.5 - 1.5 °C over the margins of the Antarctic continent. One exception can be seen over the northern Antarctic Peninsula and the adjacent Southern

Atlantic where a warming of 0.4 to 1.2 °C occurs. A very similar pattern is found in CTRL1990 suggesting that CCSM3 can represent the dynamics associated with SAM for the linkage between temperature and pressure well. During the summer months the temperature response closely resembles the one found for 'all months' (not shown). Again over the eastern half of Antarctica a temperature decrease of approximately 1 °C is observed; however, during this season no warming over the Antarctic can be seen. The pattern found in CTRL1990 confirms this finding but shows a too strong impact on temperature over the Southern Ocean and in the latitude band 30S-45S. During austral winter the response corresponds to the one found for 'all months' for ERA40 as well as for CTRL1990, both in pattern and magnitude (not shown). SAM appears to have only a weak influence on SIC when monthly anomalies in SIC are considered. No clear impact is visible from the comparison of the SAM calculated from ERA40 data with HadSST1 SIC data using either regression or correlation analysis. CCSM3 suggests an increase in sea ice concentration by 2% around Antarctica and a decrease of up to 2.5% in the Amundsen-Bellingshausen Sea during a SAM positive phase. A similar picture emerges for the summer and winter season, respectively. Again the model points towards a weak influence of SAM on SIC; on seasonal time scales the ERA40 analysis confirms these findings, and correlation coefficients between the variables only range up to 0.3, hence suggesting a weak impact of SAM on SIC.

Therefore, it can be concluded that the model can simulate SAM well, both on a spatial and temporal scale. The patterns of pressure variability correspond well on a year round monthly basis and for austral summer and winter, and the impacts of the variations lie within the expected range. For the spring and autumn the patterns are less clear and show greater discrepancies. Thus, changes in SAM shall be analyzed for month-to-month changes, and variations occurring during the DJF and JJA seasons in the transient simulations.

3.2.2 Semiannual Oscillation

A further important mode of variability in the mid to high latitudes of the Southern Hemisphere is the Semiannual Oscillation (SAO), which is a coupled-ocean atmosphere phenomena affecting climate on seasonal time scales. It is characterized by the expansion and weakening of the circumpolar trough during the austral spring and autumn, and a contraction and strengthening of the trough during the austral summer and winter. The circumpolar trough is a region of low pressure located in the region 60°S - 65°S in which the easterly winds show a high degree of variability. This area is marked by strong storms transporting warm moist air from the mid to the high latitudes resulting in extensive cloud formation and precipitation.

van Loon [1967] developed an index for the SAO from satellite observations based on the zonal mean temperature differences between 50°S and 65°S at 500 hPa. A further measure for the SAO is the difference in zonally averaged SLP at 50°S and 65°S introduced by [*Meehl et al.*, 1998].

Figure 3.12 (b) shows the annual cycle of zonal temperature differences between 50°S and 65°S on the 500 hPa level. For the ERA40 data the semiannual nature of the temperature differences is clearly visible with distinct peaks in July and January corresponding to the contraction of the circumpolar trough during these months when the meridional temperature gradient increases by up to 1.5°C. For the CTRL1990 simulation no clear semiannual structure appears and the temperature differences between 50°S and 65°S are reduced by approximately

1 - 2 °C. The SLP gradients between 50°S and 65°S can be seen in Figure 3.12 (a). Again, the ERA40 data shows a clear semiannual cycle with peaks in March and September with an amplitude of up to 3 °C. The September peak is less pronounced than the austral autumn maximum. Again as seen for T500 hPa the model does not simulate the semiannual cycle observed in the reanalysis data as clearly. CTRL1990 shows a much more strongly pronounced annual cycle with local maxima overlaid in April and November, suggesting that a weak semiannual cycle may be present in CCSM3. However, it appears to be masked by a much more dominant annular cycle in SLP which is increased by up to 7 hPa in the model.

Thus, due to the strong errors of the model in simulating the SAO seen for both SLP and T500 hPa, this variability mode shall not be considered when analysing the simulations with time varying forcing.

3.2.3   South Pacific Dipole

The South Pacific Dipole (SPD), also known as the Antarctic Dipole, is a further mode of interannual atmospheric variability in the Southern Hemisphere showing an important influence on SIC in the Antarctic [*Yuan and Martinson*, 2001]. It is characterized by a SLP dipole with centers located in the South Pacific and South Atlantic and has been denoted as part of the Pacific-South America teleconnection pattern, as it is part of a wave train propagating from the Pacific around the southernmost point of South America into the South Atlantic [*Mo and Higgins*, 1998]. A link between this variability mode and ENSO has been established by several authors [*Renwick*, 2002; *Drost et al.*, 2007; *Kiladis and Mo*, 1998; *Mo and Higgins*, 1998].
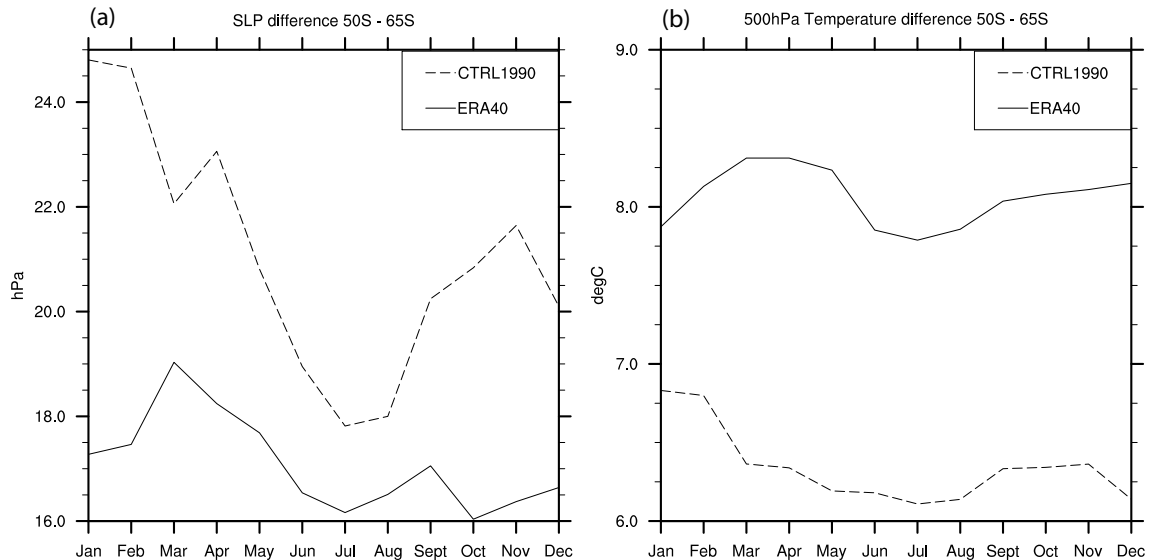
Figure 3.12: Annual cycle of (a) SLP and (b) T500 hPa difference between 50°S and 65°S for ERA40 and CTRL1990, respectively.
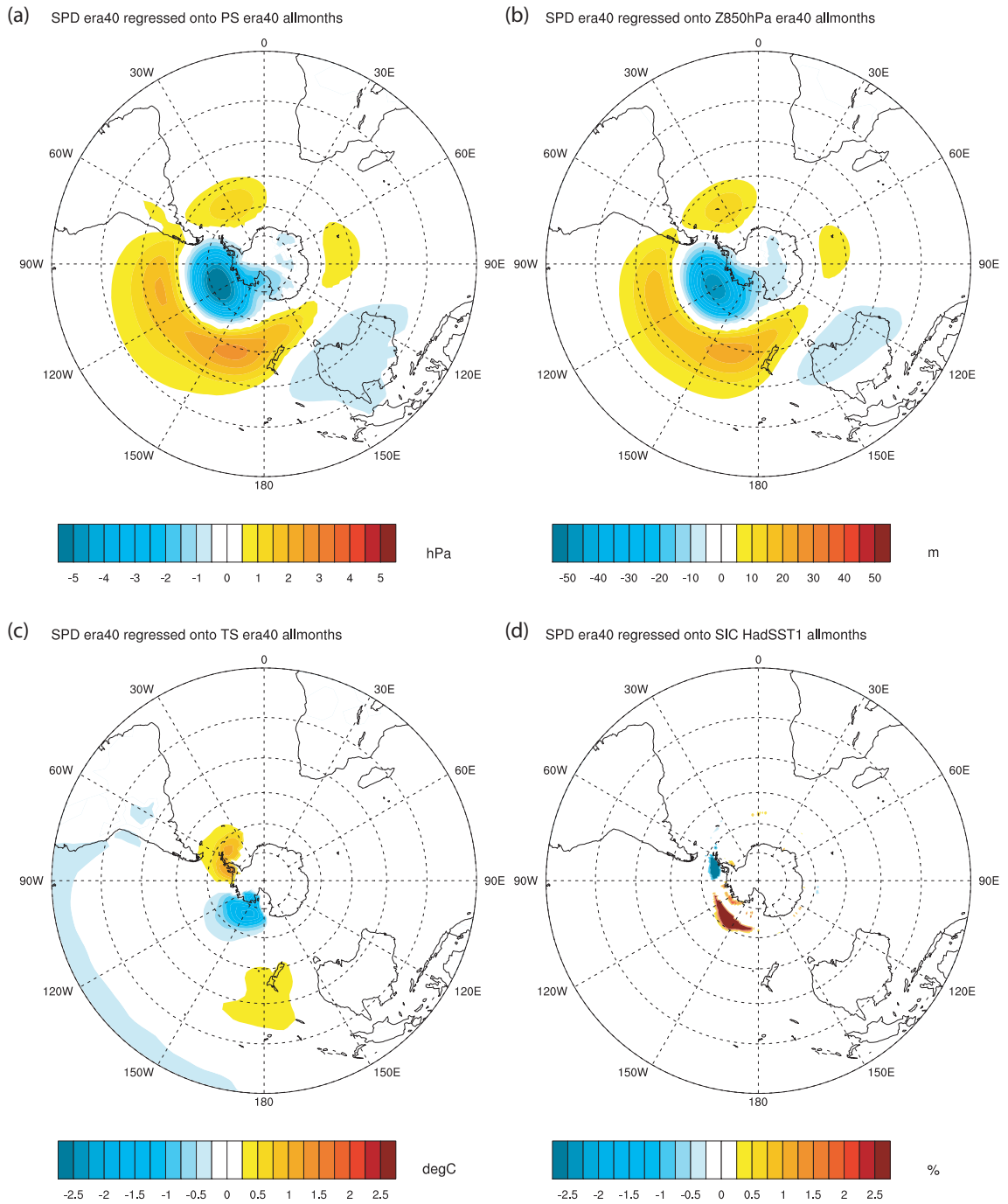
Figure 3.13: SPD timeseries calculated from EOF2 Z850hPa ERA40 regressed onto (a) sea level pressure, (b) Z850hPa, (c) sea ice concentration and (d) surface temperature. Only significant regression coefficients are shaded.
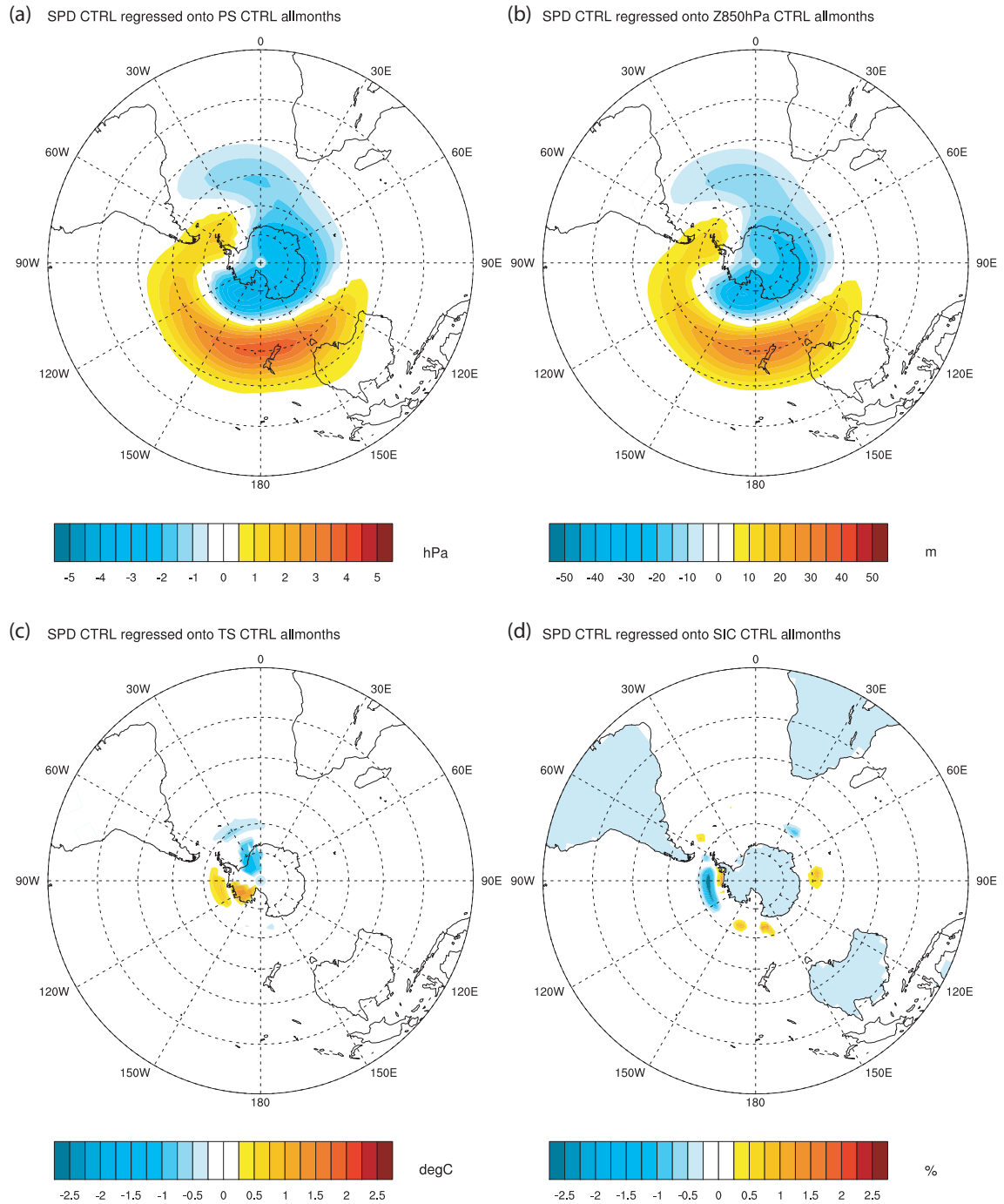
Figure 3.14: SPD timeseries calculated from EOF2 Z850hPa ERA40 regressed onto (a) sea level pressure, (b) Z850hPa, (c) sea ice concentration and (d) surface temperature. Only significant regression coefficients are shaded.
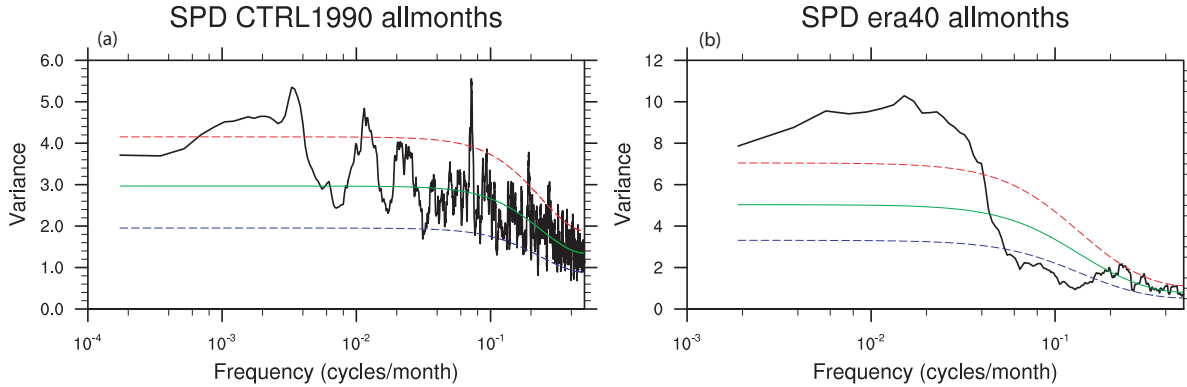
Figure 3.15: Spectra of the monthly SPD Index calculated for (a) the CTRL1990 simulation and for (b) ERA40 reanalysis data. The green line indicates the theoretical Markow red noise spectrum, dashed lines show its confidence bounds at the 5% and 95% levels, red indicates the upper boundary, blue indicates the lower boundary. Note the different scales used for the two plots.

Temporal behaviour of SPD

The spectrum calculated for the SPD timeseries from the ERA40 reanalysis data set (Figure 3.15) shows a band of significant variability between 2 years and 20 years peaking at approximately 8 years. The spectrum for the CTRL1990 simulation similarly shows a peak at 8 and 20 years; however, in this case the two peaks do not merge as for the ERA40 data but are clearly separated. Also, a peak at approximately 12 months emerges which is presumably a remainder of the seasonal cycle.

Impacts of SPD

In the ERA40 data the SPD can be seen in EOF2 of extra-tropical Z850hPa (Figure 3.13). The wave train appears clearly with centers of action located approximately 20 east of New Zealand, over the Bellingshausen-Amundsen Sea and to the east of the southernmost tip of South America for both SLP and Z850hPa. The SPD pattern leads to a dipole response in both surface temperatures and sea ice concentration over Ross and Weddell Sea, respectively. In the CTRL1990 run a similar pattern is present, however not as clearly expressed. Again the centers of action lie to the east of New Zealand and over the Bellingshausen-Amundsen Sea / Ross Sea, however, the third pole is not located at the position as expected from the simulations. It is connected to the first centre and is shifted to the south-east with respect to the ERA40 pattern. Also, whereas in the ERA40 reanalysis the SPD pattern is limited to the sea adjacent to the western half of Antarctica, its influence extends across the island in the CTRL1990 simulation. A pattern correlation yields a highly significant value of $r = 0.36$. These differences in the pattern also influence the temperature and SIC responses: for surface temperature again a dipole can be seen, however, it is shifted into the Bellingshausen-Amundsen Sea and into the eastern half of the Weddell Sea and is reversed in sign in comparison with the ERA40 data. The sea ice response shows similarities with the observations, the negative pole over the Bellingshausen-Amundsen Sea can be found in both the observations and the model. The clear positive pole over the Ross Sea, however, is not present in the model. Thus, it can be concluded that the model is able to capture part of the

variability of the SPD, that, however, errors exist in both the pattern representation and the responses of temperature and SIC to changes in the atmospheric variability pattern.

3.2.4   Zonal Wave 3

The Zonal Wave 3 (ZW3) is yet another mode of variability of the large-scale atmospheric flow in the extra-tropical SH describing the meridional flow. This structure plays an important role from daily to interannual time scales and is associated with a quasi-stationary wave pattern. The ridges are commonly located downstream of the Southern Hemisphere continents, i.e. to the East of the southernmost tips of Africa, Australia and South America. ZW3 is important for the meridional transport of heat in the atmosphere, and thus, may have an influence of sea-ice concentrations around Antarctica [*Raphael and Holland*, 2006]. One method for the calculation of ZW3, which takes into account the location of the three ridges is given by *Raphael* [2004]. I_{zw3} is calculated as
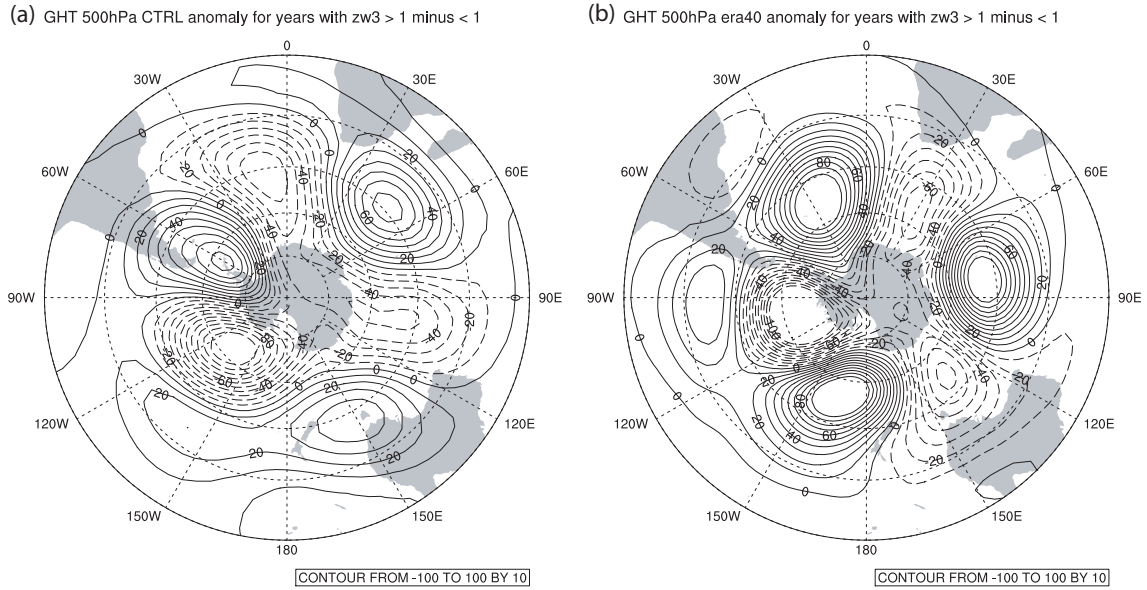
$$I_{zw3} = \sum_{i=1}^{3} I_i, where \tag{3.1}$$

$$I_i = (X_{monthly} - \bar{X}_{monthly})/\sigma_{monthly} \tag{3.2}$$

where $X_{monthly}$ is the three monthly anomaly of geopotential height at 500 hPa (Z500hPa), $\bar{X}_{monthly}$ is the three-monthly climatological mean and $\sigma_{monthly}$ is the three-monthly standard deviation of Z500hPa at the location i. The locations i were determined from *van Loon and Jenne* [1972] who calculated the annual average location of the ridges of Z500hPa. Here the ridge areas i are given as (a) 45°S - 50°S and 45°E -60 °E, (b) 45°S - 50°S and 161°E - 171°E, and (c) and 71°W - 81°W.

A further method of calculation is given by *Yuan and Li* [2008]. They calculate the ZW3 pattern as the 1st EOF of the meridional wind field at 500 hPa (V500hPa). The index is obtained by projecting the 500 hPa meriodional wind anomalies onto the EOF pattern. In this study the latter method shall be used.

Figure 3.16 shows the ZW3 pattern as differences in the Z500hPa field between the positive and the negative phase of the ZW3. In (a) the ZW3 index was calculated from the 1st principle component of V500hPa in the area 30°S to 90°S and shows the pattern in the CTRL1990 simulation; (b) shows the pattern for the ERA40 reanalysis. A comparison with Fig. 8d in *Raphael and Holland* [2006] shows that both methods yield very similar results for present day simulations with CCSM3. A comparison between Figure 3.16 (a) and (b) also shows that the model is able to capture the wave number 3 pattern well. However, both the ridges and troughs are shifted approximately 30° east against the positions expected from the analysis of the observational data, thus reducing the pattern correlation to a value of $r = 0.17$ which is still significant at the 1% level. Slight differences can be seen for both the ridge and trough south of Australia. The ridge is shifted and shows a boarder crest whereas the trough has an elongated base and is connected to the trough over the South Atlantic. Also the model overestimates the variability in the Z500hPa field caused by the ZW3 systematically by up to a factor of two. Nevertheless, it can be concluded that model is able to capture the main feature of the ZW3 pattern very well, and that this variability pattern can be analyzed in the transient simulations.

(a) GHT 500hPa CTRL anomaly for years with zw3 > 1 minus < 1

(b) GHT 500hPa era40 anomaly for years with zw3 > 1 minus < 1
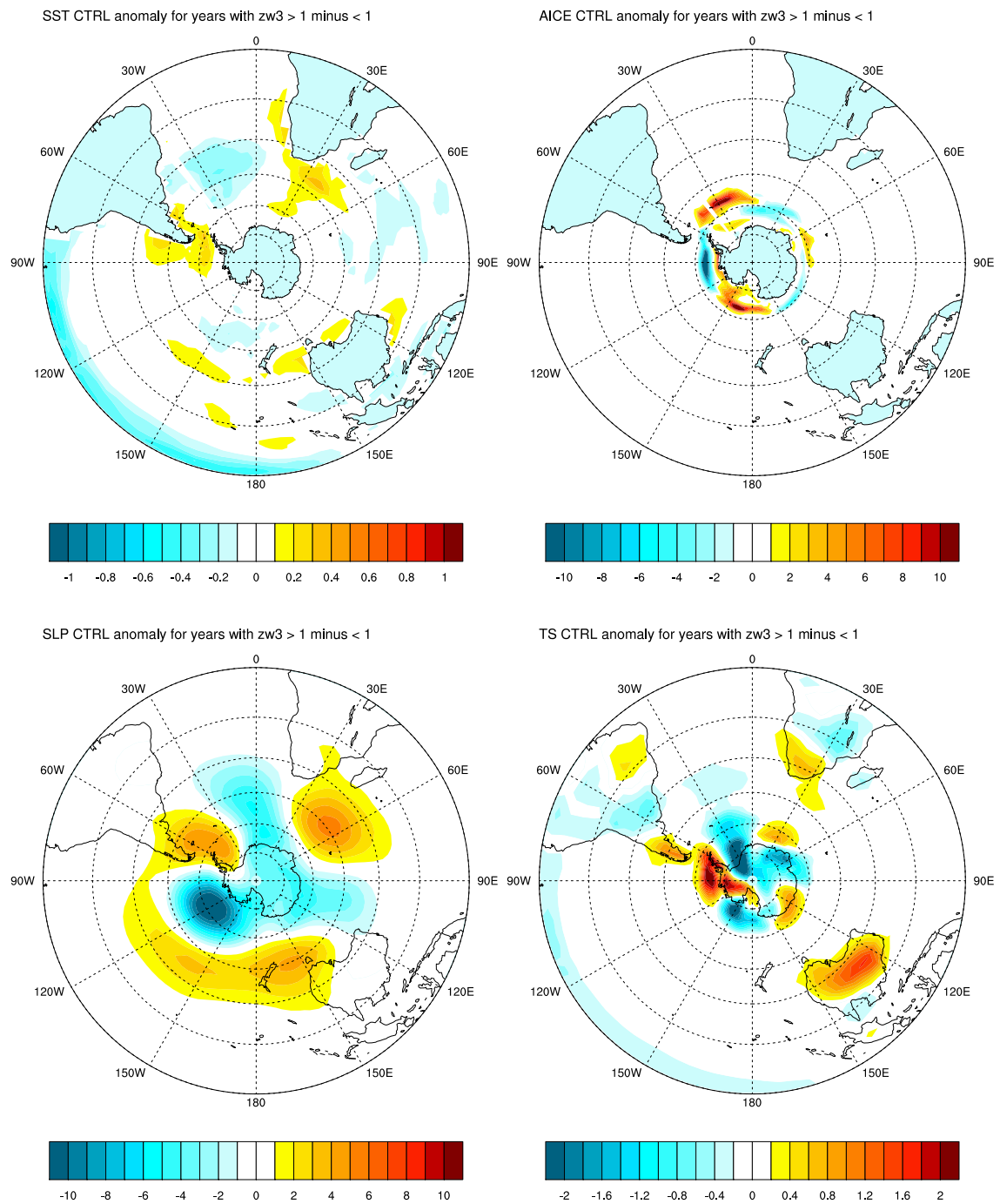
CONTOUR FROM -100 TO 100 BY 10

Figure 3.16: Composite of Z500hPa changes between positive and negative state of the ZW3 where the ZW3 was calculated according to the method proposed by *Yuan and Li* [2008]. (a) shows the composite for the ERA40 data, (b) shows the composite calculated for the CTRL1990 simulation.

Temporal behaviour of the ZW3

Both the frequency spectra calculated for ZW3 in the ERA40 data and the CTRL1990 simulation (Figure 3.18) indicate that the ZW3 is predominately a white noise process on timescales greater than one year. Neither the observational nor the model data indicate that this variability mode shows a frequency band on which interannual variability predominately takes place and is shifted into the red-noise area.

Impacts of the ZW3

The impacts of the zonal wave 3 can be seen in the high latitudes of the Southern Hemisphere in a variety of variables (Figure 3.17). The wave number 3 pattern is also present in the SLP field, however, again the ridge south of Australia appears elongated and extends far west into the Pacific and is even connected to the ridge located over the southernmost point of South America and the Antarctic Peninsula. The strongest changes in SLP occur at the trough positioned over the Amundsen-Bellingshausen Sea, i.e. in the Amundsen low pressure system. In the western half of the Southern Ocean (over the Ross, Amundsen-Bellingshausen and Weddell Sea) the SLP pattern closely resembles the SPD pattern discussed in the previous section. The SST pattern shows interesting similarities with the SLP field: in the locations of the ridges or in close proximity upstream warm surface water anomalies are simulated whereas the change in sign of the ZW3 index results in negative anomalies downstream of the locations of the troughs. Similar features also appear in the surface temperature field over the oceans. Notable is also the strong impact of the ZW3 over central Australia. Around Antarctica the impact of the ZW3 on sea ice is strongly visible which is again most pronounced in the western half of Antarctica. Upstream of the troughs negative anomalies in sea ice appear for a change in sign of the ZW3, for the ridges the opposite is the case: here positive anomalies

Figure 3.17: Composite of changes between positive and negative state of the ZW3 for (a) SST, (b) SIC, (c) SLP and (d) TS. The ZW3 index was calculated according to the method proposed by *Yuan and Li* [2008]. Only values significant at the 5% level are shaded.
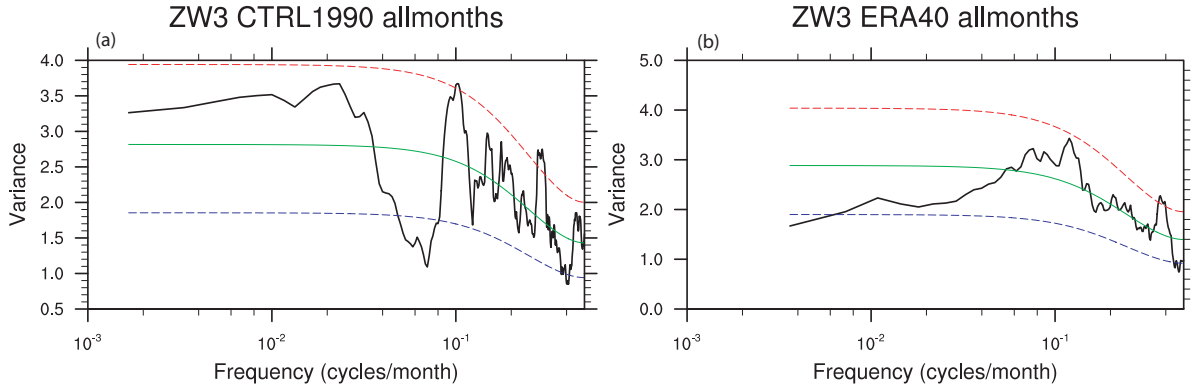
Figure 3.18: Spectra of the monthly ZW3 Index calculated for (a) the CTRL1990 simulation and for (b) ERA40 reanalysis data. The green line indicates the theoretical Markow red noise spectrum, dashed lines show its confidence bounds at the 5% and 95% levels, red indicates the upper boundary, blue indicates the lower boundary.

occur. The influence of the ZW3 on SIC has been previously noted by *Raphael* [2007]. She finds that SIC in the Antarctic is affected by alternating warm and cold air inflow from either equator- or poleward flow, respectively. This air flow affects the temperature gradient between atmosphere and ocean and results in an altered surface heat flux which subsequently influences SIC.

3.2.5 El Niño - Southern Oscillation

The El Niño - Southern Oscillation (ENSO) is a complex coupled atmosphere ocean phenomena rooted in the tropical Pacific and to date a number of indices have been compiled in order to capture the nature of this phenomenon.
Here we use the Nino3.4 index which is one of the indicators for ENSO which is based on sea surface temperatures. It quantifies monthly SST anomalies averaged over the region 5°N to 5°S and from 170°W to 120°W. Prior to calculation of the index area weighting was applied in order to account for the different sizes of the grid boxes. After obtaining the regional anomalies the average seasonal cycle was removed in order to obtain the Nino3.4 index.

Temporal behaviour of ENSO

A further important aspect of ENSO is the timing of El Niño and La Niña events. Spectral analysis of observational data shows that ENSO has a significant reoccurrence time of 3-7 years (Figure 3.22). In both the wavelet and the timeseries this period can clearly be seen. CCSM3 has as a very much more regular ENSO; here, El Niño events occur too regularly approximately every two years (Figure 3.21).

Impacts of ENSO

Figure 3.19 shows the correlation pattern of the Nino3.4 index with SST, TS, SLP and PREC in the CTRL1990 simulation. The pattern for the ERA40 reanalysis data is plotted in figure 3.20. The model is able to represent the main features of the phenomena well: As for the correlation with ERA40 surface temperature data the strong positive correlations over the
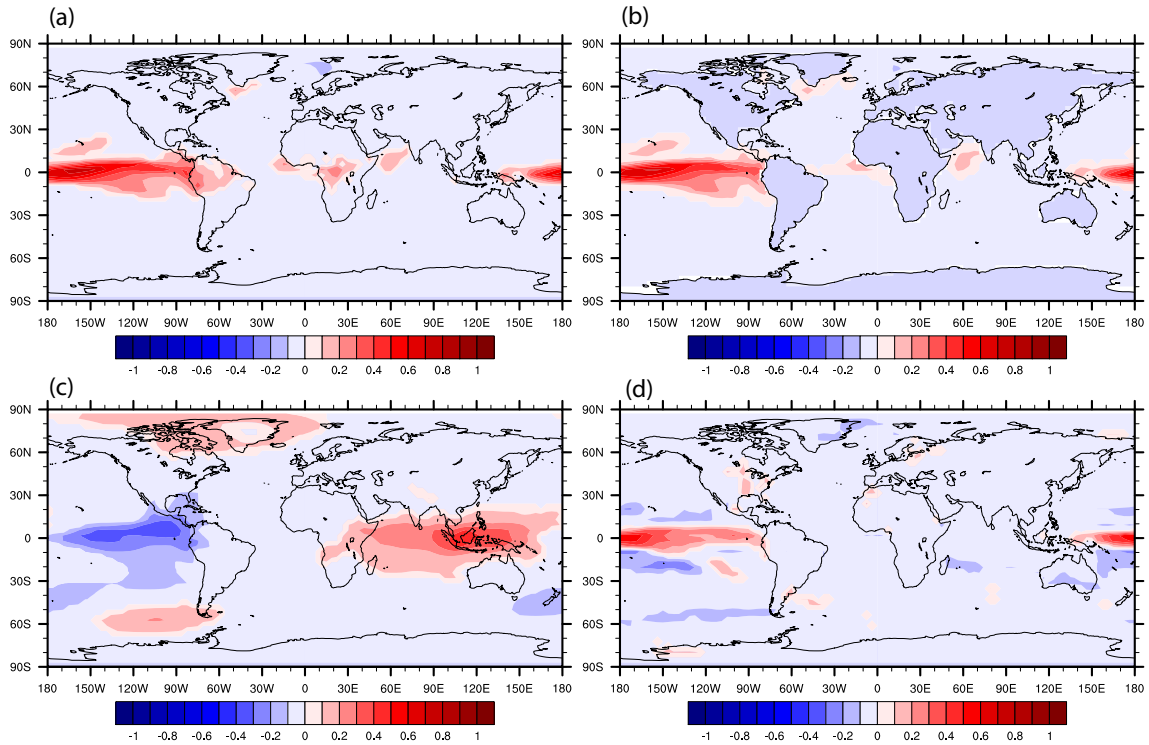
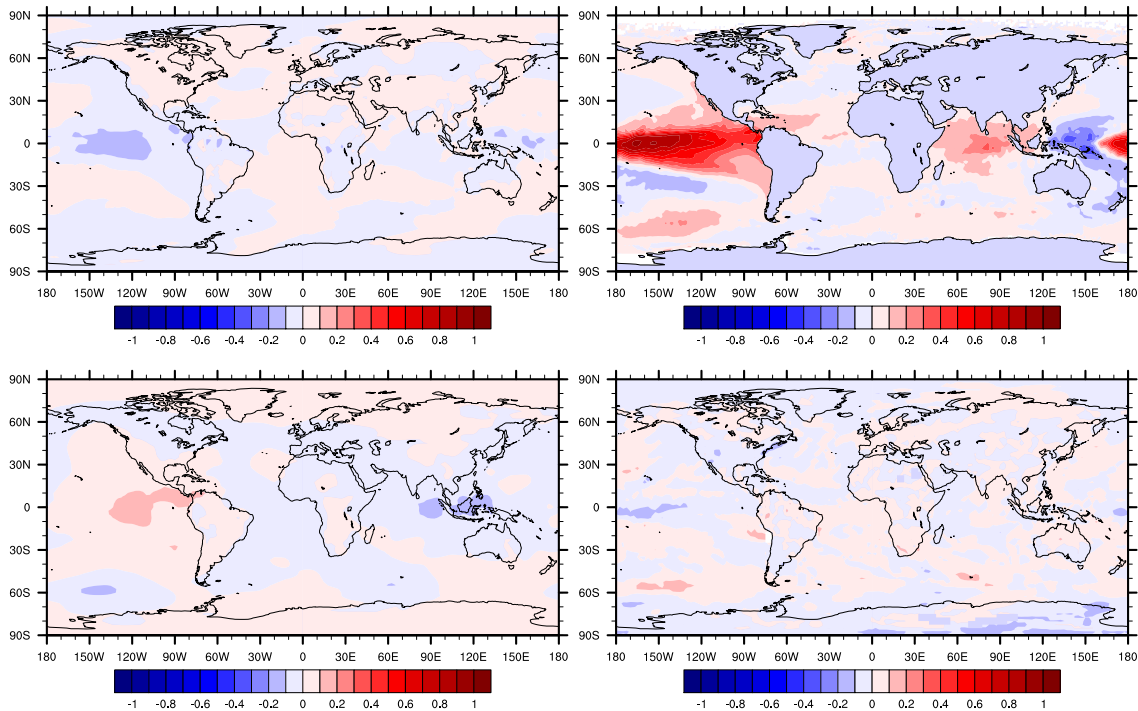**Figure 3.19:** CTRL1990 Nino34 Index correlated with (a) TS, (b) SST, (c) SLP and (d) PREC.

central Pacific and northern South America, central Africa and the Indian Ocean. The model is not able to show the significant negative correlation to the north of Indonesia and the weak but significant correlations over the South Pacific. The same is the case for the SST pattern. The model is able to well represent the correlation pattern with SLP: The strong negative correlations over the eastern Pacific are well reflected in the model, as are the positive correlations over the western Pacific. The positive relationship over the South-East Pacific is also found in the CTRL1990 simulation. The model also performs well for precipitation: A high Nino3.4 index corresponds to strong precipitation over the central Pacific and reduced values to the north and the south of this region. As for temperature the model is not able to represent precipitation anomalies over the Western Pacific as well. The negative correlations expected over Japan and Indonesia cannot be seen, however, the negative correlations east of Australia are present. Also, the negative correlation over the South-East Pacific are clearly identifyable in the model. These results suggest that, overall, the model able to well represent both the atmospheric and the oceanic component of ENSO.

3.2.6 Impacts of the variability modes on regional temperature and precipitation

In this section the linkage between regional temperature and precipitation variations for both the CTRL1990 simulation and the reanalysis data with the variability modes is evaluated. This analysis serves as prepatory work for the analyses of regional climate change in South America, South Africa and Australia presented in the following chapter. The regions used for

Figure 3.20: HadISST Nino34 Index correlated with (a) TS (ERA40), (b) SST (HadISST), (c) SLP (ERA40) and (d) PREC (ERA40).

the analyses can be found in the following chapter in Figure 3.23.

The linkage between regional temperature variations for South America and the various modes of variability in the CTRL1990 simulation (Table 3.2) generally follow the patterns found in the ERA40 (Table 3.4) quite well. In Patagonia (SAM1) each the SAM, the SPD and the ZW3, have a significant influence on temperature variability. For Central Chile and Argentine in both the model and in the reanalysis data the SPD appears as the most important mode of internal variability. The variability in the region SAM3 (central western South America) in the ERA40 data is dominated by both SPD and ENSO variability whereas neither of the two show up with a high correlation in the CTRL1990 simulation. For eastern central South America (SAM4) ENSO appears as the dominant variability mode influencing temperature in both model and reanalysis.

Both the regional temperature variations of eastern and the western part of southern South Africa (SAF1 and SA2, respectively) show a significant link to ENSO variability in the ERA40 data whereas it is not apparent in the CTRL1990 simulation. Here, the SPD shows up as the most dominant influence on temperature.

For south west Australia (AUS1) in both the model and the reanalysis data set the ZW3 appears as the leading mode. For AUS2 (south east Australia) the CTRL1990 simulation shows the same result, the ERA40 data suggests that additionally the SAM has a significant influence on temperature variability. The temperature variability in AUS3 (north western
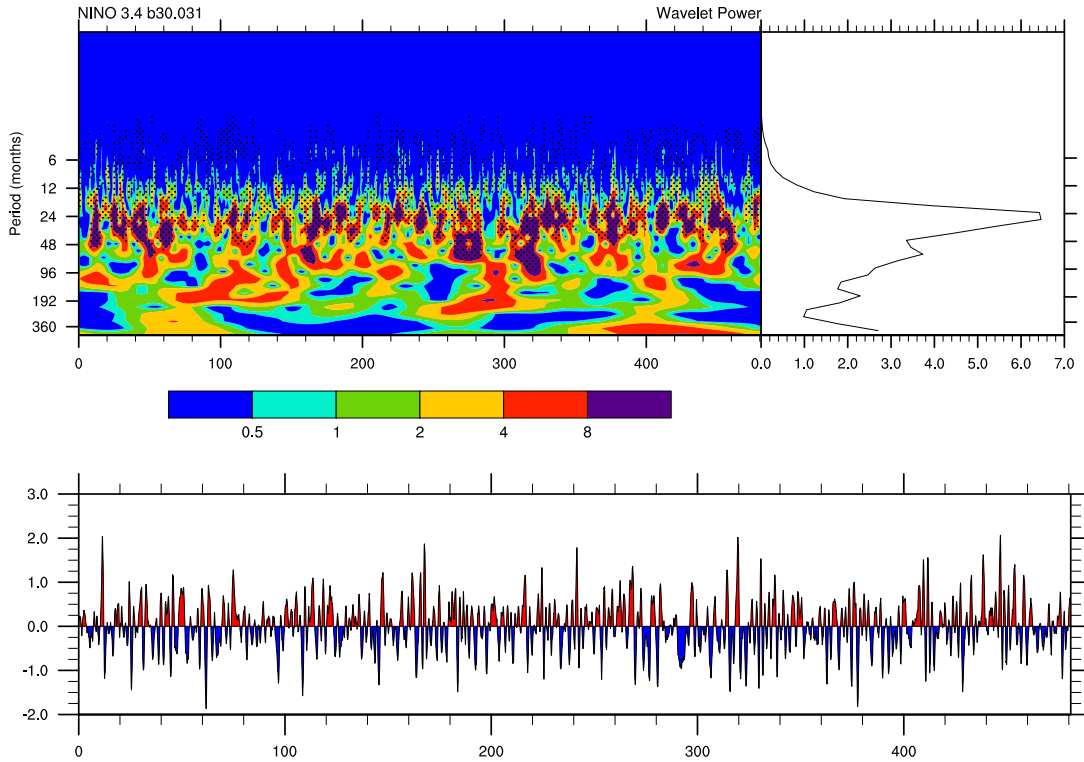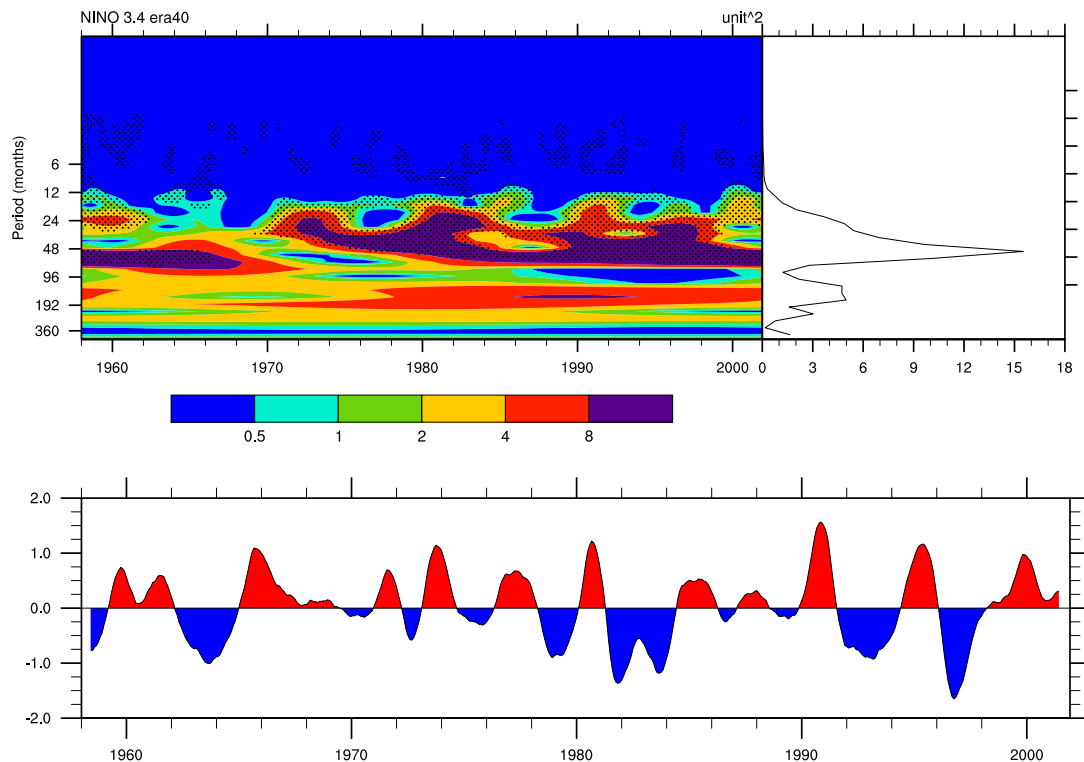
Figure 3.21: (a) Wavelet of the CTRL1990 Nino34 Index, significant (at the 5% level) values are overlaid with stipples; (b) the associated timeseries smoothed with a 12 month running average.

Australia) in ERA40 is dominated by the SAM and the ZW3 whereas the model suggests a significant influence ENSO. Both model and reanalysis data suggest that north eastern Australia is dominated by variability of the SAM.

The dominant modes of variability influencing precipitation in Patagonia are the ZW3, SAM and SPD for the model (Table 3.3). The observational data (Table 3.5), however, points to no significant influence of the ZW3 but suggests that SAM is leading mode of variability. SAM2 in both model and ERA40 appears to be influenced most by the SPD and ENSO variability. In central western South America precipitation appears to be influenced most by the SPD which both model and reanalysis confirm. No dominant mode of internal variability appears for region SAM4 for precipitation.

The ERA40 data suggests that precipitation in southern South Africa is significantly influenced by ENSO, the CTRL1990 simulation shows a similar but weaker link and implies a significant impact of the Southern Annular Mode in this region.

The dominant mode of internal variability influencing precipitation in south east Australia is the South Pacific dipole in both observations and the model. The remaining three regions in Australia are each dominated by ENSO variability which the CTRL1990 shows and the ERA40 data confirms; for each of the regions, the reanalysis, however, suggests an additional influence of the SPD which the model does not show.

Figure 3.22: (a) Wavelet of the HadISST Nino34 Index, significant (at the 5% level) values are overlaid with stipples; (b) the associated timeseries smoothed with a 12 month running average.

Table 3.2: Regional surface temperatures from the CTRL1990 simulation for South America (SAM), South Africa (SAF) and Australia (AUS) correlated with the Southern Annular Mode Index (SAM), South Pacific Dipole Index (SPD), Zonal Wave 3 Index (ZW3), Nino 3.4 Index (Nino3.4) and the Antarctic Circumpolar Current Strength (ACC). Values significant at the 1% level are labelled with (***), coefficients significant at the 5% level are marked with (**) and those at 10% with (*).

Region	SAM	SPD	ZW3	Nino3.4	ACC
SAM1	0.157***	0.159***	0.377***	-0.038***	0.117***
SAM2	-0.089***	0.179***	0.034***	-0.137***	-0.045***
SAM3	-0.082***	-0.012	-0.093***	-0.029**	-0.062***
SAM4	-0.097***	-0.147***	0.075***	0.245***	-0.104***
SAF1	-0.050***	-0.203***	0.178***	0.041***	-0.015
SAF2	-0.092***	-0.211***	0.147***	0.051***	-0.022*
AUS1	-0.013	-0.079***	0.185***	0.085***	0.026**
AUS2	-0.001	0.031**	0.185***	0.040***	0.006
AUS3	-0.051***	-0.058***	0.119***	0.140***	-0.022*
AUS4	-0.179***	0.100***	0.047***	0.140***	-0.089***
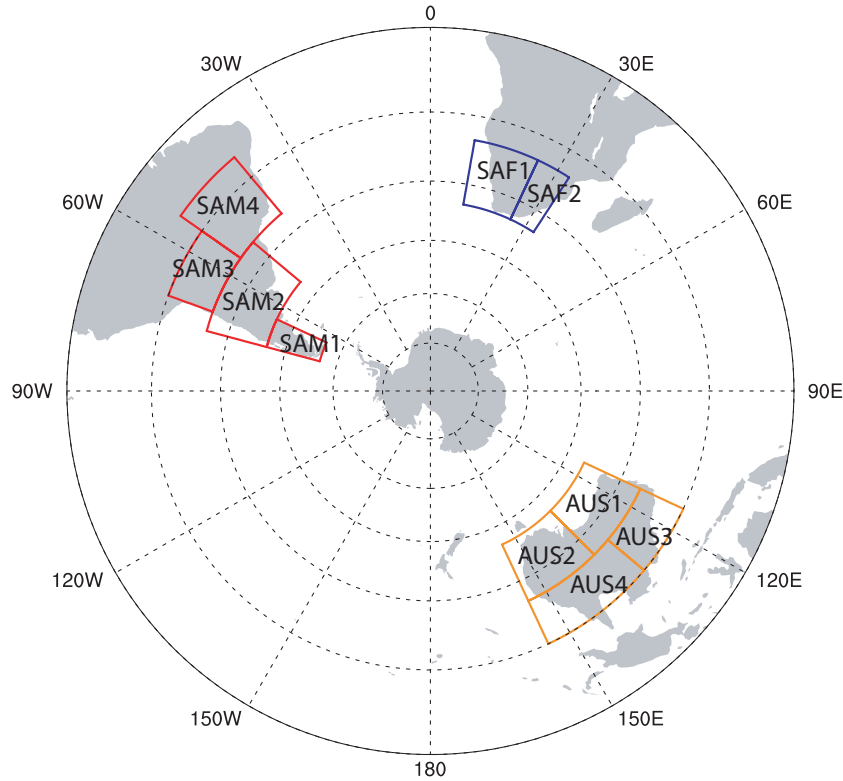
Figure 3.23: Selection of areas for regional temperature and precipitation anomalies. Red indicates areas in South America, Blue areas in South Africa, and Orange areas in Australia. The regions were selected such that variability of temperature and precipitation show a high degree of covariance within the boxes.

Table 3.3: Regional precipitation from the CTRL1990 simulation for South America (SAM 1-4), South Africa (SAF 1-2) and Australia (AUS 1-4) correlated with the Southern Annular Mode Index (SAM), South Pacific Dipole Index (SPD), Zonal Wave 3 Index (ZW3), Nino 3.4 Index (Nino3.4) and the Antarctic Circumpolar Current Strength (ACC). Values significant at the 1% level are labelled with (***), coefficients significant at the 5% level are marked with (**) and those at 10% with (*)

Region	SAM	SPD	ZW3	Nino3.4	ACC
SAM1	-0.291***	0.200***	-0.377***	-0.022*	-0.200***
SAM2	0.121***	-0.177***	0.096***	0.114***	0.098***
SAM3	0.042***	-0.107***	0.017	0.073***	0.005
SAM4	0.018*	0.044***	0.038***	-0.062***	0.025*
SAF1	0.261***	-0.075***	-0.004	0.043***	0.104***
SAF2	0.111***	0.081***	-0.100***	-0.043***	0.114***
AUS1	-0.147***	0.206***	0.070***	-0.090***	-0.090***
AUS2	0.170***	-0.086***	0.046***	-0.172***	0.047***
AUS3	0.087***	0.098***	0.029**	-0.120***	0.040***
AUS4	0.119***	0.039***	0.026**	-0.136***	0.045***

Table 3.4: Regional surface temperatures from the ERA40 reanalysis (1979 AD to 2001 AD) for South America (SAM), South Africa (SAF) and Australia (AUS) correlated with the Southern Annular Mode Index (SAM), South Pacific Dipole Index (SPD), Zonal Wave 3 Index (ZW3), Nino 3.4 Index (Nino3.4) and the Antarctic Circumpolar Current Strength (ACC). Values significant at the 1% level are labelled with (***), coefficients significant at the 5% level are marked with (**) and those at 10% with (*).

Region	SAM	SPD	ZW3	Nino3.4
SAM1	0.369***	0.284***	0.194***	-0.051
SAM2	0.044	-0.261***	-0.087	0.090
SAM3	-0.086	-0.325***	-0.261***	0.265***
SAM4	-0.057	-0.027	-0.139**	0.199***
SAF1	0.115	-0.112	-0.194***	0.217***
SAF2	0.014	-0.047	0.027	0.236***
AUS1	-0.286***	-0.264***	-0.338***	0.089
AUS2	-0.185***	-0.079	-0.156**	0.034
AUS3	-0.256***	-0.152**	-0.174**	0.112
AUS4	-0.171**	0.064	-0.039	0.047

Table 3.5: Regional precipitation from the ERA40 reanalysis (1979 AD to 2001 AD) for South America (SAM 1-4), South Africa (SAF 1-2) and Australia (AUS 1-4) correlated with the Southern Annular Mode Index (SAM), South Pacific Dipole Index (SPD), Zonal Wave 3 Index (ZW3), Nino 3.4 Index (Nino3.4) and the Antarctic Circumpolar Current Strength (ACC). Values significant at the 1% level are labelled with (***), coefficients significant at the 5% level are marked with (**) and those at 10% with (*)

Region	SAM	SPD	ZW3	Nino3.4
SAM1	-0.308***	-0.156**	0.069	-0.019
SAM2	-0.193***	-0.301***	-0.180**	0.290***
SAM3	0.004	0.111	0.075	-0.009
SAM4	0.021	0.060	0.101	-0.011
SAF1	0.065	0.058	-0.024	-0.202***
SAF2	0.132*	0.119*	0.045	-0.250***
AUS1	-0.106	0.206***	0.159**	-0.080
AUS2	0.081	0.347***	0.003	-0.177**
AUS3	0.093	0.184***	0.096	-0.190***
AUS4	0.074	0.214***	0.013	-0.260***

3.3   Discussion

The results of the previous sections show that, overall, CCSM3 is able to simulate the main features of the Southern Hemisphere mean climate and the dominant modes of atmospheric variability. Several issues however, arise due to biases in the model climatology. One problem previously noted by e.g., *Yeager et al.* [2006] or *Collins et al.* [2006] lies in the too zonal behaviour of the model with respect to the atmospheric dynamics which leads to an over-estimation of the strength of the mid latitude westerly winds. Also, in the low resolution version of the model an unrealistic shift of the storm tracks in equatorial direction has been found which, however, at some latitudes leads to a better agreement with the observations (e.g., at 55°S) [*Yeager et al.*, 2006]. This bias has also been noted in the assessment of the model ensemble used for the IPCC AR4 [*Randall et al.*, 2007]. Most of these models also overestimate the strength of the Southern Hemisphere polar easterlies, thus increasing the pressure gradient between the mid and high latitudes.

This bias also impacts on the variability modes such as the Southern Annular Mode. The model overestimates the pressure gradient between the polar latitudes and the Southern Hemisphere mid latitudes, and hence the wind speeds masking other modes of variability in this area. SAM in the model explains 10% more variability than in the observations. In contrast to the results of this study, *Raphael and Holland* [2006] find that in 20th century simulations with the high-resolution CCSM3 that SAM has a weaker amplitude if the difference between the positive and the negative center of action is taken as measure of the impact of SAM. Furthermore, they find that the model underestimates the impact of SAM on the zonal wind speed by more than a factor of 2. Here, the strength of the impact of SAM was evaluated by a regression of the index onto Z850hPa and shown as a composite between the SAM positive and SAM negative phases. These differences, of course, may be a result of both the different resolution but also of the different model setup, i.e. the applied forcing. Also, the CCSM3 simulation the authors applied ozone forcing whereas this factor is not present in the version of CCSM3 used for this study. Similar to the findings in this study most of the IPCC AR4 models also overestimate the impact of SAM on surface pressure, indicating that these models also show an enhanced zonal component in comparison to the observations. The temporal variations in the SAM index in the CTRL1990 and the ERA40 data showed a rather white spectrum whereas *Raphael and Holland* [2006] using NCEP data and the 20th century CCSM3 simulation found a significant peak at 16 years. The authors, however, note that this peak is presumably a result of reduced natural variability through ensemble averaging of the SAM index.

CCSM3 shows greater problems in adequately representing the Semiannual Oscillation. Especially the representation of the annual cycle of temperature at the 500hPa level is strongly biased. This has also been found by *Ackerley and Renwick* [2010]. For sea level pressure two distinctive peaks appear, however, they are not located at the correct months. These errors are partly related to a lacking representation of the Antarctic Circumpolar Trough (CPT). *Raphael and Holland* [2006] find that the representation of both the annual cycles of SLP at 50°S and 65°S show generally too low SLPs which were also noted in section 3.1.1. They suggest that the errors in the correct representation of the SAO lie in the incapability of the model to simulate the temperature cycle at 50°S leading to a too deep CPT. Due to the insufficient representation of this phenomenon the SAO will not be considered in the further

analysis.

The ZW3 pattern is well represented in CCSM3, however, shows errors in the exact location of the wave crests and troughs. Even though a different method was applied for the calculation than suggested in *Raphael* [2004] the patterns of variability appear similar with both methods. The index by *Raphael* [2004] specifies the ridge areas of the pattern whereas calculating the 1st EOF of V500hPa allows one to determine the location of the ridges from the actual variability pattern. Both patterns compare well which can be seen in a comparison with Figure 8d in *Raphael and Holland* [2006]. Similarly, CCSM3 is able to capture the observed effect [*Raphael*, 2007] of this variability mode on sea ice variability well suggesting that the dynamics behind this variability mode are well represented. Also notable are the strong and significant impacts (regression analysis) of the ZW3 on surface temperatures over southern South America, South America and Australia indicating that changes in this variability pattern due to external forcing may show a significant impact on climate in these areas. Nevertheless, due to the shift of the pattern which may be related to a poor representation of the local topography, care needs to be taken when assessing regional changes induced by this mode.

The South Pacific dipole, also known as the Pacific South America pattern, also shows up in the CTRL1990 simulation. However, one of the problems arising is the shifted position of the Amundsen low pressure system which, for example, evokes an incorrect sea ice response. This problem is not found by *Timmermann et al.* [2010] in a preindustrial control simulation with the medium resolution version (T42) of CCSM3 suggesting that the resolution of the model may impact on the ability of simulating this phenomenon for example by insufficiently resolved topographic features. This variability mode has previously been liked to ENSO variability [*Kiladis and Mo*, 1998; *Renwick*, 2002]. The spectrum calculated for the ERA40 SPD indeed shows a significantly red behaviour between 2 and ~ 20 years with a peak at 8 years which closely corresponds to the spectrum of Nino3.4. Also an ENSO signal is clearly visible in the regression pattern of the SPD onto TS. For the model this, however, is not the case. Additionally, the responses of surface temperatures and sea ice to the SPD appear weaker than in the observations. *Raphael and Holland* [2006] attribute this to the altered ENSO variability in CCSM3 which takes place on at higher frequencies than observed, thus, reducing the period of time given for anomalies to accumulate in, for example, the sea ice system between an El Niño and a La Niña event. Due to the errors in the representation of this variability pattern changes in the mode and their impacts need to be treated with care when a time-varying external forcing is applied to the simulations.

As addressed by a number of previous studies, e.g. *Deser et al.* [2006], the ENSO variability in CCSM3 has a too high frequency and the band of SST anomalies in the tropical Pacific extends too far westwards. They also note difficulties of the model to represent the expected positive minus negative ENSO composite. Especially the precipitation patterns show large errors. A phenomenon also noted in *Yeager et al.* [2006] is the double ITCZ precipitation anomaly. This stands in contrast to a single ITCZ located north of the equator in observations which shifts southward during an El Niño event. Their work on the medium resolution of the model also shows that the response over the Southern Ocean shows a strong tendency to the positive phase of the SAM, i.e. exhibiting a strong zonal symmetry, during a positive ENSO event which is not the case for the observations. Also it can be seen that the SST/TS and precipitation responses especially over Southern South America do not conform to the

expected pattern. This indicates that the ENSO teleconnections may be not well represented in the model as also suggested for the SPD which is closely linked to ENSO, and that this mode thus needs to be treated with care in the transient simulations and the regional analysis.

The estimates given for the strength of the ACC by *Whitworth* [1983] and *Whitworth and Peterson* [1985] lie around 134 ± 13 Sv fitting the range of the model ACC well. One problem arising in the transient simulations noted earlier may be given by the position of the maximum Southern Hemisphere westerlies which are shifted northward. It was shown by *Gent et al.* [2001] that the strength of the ACC in numerical models depends mainly on the wind stress at Drake Passage latitudes and on the thermohaline circulation off Antarctica driven by brine rejection through sea ice formation. A shift from present day forcing to preindustrial levels shows no effect on the strength of the ACC in the low resolution version of the model, however, leads to a significant increase of the ACC in the medium resolution version [*Otto-Bliesner et al.*, 2006]. The authors also note that it may be the position and the strength of the Southern Hemisphere westerlies causing this difference and making the coarse version of the model less sensitive to changes in external forcing. A further problem arising could be the too extensive sea ice in the model which is especially pronounced in the low resolution of the model which could also affect the thermohaline circulation off Antarctica. Again this is a parameter which shall be analyzed in the transient simulation but needs by evaluated with caution due to the errors of the model.

The values for the Agulhas leakage found in the CTRL1990 simulations fit estimates by [*Biastoch et al.*, 2009] well. They find values of average values around 54 Sv for yearly data with anomalies that lie around 2 Sv. For the 20th century the authors note a significant strengthening of the Aguhlas leakage which they attribute to a shift in the westerly winds. Therefore, a comparison of the transient simulations will provide an intriguing opportunity to examine the Agulhas leakage under varying external forcing.

As noted previously by many authors (e.g., *Yeager et al.* [2006]) CCSM3 shows a too large sea ice extent. The major errors are found to occur during wintertime whereas from the previous version of CCSM the sea ice area estimates have improved for the summer, thus indicating the reason for the too large seasonal differences in SIA in the CTRL1990 simulation. The largest errors in SIA occur in the Weddell and the Bellingshausen-Amundsen Sea as can be seen in Figure 12 in *Yeager et al.* [2006]. One reason for these errors given by the authors is biases in the winds. Furthermore, the representation of ocean currents and the heat transfer from ocean to the ice may place a role in forming the extensive sea ice. Further information on the sea ice in CCSM3 can be found in *Holland et al.* [2006]. It can be concluded that even though a number of biases in both the mean climate and the variability modes exist the model is able to simulate the most dominant mid and high latitude phenomena of the Southern Hemisphere and thus can be used as a tool to explore past climate variations in the Southern Hemisphere.

3.4   Excursus: Antarctic sea ice variability and its links to the Amundsen low pressure system

In this section the linkage between regional sea ice variability in Antarctica and the Southern Annular Mode shall be analyzed. For this observational data from the HadISST SIC dataset and the ERA40 reanalysis shall be used and will be compared to the CTRL1990 simulation.

In recent decades a significant increase in Antarctic sea ice area (SIA) has been observed [*Stammerjohn and Smith*, 1997; *Cavalieri and Parkinson*, 2008]. During the same period the Southern Annular mode has exhibited a positive trend which is possibly a result of ozone depletion or the increase in Greenhouse gases [*Thompson and Solomon*, 2002; *Kushner et al.*, 2001]. However, so far no clear link between the SIA changes and the trends in the SAM index on a hemispheric scale could be found [*Lefebvre et al.*, 2004]. Thus, here the regional changes in both SLP and the SIA shall be analyzed.

The main SIA variability in Antarctica takes place in form of a dipole pattern, the so-called Antarctic dipole, with opposing poles in the Bellingshausen-Weddell Sea and the Amundsen-Ross Sea [*Lefebvre et al.*, 2004]. The Amundsen low pressure system exhibits an important influence on the state of the dipole. Recently, a shift towards more cyclonic condition has been observed and attributed to stratospheric ozone depletion [*Turner et al.*, 2009].

The following questions shall be addressed with the analyses performed:

1. Where does the sea ice increase take place?
2. Where do the trends in the SAM occur?
3. How does the dipole pattern relate to the hemispheric sea ice trend?
4. How does the state of the Amundsen low influence the sea ice trends?
5. Can the model validate the findings in the observations?

Data

For the analyses monthly sea level pressure data (SLP) from the NCEP-NCAR reanalysis project ranging from 1979 to 2008 AD [*Kalnay et al.*, 1996] is used. It has a horizontal resolution of $2.5° \times 2.5°$. For the monthly sea ice variations the HadISST SIC dataset is used which has a spatial resolution of $1° \times 1°$. For the model the high resolution (T85) version of CCSM3 is used and the CTRL1990 simulation with perpetual 1990 AD forcing is analyzed. The model has a horizontal resolution of $1.4° \times 1.4°$ and 26 hyprid sigma pressure levels in the vertical.

Results

Figures 3.24 (a) and (b) show the relationship between regional sea ice and sea level pressure changes. The Amundsen low pressure system varies synchronously with sea ice in the western half of Antarctica in form of a dipole pattern. A switch in sign of the pressure anomalies over the Amundsen Sea corresponds to a change in sign of the dipole in the sea ice. Furthermore, SLP changes in the eastern half of Antarctica show a similar behavior as sea ice in this area. A comparison between regional sea level pressure changes and the corresponding SAM index (calculated according to *Gong and Wang* [1999]) (Figure 3.24 (a) and (c), respectively)
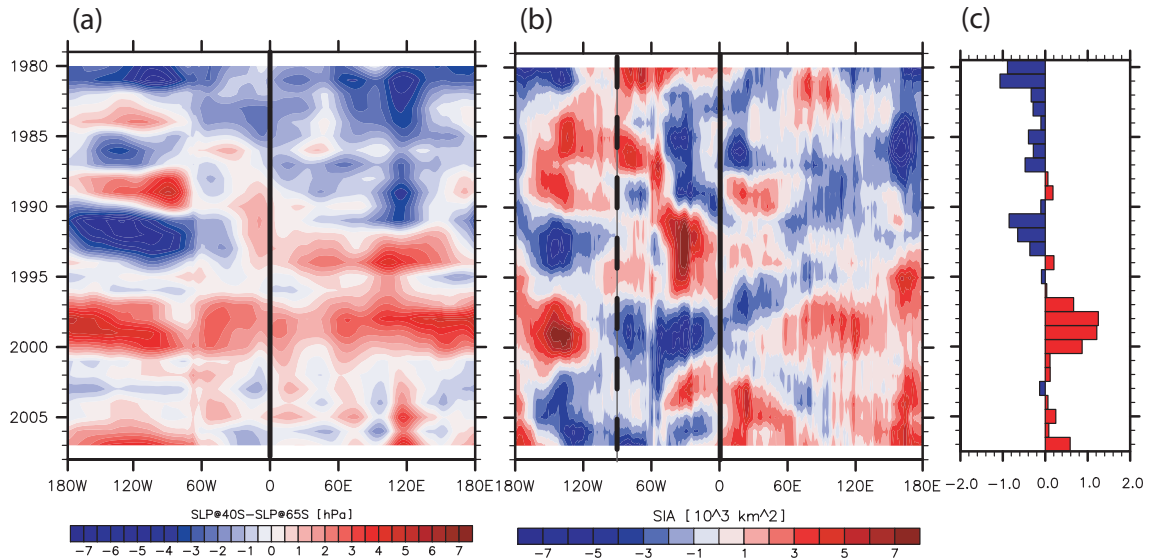
Figure 3.24: (a) Anomalies of the SLP difference between 45 and 60°S from the NCEP-NCAR reanalysis, (b) SIA anomalies from the HadISST SIC dataset and (c) annual SAM index calculated according to *Gong and Wang* [1999] from the NCEP-NCAR renanalysis from 1979 to 2008
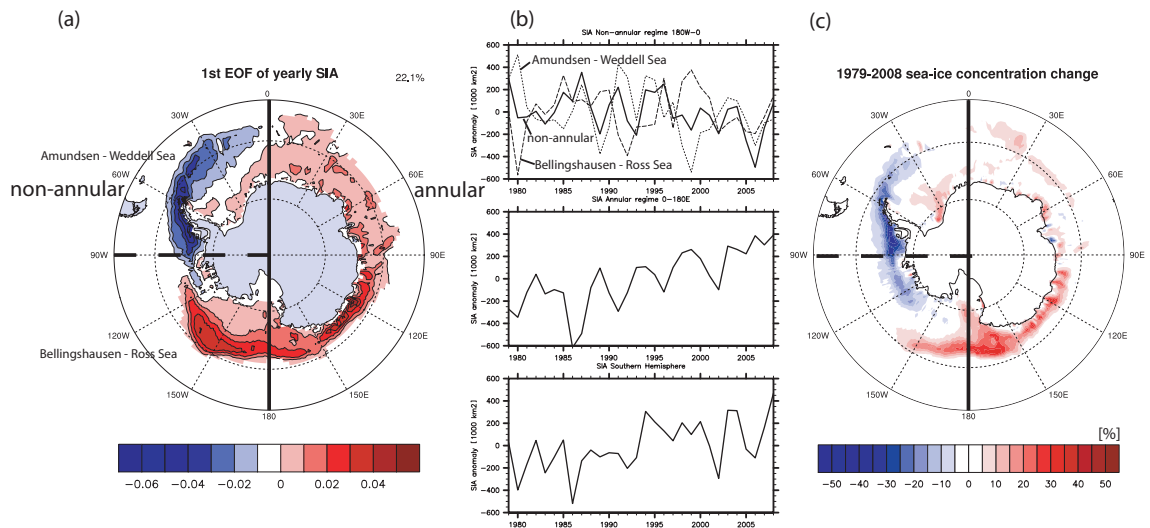
Figure 3.25: (a) EOF1 of yearly mean HadSST1 SIC and the corresponding two-regime approach. Area weighting was applied prior to calculation. (b) Timeseries of HadSST1 SIA anomalies for the non-annular regime (top), annular regime (middle) and hemispheric SIA anomalies. (c) Trend in the HadISST SIC between 1979 and 2008 AD.
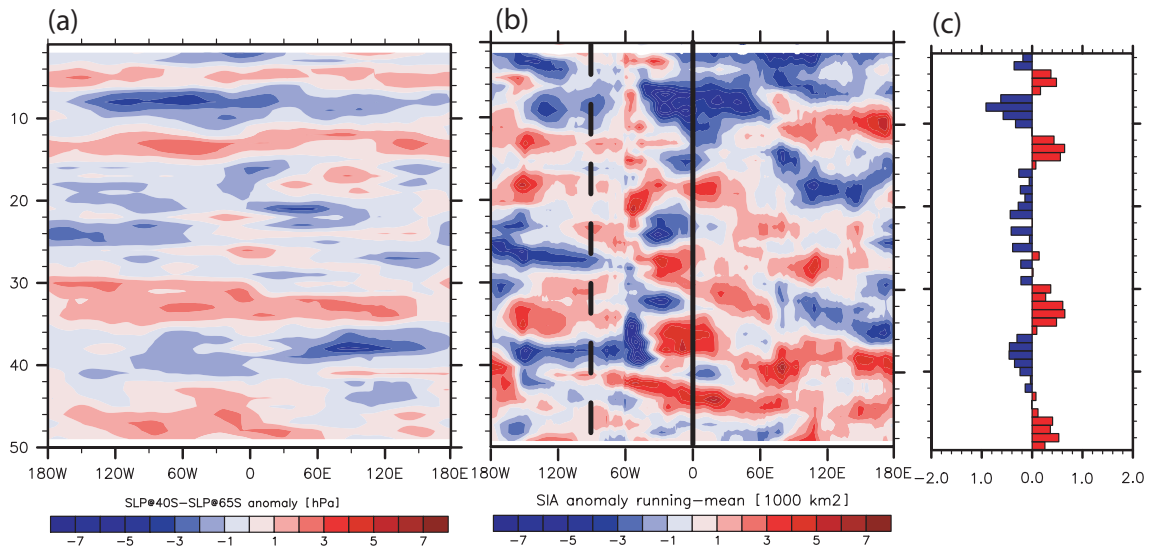
Figure 3.26: (a) Anomalies of the SLP difference between 45 and 60°S, (b) SIA anomalies and (c) annual SAM index calculated according to *Gong and Wang* [1999]. Each were are shown for 50 years from the CTRL1990 simulation.

shows that the Amundsen low pressure system changes independently of the remaining zonal SLP anomalies and determines the high frequency behaviour of the SAM index. Therefore, a two-regime approach is taken for the subsequent analysis: an annular regime for the eastern half of Antarctica (0°E to 180°E) and a non-annular regime for the western half of Antarctica (180°E to 0°E) which is validated with the calculation of the 1st EOF of SIA (Figure 3.25 (a)).

It can be seen that the main variability indeed takes place in form of a dipole in the non-annular regime and that the subdivision of the non-annular regime into the Amundsen-Weddell (AWS) and Bellingshausen-Ross Sea (BRS) can indeed be justified. Figure 3.25 (b) shows the timeseries of the SIA anomalies for each of the regimes and the hemispheric mean and in Figure 3.25 (c) the spatial pattern of the SIC concentrations over the last 30 years can be seen. Both Figures support the notion that the SIA trends originate in the annular regime. In the dipole region the anomalies in each the AWS and the BRS cancel each other out; thus this region does not contribute to the hemispheric trend. In fact, a slightly negative trend can be observed for sea ice in the non-annular regime.

As these results are somewhat limited due to only 30 years of data coverage in this area one goal of the analyses is to find out whether the CCSM3 can represent the results presented in the previous section in order to analyze the underlying dynamics of the changes in greater detail.

Unfortunately, this is not the case. Figure 3.26 shows the regional SLP and SIA variations together with the SAM index over 50 years in the CTRL1990 simulation and it can be seen that the model does not show the pronounced two-regime behavior found for sea ice in the observations, nor does the independent behavior of the Amundsen low pressure system show up. The model exhibits a too zonal behavior which was noted in the discussion section

CCSM3 T85 1st EOF of yearly SIA
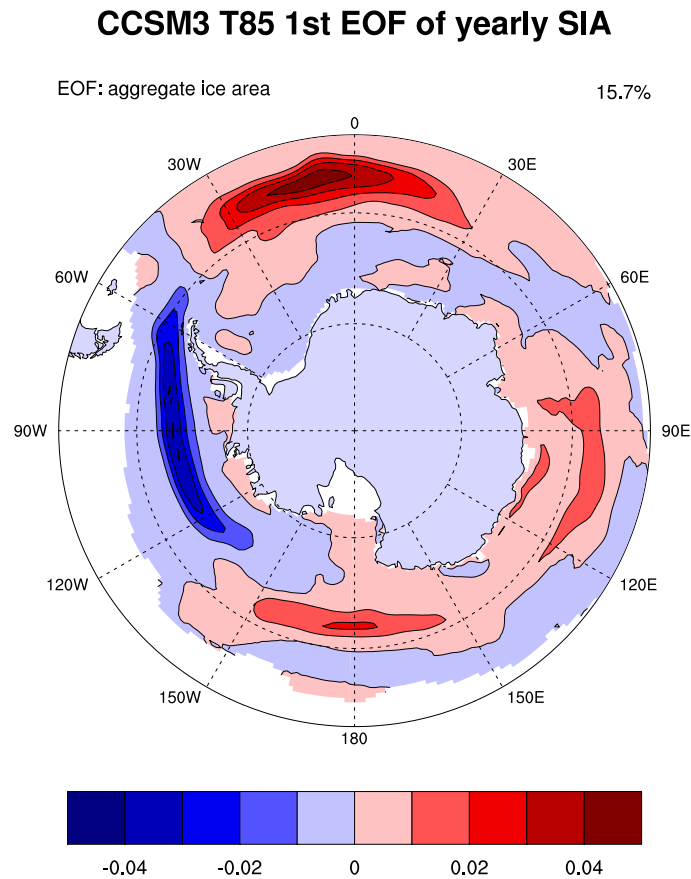
Figure 3.27: 1st EOF of yearly SIC from the CTRL1990 simulation. Area weighting was applied prior to calculation.

earlier in the chapter. Furthermore, the analysis of the main variability pattern of sea ice concentration (Figure 3.27) shows that indeed the variability takes place as a dipole pattern, that however, in the CTRL1990 simulation the dipole is shifted by approximately 45°E and that less variability is explained by this pattern. The analyses were repeated for both the high resolution version of CCSM3 and for the transient simulations; however these also fail to represent the pattern expected from the observations. A more detailed discussion on the shortcomings of the model can be found at the beginning of this chapter.

Discussion and Conclusion

Therefore, it can be concluded that the positive SIA trend originates in the annular regime, whereas the dipole in the non-annular regime cancels out the trend in this region. The Amundsen low pressure system explains the high frequency variability of the SAM index and affects the state of the dipole. Furthermore, contrary to the findings by *Turner et al.* [2009] ozone depletion resulting in a strengthening of the Amundsen low should not be responsible for the hemispheric trend in sea ice area as the changes in the BRS cancel out with changes in the AWS. However, the results do agree with the findings of a number of authors [*Hall*

and Visbeck, 2002; *Turner et al.*, 2009] that an increase in the Southern Annular Mode and
thus an increase in the westerly winds results in an increase in Antarctic sea ice through
anomalous divergent flow at the margins of Antarctica. However, the mechanisms resulting
in the trend in the SAM index remain in question. As discussed in the next chapter (Section
4.6.1) it is presumably the result of both ozone depletion and the increase in greenhouse gases
[*Thompson and Solomon*, 2002; *Arblaster and Meehl*, 2006].

Chapter 4

Results

In this chapter the results of the transient simulation ranging from 1500 AD to 2000 AD shall be introduced. The analysis will focus on detecting changes in atmospheric variability during the last 500 years and their impacts on the sea ice - ocean system and vice versa. Also, regional climate change shall be analysed for several areas of South America, South Africa and Australia in order to allow comparisons to proxy reconstructions. In a third section the direct impact of the time varying external forcing will be evaluated.

4.1 Climate Variability

In this section changes in the main variability patterns of the mid- and high latitude Southern Hemisphere, namely the Southern Annular Mode, the South Pacific Dipole and the Zonal Wave 3 pattern, will be analysed and discussed.

4.1.1 Southern Annular Mode

Figure 4.1 shows the ensemble mean time series of the Southern Annular Mode for all months, austral winter (JJA) and austral summer (DJF). When year round data are considered it can be seen that during the 16th century SAM prevails in a negative state. At $\sim$ 1650 AD a short shift to more positive conditions occurs, which is followed by a switch to a negative index around 1690 AD. The first half of the 18th century is marked by strong variability in the SAM index whereas the variations become less pronounced during the second half, a pattern which continues throughout the 19th century. One exception can be found at 1800 AD where two pronounced shifts to SAM negative conditions occur corresponding with two strong volcanic eruptions. During the 20th century a generally positive trend in the SAM index can be seen. A similar pattern emerges for the austral winter. During the middle of the 16th century and around 1680 AD the SAM index shows strongly negative values; from the middle of the 18th century to the end of the 19th century variability appears to be weak, and then during the 20th century a shift to a positive SAM index takes place. For austral summer the trend from a negative to a positive SAM index appears even more pronounced. From 1500 AD to the middle of the 18th century the SAM remains in a negative state, exceptions occurring at 1560 AD and 1760 AD. As seen for both winter and year round values variability seems reduced during the late 18th and early 19th century. Again a pronounced shift to a positive SAM index can be seen during the 20th century.

A more positive SAM index is expected to be related to stronger westerly winds in the mid latitudes [*Thompson and Wallace*, 2000]. Figure 4.2 shows the ensemble mean zonal wind speed changes for each season. It can be seen that changes in the wind speed and position do not occur until the end of the 20th century and are most pronounced during the summer months (DJF), as are the changes in the SAM index.

4.1.2   South Pacific Dipole

In Figure 4.3 the timeseries of the ensemble mean SPD for monthly data are shown. As the SPD pattern does not emerge clearly on a seasonal scale only year round data is considered. During the early 16th century several oscillations with a period of approximately 10 years are identified. During the middle of the century the index remains in a positive state for several decades. Towards the end of the century oscillations with a similar frequency as at the beginning occur. During the first half of the 17th century the index shifts to negative conditions in which it remains until $\sim$ 1680 AD; thereafter decadal oscillations are again found, however combined with a shift to a more negative SPD. The most negative values of the timeseries are found around 1760 AD. Up to 1800 AD the index remains in a more positive state. At the beginning of the 19th century two marked negative excursions can be seen. From $\sim$ 1900 AD to 1930 AD the SPD index shows consistently negative values; during
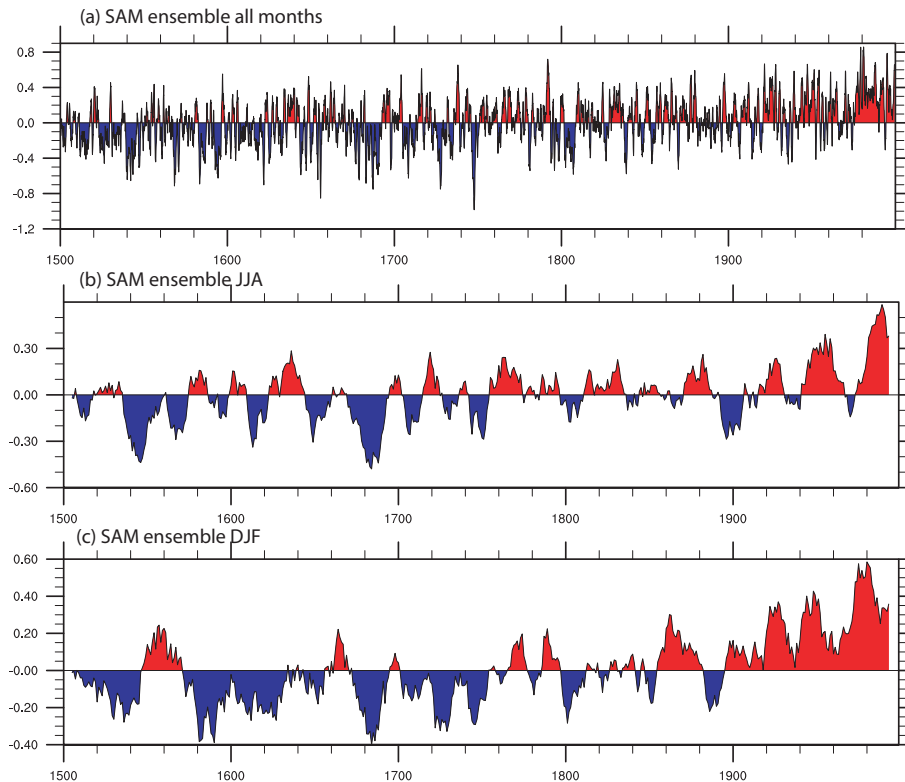
Figure 4.1: SAM index ensemble mean for (a) all months, (b) JJA and (c) DJF. The SAM index was calculated by projecting the 1st EOF pattern of Z850hPa, 20°S to 90°S, calculated from the CTRL1990 simulation for all months, JJA, and DJF, respectively, onto the Z850hPa anomalies in the transient simulations. The ensemble mean was obtained by averaging the SAM indices calculated for the respective simulations.
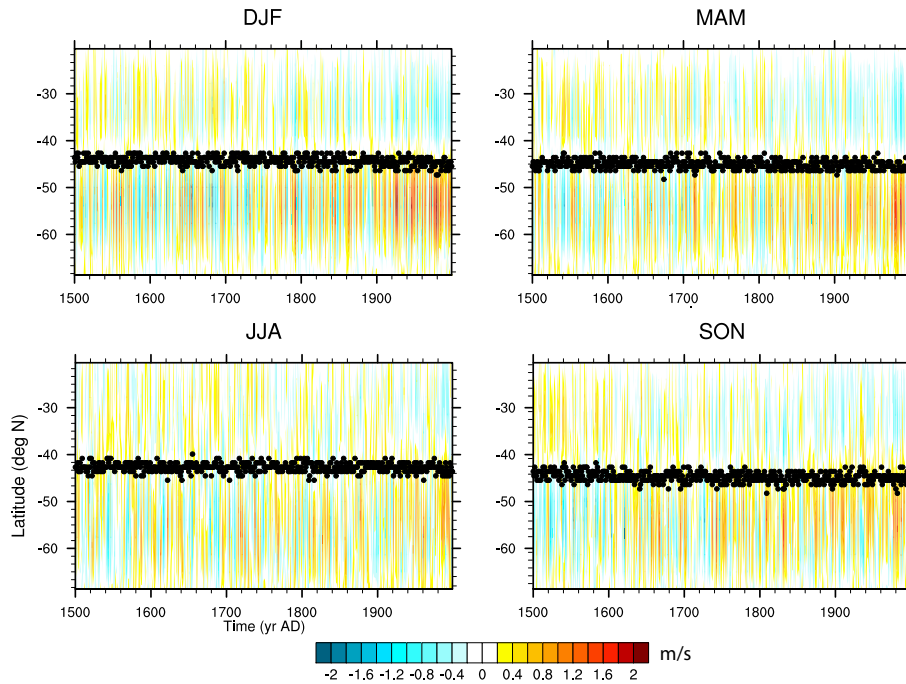
Figure 4.2: Ensemble averge seasonal zonal wind speeds anomalies versus the preindustrial mean (shaded) and the position of the maximum westerly wind speeds (black dots).

the next 30 years the opposite is the case. During the latter half of the 20th century the index again shows oscillations.

4.1.3   Zonal Wave 3

Figure 4.4 shows the ensemble mean monthly ZW3 index for the transient simulations. The index exhibits no significant trends and analysis of the individual ZW3 timeseries of the respective simulations show little common variance or shifts in amplitudes. During the late 17th and early to mid 18th century the index shows a tendency to negative values, especially, between 1740 AD and 1760 AD. Further prominent shifts to negative values can be seen at
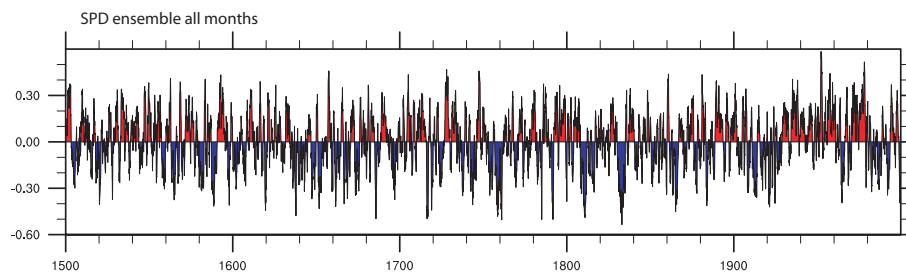
Figure 4.3: SPD index ensemble mean for all months. The SPD index was calculated by projecting the 2nd EOF pattern of Z850hPa, 20°S to 90°S, calculated from the CTRL1990 simulation for all months onto the Z850hPa anomalies in the transient simulations. The ensemble mean was obtained by averaging the SPD indices calculated for the respective simulations.

1810 AD and 1840 AD. A predominantly positive index is found around 1830 AD and 1910 AD. Overall, the simulations indicate that few simultaneous changes in the ZW3 phenomena occurred, and that the amplitude of the variability mode did not change; thus suggesting it was not affected by external forcing.

4.1.4   ENSO

In this section it will be briefly analysed whether changes in frequency and/or amplitude of ENSO variability occurred in the ensemble of transient simulations during the last 500 years. In Figure 4.5 the wavelet for run TR01 is shown as an example. The wavelets for the remaining three simulations show a very similar behaviour. Throughout the simulations the main periodicity of the variations remains around 2 - 3 years. Figure 4.6 shows the 30 year running variance of the Nino3.4 Index for each of the simulations and the ensemble mean. No long term shifts in amplitudes of the events can be seen; however, it is notable that the amplitude of the ENSO events during the Maunder Minimum was slightly but not significantly increased. Hence it can be concluded that the simulations do not indicate any significant changes to the ENSO phenomena induced by the varying external forcing.
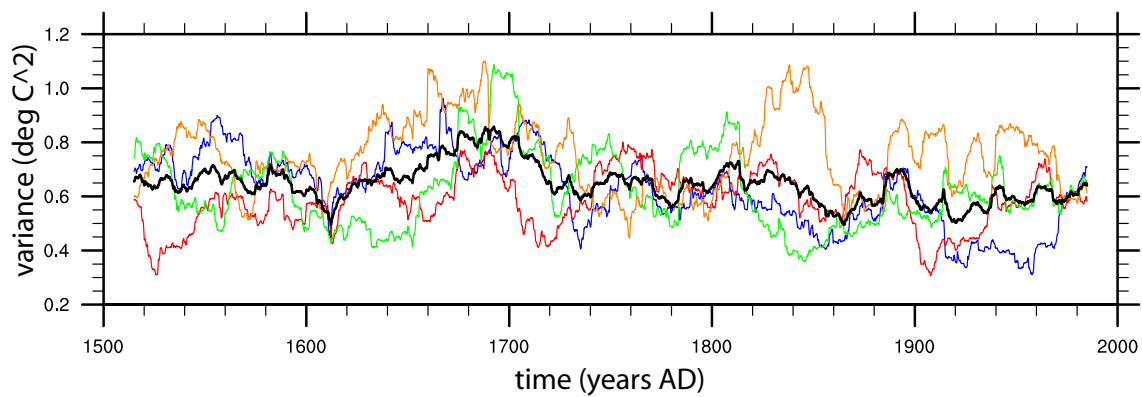
4.1.5   ACC

The timeseries of the Antarctic Circumpolar Current through the Drake Passage is shown in Figure 4.7 for each of the ensemble members and the ensemble mean. The ensemble mean ranges between 125 Sv and 131 Sv with an average of 126.75 Sv. Approximately 95% of the values of the ensemble mean lie within the range 123.39 Sv to 130.11 Sv. These are very similar values as found in the CTRL1990 simulation and no significant outliers can be seen for the ensemble mean, thus suggesting that no significant changes in the strength of the ACC through the Drake Passage occurred in the ensemble of simulations. Notable, however, is the decrease in the strength of the ACC between 1700 AD and 1800 AD by approximately 4 Sv and the abrupt increase in strength by 3 Sv at about 1820 AD which can be seen in each of the ensemble members. These fluctuations, however, lie well in the range of expected variability.
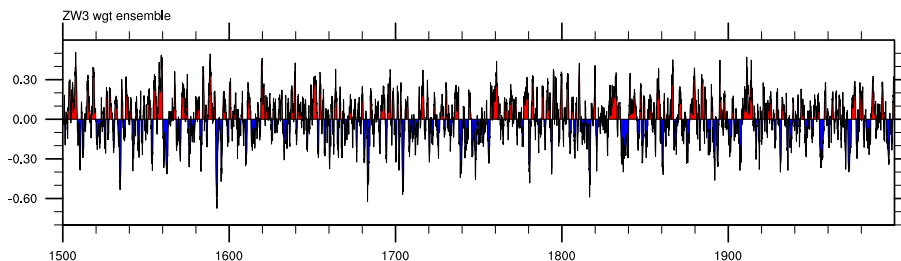
Figure 4.4: ZW3 index ensemble mean for all months. The ZW3 SPD index was calculated by projecting the 1st EOF pattern of V500hPa, 30°S to 90°S, calculated from the CTRL1990 simulation for all months onto the V500hPa anomalies in the transient simulations. The ensemble mean was obtained by averaging the ZW3 indices calculated for the respective simulations.
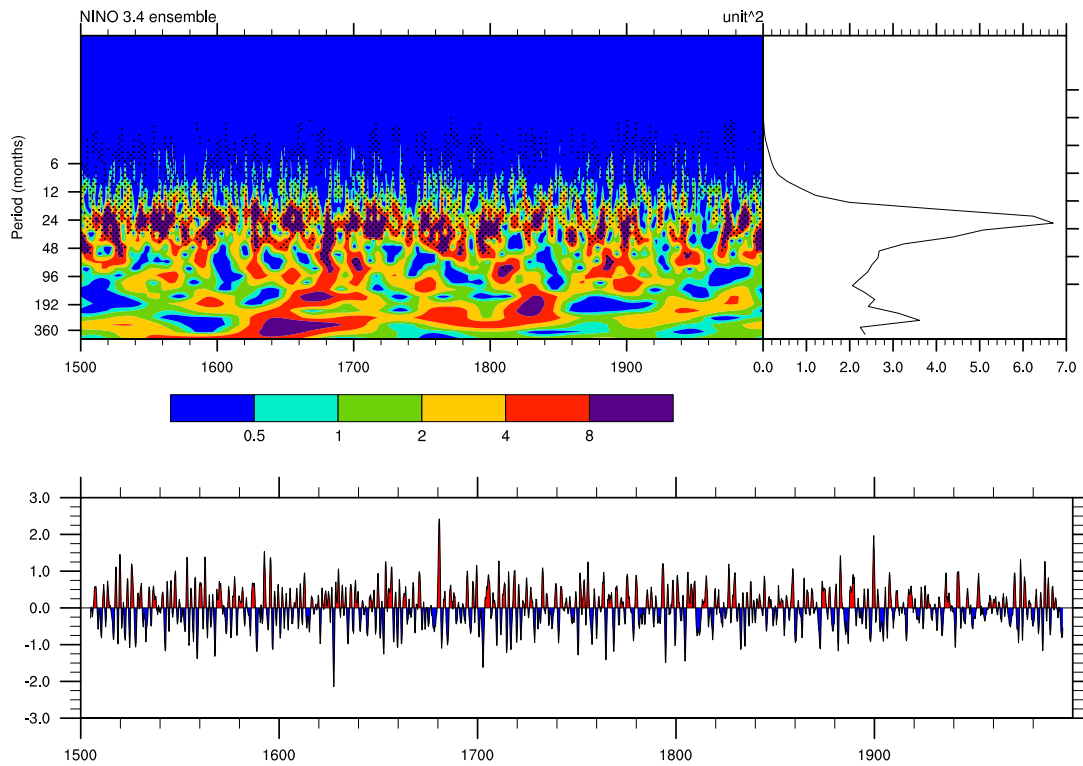
Figure 4.5: (a) Wavelet of the Nino34 Index calculated for the TR01a simulation, significant (at the 5% level) values are overlaid with stipples; (b) the associated timeseries smoothed with a 12 month running average.

Figure 4.6: 30 year running variance of the Nino34 Index calculated for the TR01a (blue), TR01b (red), TR01c (green) and TR01d (orange) simulation.
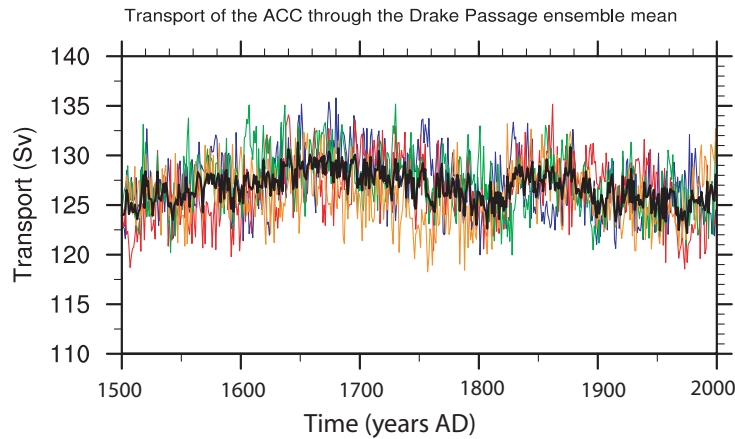
Figure 4.7: Annual average Antarctic Circumpolar Current through the Drake Passage [Sv] calculated for the ensemble mean; the respective ensemble members are shaded red, orange, blue and green; the ensemble average is the black line..
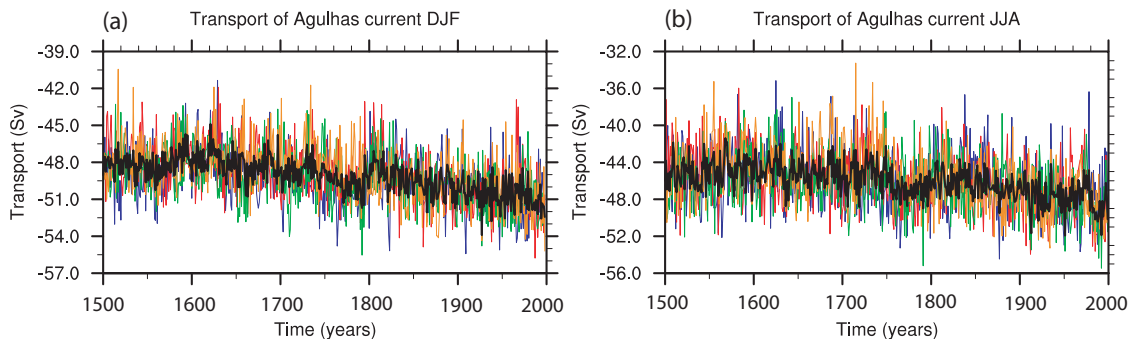
4.1.6 Agulhas leakage

The timeseries of the strength of the Agulhas leakage for the ensemble and ensemble mean for both austral summer and winter is shown in Figure 4.8. For the period 1500 AD to 1750 AD the transport is generally reduced in austral summer against the 1990 mean whereas a slight strengthening between 1750 AD and 1800 AD can be observed. Thereafter then strength of the barotrophic streamfunction abruptly decreases by approximately 3 Sv but shows an increase by the same amount throughout the 19th and 20th century. In austral winter similar changes as for the summer occur, however, here the shift towards a stronger circulation does not appear as pronouced as for the summer months. These changes however lie well within the range expected from the CTRL1990 simulation. However, it can be seen that decreases in current strength occur in the two source leakage areas of the Agulhas, the Mozambique Current and the Madagascar Current, during the 20th century, pointing towards changes occurring within this current system.

Figure 4.8: Strength of the Agulhas leakage calculated as the average barotropic streamfuction in the area 41.77°S to 39.05°S and 22.70°W to 33.50°W for (a) DJF and (b) JJA. The transient simulations are represented by the colours red, blue, orange, and green; the ensemble mean is plotted in black.

4.1.7   Sea Ice

A further interesting parameter in the high latitude Southern Hemisphere which may be affected by changes in the external forcing is of course sea ice extent. The temporal changes in sea ice area anomalies can be seen in Figure 4.9. The SIA anomalies for the whole of Antarctica (bottom panel) show a shift to positive anomalies during the 16th century. During the following century this trend reverses again whereas during the 18th century a slight shift towards higher sea ice coverage can be seen. Peak sea ice area occurs at 1810 AD. Values remain stable and slightly positive until 1900 AD after which a significant decline of sea ice area occurs. A very similar picture appears for both the annular and the non-annular regime. The only difference can be seen in the 16th century in the non-annular regime. Here, a shift from positive anomalies to a slightly negative state can be observed. However, again, as seen previously for numerous other variables the changes occurring during the pre-industrial period are small and not significant and the changes during the late 19th and the 20th century are presumably related to the increase in greenhouse gases. No changes in the relationship between the regional sea-ice variability can be seen either.

## 4.2   Regional Climate Change

In order to allow comparisons to proxy records climate change in the Southern Hemisphere as simulated by CCSM3 for the past 500 years needs to be evaluated on a regional scale. For this 10 regions were chosen - four for South America, two for South Africa and four for Australia - according to the distribution of temperature and precipitation variability patterns. For each region temperature and precipitation the covariability within the region was maximized to reduce damping of signals. The choice of regions can be seen in Figure 3.23. In the following sections the temperature and precipitations variations shall be explored for each of the three continents. Common variations in each of the simulations indicate that the parameter being analyzed shows a reaction to external forcing. No common variance indicates the period under considerations is dominated by internal variability. The regional temperature and precipitation anomalies can be seen in Figures 4.10 and 4.11.

4.2.1   South America

South America is influenced by a variety of atmospheric and oceanic circulation regimes, each showing its distinct imprint and possibly superimposing and/or masking signals induced by changes in external forcing or changes induced by internal variability. Hence, the temperature and precipitation variations show regionally very different temporal evolutions.

Southern South America (SAM1)

The temperature variations in the transient simulations at the southernmost tip of South America are only small ($< \pm 0.5°$C) up to $\sim$ 1900 AD after which temperatures rise by $< 0.5°$C. A very similar picture can be seen for the seasons DJF and JJA. The simulations show a high degree of internal variability up to 1800 AD after which each simulation shows a shift to colder temperatures which lasts for approximately 30 years which is followed by a slight increase in temperatures which lasts up to 2000 AD and is only interrupted at $\sim$ 1900
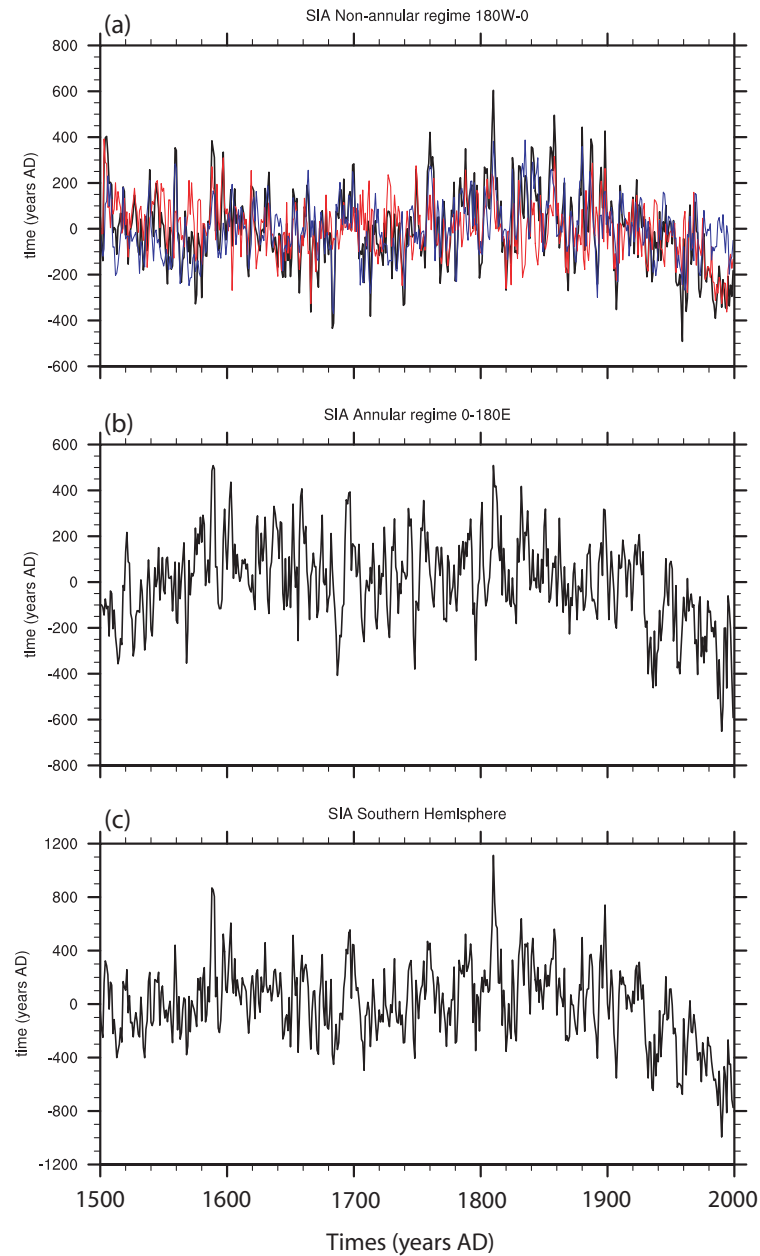
Figure 4.9: Ensemble mean early sea ice area anomalies (1000 km^2) in the transient simulations calculated for (a) the dipole region ($0:180°\text{W}$) where red stands for the Bellingshausen-Weddel Sea, blue for the Amundsen-Ross Sea sector and black for the whole dipole region, (b) the extra-dipole region ($0:180°\text{E}$) and (c) the Southern Hemisphere mean.
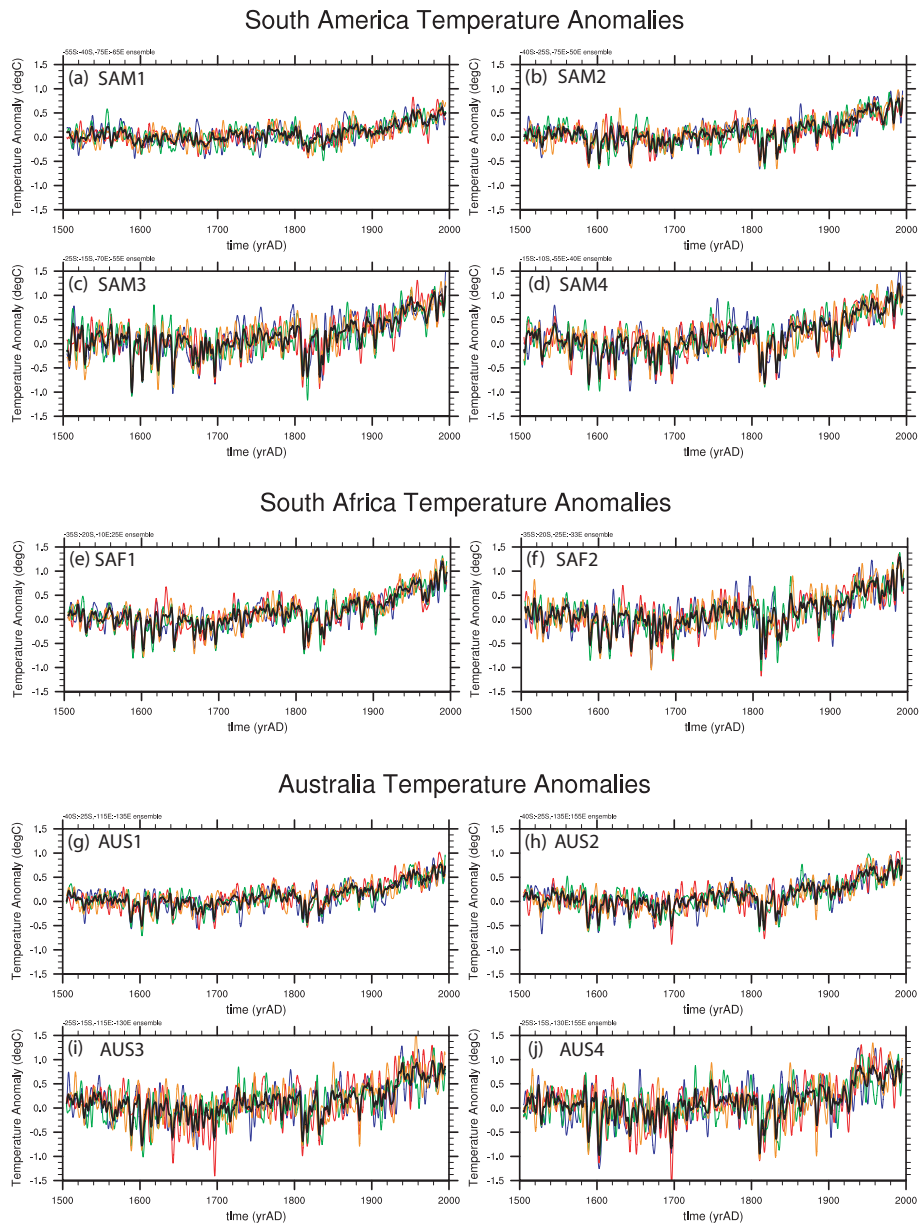
Figure 4.10: Regional temperature anomalies simulated by the transient runs (blue - TR01, red - TR02, green - TR03, orange - TR04) and the ensemble mean (black) for (a) southern South America, (b) central southern South America, (c) western central South America, (d) eastern central South America, (e) western South Africa, (f) eastern South Africa, (g) south-west Australia, (h) south-east Australia , (i) north-west Australia, and (j) north-east Australia. The exact coordinates of the regions are specified above each graph. The monthly anomalies were calculated against the monthly preindustrial means (1500-1850) and a 12-month running mean applied to smooth the records.
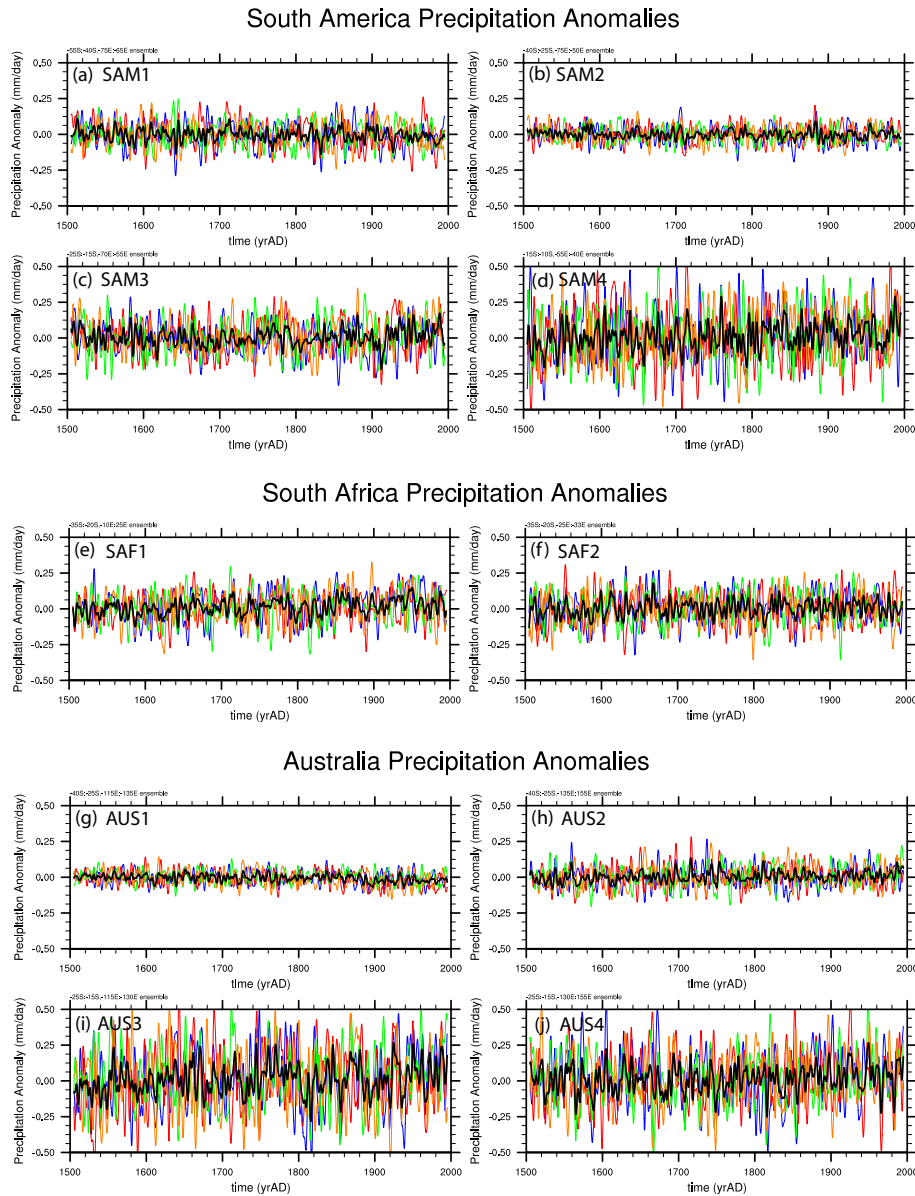
Figure 4.11: Regional precipitation anomalies simulated by the transient runs (blue - TR01, red - TR02, green - TR03, orange - TR04) and the ensemble mean (black) for (a) southern South America, (b) central southern South America, (c) western central South America, (d) eastern central South America, (e) western South Africa, (f) eastern South Africa, (g) south-west Australia, (h) south-east Australia , (i) north-west Australia, and (j) north-east Australia. The exact coordinates of the regions are specified above each graph. The monthly anomalies were calculated against the monthly preindustrial means (1500-1850) and a 12-month running mean applied to smooth the records.

AD where a slight decrease in temperatures occur. The temperature variations for DJF show a lower amplitude than the ones for JJA, and a lower degree of correspondence between the individual simulations.

Year-round precipitation variations appear small and are found to range between ±0.2mm/day. No significant trends are identified for either the records containing information on monthly anomalies nor for the seasonal means. The winter precipitation time series (JJA) shows several oscillations which can be seen in each of the simulations during the 16th century and a strong dip in precipitation in 1580 AD which corresponds to a strong volcanic eruption. During the remainder of the time the simulations show little common variability indicating a degree of internal variability. The summer record shows little agreement between the records though in the 18th, 19th and at the beginning of the 20th century several simulations show decreases in precipitation, each occurring some years after a volcanic event.

Central southern South America (SAM2)

Temperatures during the 16th century appear stable for this region, however, at the end of this century and during the following 60 years a series of shifts to colder temperatures can be observed, each corresponding to a volcanic eruption. These variations appear stronger in the summer months (DJF) than in the winter and have a maximum amplitude of 0.5°C. A slight temperature increase can be seen for all simulations during the 18th century which is interrupted by a drop in temperatures at 1800 AD and several strong oscillations, again, during a period during which several strong volcanic events and a decrease in solar activity occurred. From 1850 AD onwards temperatures rise and only stagnate at 1900 AD when several volcanic events occur. A similar pattern can be seen for DJF and JJA, however, the temperature increase is much less pronounced in the austral winter than in the summer where the temperature increase between 1850 AD and 2000 AD amounts to 1.5°C.

Precipitation variations, as for the region previously discussed, are marked by a high degree of internal variability and no notable shifts occur during the 500 year period neither for the year-round monthly values nor for the seasonal means.

Western central South America (SAM3)

The temperature record for this area of South America appears very similar to the one previously discussed, however, the amplitude of the variation is slightly increased due to its proximity to the tropics. Also the amplitude of temperature increase in the 19th and 20th century is slightly higher. Again the series of volcanic eruptions around 1600 AD and 1800 AD appear to strongly impact the variations in the temperature record. Temperatures during the austral summer appear a lot more stable than during the winter where the variations about twice as strong and show a lower degree of consistency between the records. Precipitation in this region appears to be marked by a high degree of internal variability. Variability is much higher for this region than the previous two and the difference between the summer and winter season is much more pronounced. In the austral summer two shifts to drier conditions can be seen at 1680 AD and 1900 AD, the latter shows up in the winter records too.

Eastern central South America (SAM4)

Temperature variations in this region show strong similarities to Western central America. Again strong temperature dips by up to 1°C can be seen between 1600 AD and 1700 AD, and around 1800 AD. Winter and summer temperature oscillations in this case, however, show closer correspondences. Strong seasonal differences occur for precipitation in this area: In winter precipitation lies close to zero whereas the summer shows much wetter conditions and also very much stronger variations. For the winter no shifts in precipitation regimes can be seen, in the summer strong oscillations occur, however, no clear signal between the different simulation emerges.

4.2.2   South Africa

Western South Africa (SAF1)

The temperature record from Western South Africa shows very similar features to the ones seen for Central South America: stable temperatures in the 16th century, a series of temperature decrease in the order of 1°C throughout the 17th century, stable and slightly increasing temperatures in the 18th century followed by two notable temperature decreases around 1800 AD after which temperatures rise steadily and only show a slight dip around 1950 AD. Precipitation variability is again characterised by a large degree of internal variability. No significant trends can be seen, however it does appear that during the 19th century a shift towards a wetter climate occurred especially during the austral summer months. During this season the variability is also much more pronounced than during the winter. During several volcanic events shifts towards a drier climate occurred, e.g. around 1580 AD, at 1720 AD, and around 1900 AD.

Eastern South Africa (SAF2)

The variations in temperature in the eastern section of South Africa follow the variations in the west very closely. All features noted in the previous section can be found, and even the amplitude of the temperature variations is very alike, the west showing slightly stronger variations as the east. As observed previously the precipitation variations of the respective simulations show only a low degree of covariability between the respective simulations when monthly anomalies are analyzed. Mean precipitation remains fairly constant throughout the 500 years under consideration, only during the 17th century both the variability and also the mean values of precipitation appear slightly increased. This corresponds to a period with many volcanic eruptions. On seasonal scales slightly different pictures appear: For the winter the same precipitation increase occurs, however, the variability appears decreased, whereas for the summer months precipitation does not increase, however, here, in comparison to the previous century the variability increased. During the 20th century as for Western South Africa a tendency towards a wetter climate can be seen during the summer season; in the winter the opposite can be observed.

4.2.3 Australia

South-West Australia (AUS1)

As seen for both southern South America and South Africa, temperature variations in South-West Australia are small in comparison to the areas closer to the equator. During the preindustrial period temperatures remain stable except for small ($\sim 0.5°$C) dips in temperature occurring around 1600 AD, 1700 AD and 1800 AD. From approximately 1850 AD onwards a warming trend can be observed, around 1900 AD a stagnation in the temperature increase occurs; thereafter temperatures rise by $\sim 0.5°$C with a slight reversal in the middle of the 20th century. Neither the DJF nor the JJA records show strong differences to the all-month records. For DJF the temperature increase during the 20th century is more pronounced than for JJA. No marked precipitation anomalies can be seen for the period considered when all months are considered. A similar picture emerges for DJF and JJA. During the austral winter precipitation variability is slightly increased and two periods of anomalously low precipitation can be seen around 1600 AD and 1980 AD, both coinciding with strong volcanic eruptions. Neither show up in the DJF records though.

South-East Australia (AUS2)

The temperature variations in South-East Australia are very similar to the anomalies seen in the south-west. The maximum amplitude is increased by approximately 0.1°C and again negative temperature anomalies can be seen around 1600 AD, 1680-1700 AD and around 1800 AD. Exceptionally warm temperatures occur around 1770 AD coinciding with a peak in the solar forcing. During austral winter the temperature variability is slightly higher than in summer, and the impact of the volcanic eruptions appears increased in comparison to the summer season. Precipitation remains stable throughout the 500 year period for both seasonal and year-round values, notable, however, is a period of exceptionally strong precipitation during the middle of the 16th century.

North-West Australia (AUS3)

The records in the north of Australia show markedly stronger temperature variations and higher amounts of internal variations than the ones of the south. Also due to proximity to the tropic volcanic eruptions show a stronger impact on temperature. For the year-round record temperatures at 1500 AD lie slightly above the preindustrial mean. During the 16th century two distinct dips can be seen, both corresponding to a volcanic event. The strong volcanic eruptions around 1600 AD can clearly be seen in the temperature record. During the 17th century mean temperatures lie $\sim 0.5°$C lower than at 1500 AD, again this was a period with a large number of volcanic events. During the 18th century temperature remained stable and slightly above the preindustrial average. At 1800 AD two distinct temperature drops occurred, again corresponding with several volcanic eruptions. Between $\sim$1920 AD and 1940 AD a marked temperature increase by approximately 0.5°C takes place. Thereafter, temperatures remain stable. Precipitation variability is marked by a high degree of internal variability and fluctuations in precipitation are an order of magnitude stronger than in the southern areas of Australia. Mean precipitation remains fairly constant over the period analysed; towards the 20th century precipitation appears slightly increased. A marked decrease in precipitation can be seen around 1800 AD which is present in each of the simulations,

and appears most pronounced during the austral summer. During this season two positive precipitation anomalies during the 20th century are also notable occurring at 1930 AD and 1950 AD. They are most pronounced during the summer season but can also be seen for the austral winter.

North-East Australia (AUS4)

Temperature variability in North-East Australia shows the same structure as the north west on a year-round basis. The seasonal records also appear very similar, however, record from North-East-Australia shows a stronger and more clear impact of volcanic eruptions. Precipitation shows a low degree of consistency between the respective model runs. Two marked shifts towards drier conditions which can be seen in each of the simulations occur at 1680 AD and appear most pronounced during the summer season. Marked increases in precipitation can be seen at the end of the 19th century in both the DJF and JJA records. No significant changes throughout the 20th century can be seen.

4.3   Stability of teleconnection patterns

This section analyzes the stability of the relationship between the modes of variability examined in the earlier section and the regional temperature and precipitation changes. Two approaches are taken for this. On the one hand the correlations between the regional climate with the timeseries of the modes are compared between the CTRL1990 simulation and the transient simulations, on the other hand a running correlation between both is performed in order to assess the temporal variability of the teleconnection patterns. A comparison between the CTRL1990 and the transient correlation coefficents (Table 4.1 and 3.2, and 4.2 and 3.3 for temperature and precipitation, respectively). It can be seen that for neither temperature nor precipitation large or significant changes in the correlation coefficients occurs between the CTRL1990 and the transient simulations occurs. The 50-year running correlations between the Southern Annular Mode and the regional regional precipitation can be seen in Figure 4.12. Again, no significant changes over time can be seen. This picture repeats itself for the remaining three varibiability modes for both temperture and precipitation which suggests that the teleconnections occurring on a month to month basis appear stable over the period analyzed.

4.4   Underlying Dynamics

When reconstructing modes of internal variability from regional proxy records it is important that the proxy changes actually reflect variations in the mode and not a combination of various modes. A top down approach was taken in the previous section where the stability of the teleconnections was assessed by calculating the amount of variability of regional temperature and precipitation, respectively, which was explained by the respective variability mode. In this section a different approach is taken and the regional temperature and precipitation records are regressed onto the geopotential height field at 850hPa in order to determine the underlying atmospheric dynamics influencing regional climate and to find out whether there is a region solely reflecting changes in one single variability mode.

Table 4.1: Regional surface temperatures in the transient simulations for South America (SAM), South Africa (SAF) and Australia (AUS) correlated with the Southern Annular Mode Index (SAM), South Pacific Dipole Index (SPD), Zonal Wave 3 Index (ZW3), Nino 3.4 Index (Nino3.4) and the Antarctic Circumpolar Current Strength (ACC). For each variable and region, respectively, the highest and lowest correlation coefficient are given. Values significant at the 1% level are labelled with (***), coefficients significant at the 5% level are marked with (**) and those at 10% with (*).

Region	SAM	SPD	ZW3	Nino3.4	ACC	VOL	GHG	SOL
SAM1	0.180 ; 0.204 ***	0.171 ; 0.196 ***	0.360 ; 0.375 ***	-0.033 ; 0.033	0.005 ; 0.023	-0.047 ; -0.021 *	0.475 ; 0.526 ***	-0.089 ; 0.152
SAM2	-0.032 ; -0.025 **	0.160 ; 0.165 ***	0.044 ; 0.071 ***	-0.125 ; -0.076 ***	-0.003 ; -0.000	-0.151 ; -0.134 ***	0.516 ; 0.588 ***	-0.055 ; 0.157
SAM3	-0.114 ; -0.093 ***	-0.05 ; -0.031	-0.094 ; -0.062 ***	0.014 ; 0.053	-0.025 ; -0.006	-0.199 ; -0.146 ***	0.518 ; 0.565 ***	-0.008 ; 0.116
SAM4	-0.110 ; -0.061 ***	-0.157 ; -0.124 ***	0.035 ; 0.045 ***	0.227 ; 0.293 ***	-0.003 ; 0.028	-0.184 ; -0.149 ***	0.580 ; 0.617 ***	0.075 ; 0.125 *
SAF1	-0.052 ; -0.025 **	-0.185 ; -0.159 ***	0.144 ; 0.185 ***	0.094 ; 0.131 ***	0.049 ; 0.060 ***	-0.185 ; -0.157 ***	0.618 ; 0.686 ***	0.079 ; 0.172 *
SAF2	-0.091 ; -0.072 ***	-0.207 ; -0.175 ***	0.099 ; 0.152 ***	0.101 ; 0.133 ***	0.035 ; 0.050 ***	-0.162 ; -0.137 ***	0.525 ; 0.572 ***	0.015 ; 0.102
AUS1	-0.035 ; 0.004	-0.084 ; -0.043 ***	0.158 ; 0.171 ***	0.116 ; 0.142 ***	0.046 ; 0.072 ***	-0.169 ; -0.132 ***	0.478 ; 0.526 ***	-0.089 ; 0.153
AUS2	-0.054 ; -0.002	0.026 ; 0.075 **	0.127 ; 0.160 ***	0.092 ; 0.131 ***	0.050 ; 0.065 ***	-0.163 ; -0.145 ***	0.552 ; 0.606 ***	0.060 ; 0.120
AUS3	-0.109 ; -0.068 ***	-0.059 ; -0.032 **	0.117 ; 0.126 ***	0.131 ; 0.170 ***	0.037 ; 0.053 ***	-0.123 ; -0.093 ***	0.443 ; 0.484 ***	0.038 ; 0.078
AUS4	-0.226 ; -0.181 ***	0.103 ; 0.128 ***	0.023 ; 0.041 *	0.134 ; 0.199 ***	0.026 ; 0.030 **	-0.136 ; -0.105 ***	0.408 ; 0.441 ***	0.020 ; 0.136

Table 4.2: Regional precipitation in the transient simulations for South America (SAM), South Africa (SAF) and Australia (AUS) correlated with the Southern Annular Mode Index (SAM), South Pacific Dipole Index (SPD), Zonal Wave 3 Index (ZW3), Nino 3.4 Index (Nino3.4) and the Antarctic Circumpolar Current Strength (ACC). For each variable and region, respectively, the highest and lowest correlation coefficient are given. Values significant at the 1% level are labelled with (***), coefficients significant at the 5% level are marked with (**) and those at 10% with (*).

Region	SAM	SPD	ZW3	Nino3.4	ACC	VOL	GHG	SOL
SAM1	-0.299 : 0.282 ***	0.165 : 0.168 ***	-0.393; -0.353 ***	-0.203 : 0.021	-0.062 ; -0.0474 ***	-0.046 : 0.001	-0.109 : -0.022	-0.096 : 0.018
SAM2	0.056 : 0.091 ***	-0.214 ; -0.179 ***	0.049 : 0.093 ***	0.105 : 0.127 ***	0.030 ; 0.041 **	0.014 : 0.040	-0.050 : 0.063	-0.030 : 0.031
SAM3	0.031 : 0.061 **	-0.106 : 0.074	-0.013 : 0.014	0.078 : 0.113 ***	0.006 : 0.022	-0.036 : 0.000	0.020 : 0.142	-0.009 : 0.112
SAM4	-0.028 : 0.004	0.058 : 0.086 ***	0.049 : 0.059 ***	-0.076 : -0.050 ***	-0.011 : -0.004	-0.023 : -0.017	0.030 : 0.152	0.008 : 0.089
SAF1	0.241 : 0.297 ***	-0.078 ; -0.061 ***	-0.007 : 0.011	-0.070 : -0.057 ***	0.012 : 0.031	-0.028 : -0.017	0.059 : 0.143	-0.016 : 0.053
SAF2	0.102 : 0.128 ***	0.075 : 0.0844 ***	-0.098 ; -0.065 ***	0.014 : 0.034	-0.025 : -0.019	-0.017 : 0.008	0.001 : 0.065	0.023 : 0.097
AUS1	-0.189 : -0.163 ***	0.210 : 0.236 ***	-0.009 : 0.038	-0.085 : -0.072 ***	-0.006 : 0.010	-0.005 : 0.018	-0.109 : -0.022	-0.096 : 0.018
AUS2	0.150 : 0.181 ***	-0.107 ; -0.056 ***	0.016 : 0.064	-0.193 : -0.182 ***	-0.027 : -0.006	-0.102 : 0.020	-0.001 : 0.115	-0.062 : 0.094
AUS3	0.090 : 0.112 ***	0.010 : 0.012	0.020 : 0.034	-0.110 : -0.072 ***	-0.013 : 0.008	-0.040 ; -0.022 *	-0.014 : 0.089	0.032 : 0.148
AUS4	0.124 : 0.148 ***	0.034 : 0.062 ***	0.042 : 0.061 ***	-0.180 : -0.135 ***	-0.010 : 0.006	-0.049 : 0.032	0.007 : 0.114	-0.066 : 0.056
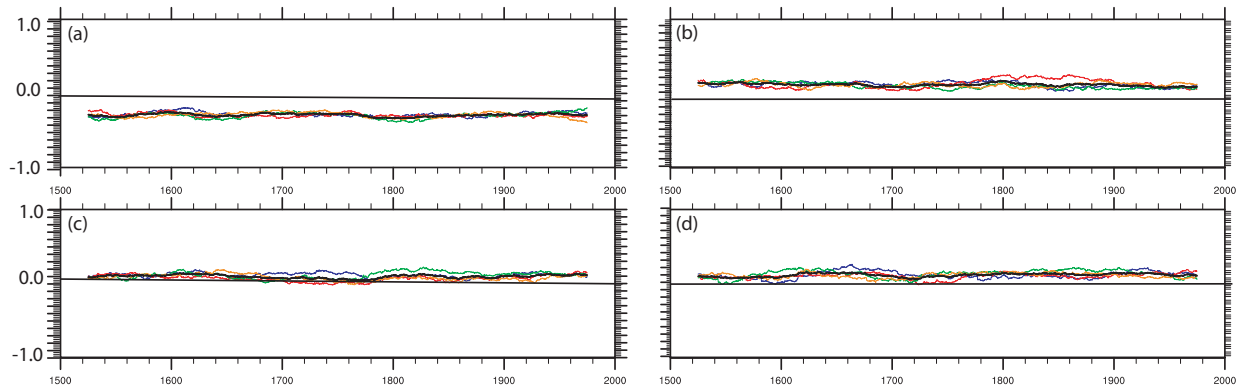
Figure 4.12: The 50 year running correlations between the Southern Annular Mode index calculated for each the TR01 to TR04 simulation with regional precipitation for in South America for region (a) SAM1, (b) SAM2, (c) SAM3 and (d) SAM4.

Figure 4.13 shows the regression of regional temperature with geopotential height at 850hPa for the TR01 run. The patterns emerging for the remaining three runs are very similar, hence, they shall not be shown here. Temperature changes in Patagonia (SAM1) project onto a combination of the Southern Annular Mode, the South Pacific Dipole and the Zonal Wave 3 pattern, thus suggesting that a record of temperature change from this region cannot soley be attributed to changes in a single variability mode. For SAM2 (Chile and Argentina) none of the four variability modes appears clearly. No clear SAM pattern emerges but both the SPD and the ZW3 pattern are weakly identifiable, therefore, again not giving a clear pattern of atmospheric variability. For both SAM3 and SAM4 (western and eastern central South America) no clear pattern of atmospheric variability emerges. Even though the correlation analysis performed in the previous section suggests that ENSO is the dominant mode of variability for SAM4, no sign of the Southern Oscillation can be seen in the Z850hPa field. A similar case appears for SAM3 where correlation analysis suggests that SAM and the ZW3 are the leading modes but the dynamics do not show a clear mix of the two. For western South Africa (SAF1) the impact of both the ZW3 and the SPD can be seen whereas for eastern South Africa shows stronger similarities towards the SAM and the SPD patterns. The dynamics in south west Australia strongly reflect a combination of both the South Pacific Dipole and the Zonal Wave 3; a similar but not as pronounced pattern can be seen for AUS2 (eastern south Australia). Both eastern and western north Australia (AUS3 and AUS4) closely reflect the Southern Annular Mode pattern, even though the correlation analysis suggests that ENSO also strongly influences temperature in this region.

Thus, it can be concluded that the model suggests never only one dynamical effect is responsible for generating temperature variations. Therefore, according to CCSM3 no region would provide a perfect place to reconstruct an atmospheric variability mode because each region represents a combination of influencing factors.

For precipitation the picture appears a little different 4.14. For Patagonia (SAM1) the Southern Annular Mode appears as the dominant mode, however, no sign of the ZW3 pattern can be seen unlike the regional correlations would suggest. For central Chile and Argentine (SAM2) no impact of the Southern Annular Mode can be seen, however, now, both the South Pacific

Dipole and the Zonal Wave 3 pattern influence the regional precipitation dynamics. For region SAM3 the SPD appears as the leading pattern. In eastern central South America (SAM4) no clear variability pattern can be seen. Both in western and eastern South Africa (SAF1 and SAF2) the precipitation variability is clearly dominated by the Southern Annular Mode. For south western Australia (AUS1) the variability appears to be a result of both the Southern Annular Mode and the South Pacifc Dipole. Eastern south Australia is mainly influenced by the Southern Annular Mode, however, a minor influence of the SPD is still detectable. Both north eastern and north western Australia (AUS3 and AUS4) appear to be dominated by the Southern Annular mode again.

4.5   Direct Impact of the Forcing

In this section the direct impact of the forcing greenhouse gas and solar forcing on climate in the Southern Hemisphere is analysed. For this, in a first step the effect of the volcanic forcing was removed. In a first step the impact of the volcanic eruption for the first 120 years for the ensemble mean was estimated by calculating the monthly anomalies for the respective variable against the monthly 3 yearly mean prior to the eruption for year 1, year 2 and year 3 after the volcanic event. This procedure was carried out from 1500 AD to 1620 AD as during this period the volcanic eruptions are temporally well separated and the changes in solar and GHG forcing are small. In the next step the monthly regression coefficients between the respective variable, e.g., surface temperature for each month and for year 1, year 2 and year 3, respectively, and the strength of the volcanic eruption quantified by the change in optical depth. Subsequently, the impact of the volcanic eruptions for the entire timeseries, i.e. 1500 AD to 2000 AD was calculated by multiplying the regression coefficients for years 1
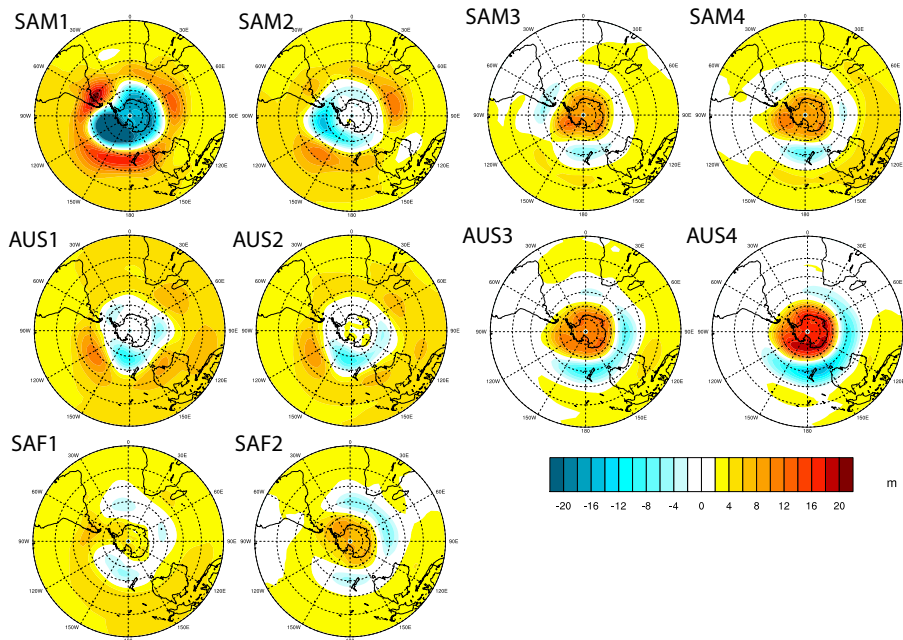
Figure 4.13: Regression of monthly regional surface temperature for South America (SAM1 to SAM4), South Africa (SAF1 and SAF2) and Australia (AUS1 to AUS4) onto geopotential height at the 850hPa level.
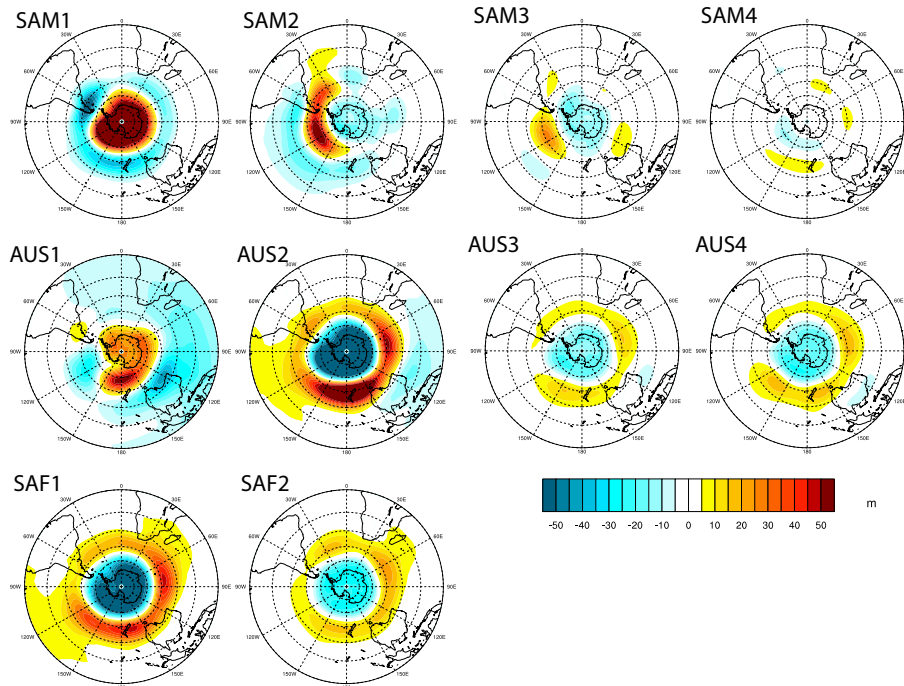
Figure 4.14: Regression of monthly regional precipitation for South America (SAM1 to SAM4), South Africa (SAF1 and SAF2) and Australia (AUS1 to AUS4) onto geopotential height at the 850hPa level.

to 3 with the time series of the changes in optical depth and then subtracting this effect from the original ensemble mean timeseries of the the respective variable. After the impact of the volcanic eruptions was subtracted a regression between the summed forcing (solar variability and GHG changes) and the timeseries of the respective variables was performed and the significance of the regression was tested with a Student's t-test at the 5% level.

The results for the forcing impact on the annual mean climate can be seen in Figures 4.15 and 4.16.

Surface Temperature and Sea Surface Temperatures

The regression between the summed forcing and SST (Figure 4.16(c)) yields a strong and positive response over each the Pacific, the Atlantic and the Indian Ocean sectors. An increase of the forcing by approximately $1 \, \text{W} \, \text{m}^{-2}$ corresponds to a change in SST by between 0.2 and 0.8°C. Over the Southern Ocean no significant positive changes can be seen, in contrary a negative regression coefficient appears over the Ross Sea.

For surface temperature (Figure 4.15(a)) no significant regression coefficients can be seen for the Southern Hemisphere, however, a reduction of the significance level of the t-test shows that over the entire Southern Hemisphere surface temperature and the external forcing are positively related and that an increase in the forcing by $1 \, \text{W} \, \text{m}^{-2}$ would correspond to an increase in surface temperatures by approximately 3°C (not shown). Reducing the analysed time period to the last 150 years, i.e. 1850 AD to 2000 AD, yields a significantly positive regression coefficient which shows that an increase of the external forcing by $1 \text{W} \, \text{m}^{-2}$ would result in a temperature change of approximately 0.5°C all over the Southern Hemisphere

except for the Southern Ocean sector.

Pressure and Geopotential Height

As for surface temperature the regression coefficients for both surface pressure and geopotential height at 850hPa Figure 4.15 (b) and (d) are not significant in the Southern Hemisphere. However, the coefficients when regarded without performing a t-test shows an increase in surface pressure with increasing forcing which is strongest between 30° and 45°S and appears least pronounced over the Southern Ocean and Antarctica. For geopotential height a very similar picture emerges.

Zonal Winds

Figure 4.16(a) shows the changes in zonal wind speed with changes in the external forcing. It can be seen that an increase in the external forcing by $1\,\mathrm{W\,m^{-2}}$ corresponds to a weakening of the Southern Hemisphere westerlies by approximately 0.7 km/h which is a small value compared to the large fluctuations measured in the winds in this region. At the same time a weakening of the equatorial easterly winds can be observed, again the changes lie in the same order of magnitude as for the mid latitude westerly winds.

Meridional Winds

A general strengthening of the northerly component of the meridional winds between 45°S and 60°S with increasing GHG and solar forcing can be seen whereas in the region 30°S a more southerly component is introduced, hence suggesting a weakening of both the Hadley and the Ferrel cells.

Precipitation

With increasing forcing an increase in precipitation over both Antarctica and the Southern Ocean region can be seen. The same picture emerges for the tropics. In the mid latitudes the results appear more spread: Over central Chile and Patagonia, for example, a decrease in precipitation by around 2 mm/day can be seen whereas in the more northerly parts of South America and increase in precipitation with increasing forcing can be seen. Australia in general also sees higher precipitation levels with stronger external forcing whereas the opposite is the case for eastern South Africa.

Sea Ice

The regression between the summed external forcing and sea ice concentration (Figure 4.16(d)) shows that an increase in the external forcing corresponds to a decrease in SIC at the ice edge all around Antarctica except for the Ross Sea where a significant increase in SIC can be seen. An increase in the external forcing by $1\,\mathrm{W\,m^{-2}}$ would correspond to approximately 2.5% decrease in sea ice over the western Antarctic sea ice margins whereas over the Ross Sea an increase of the same magnitude could be observed.
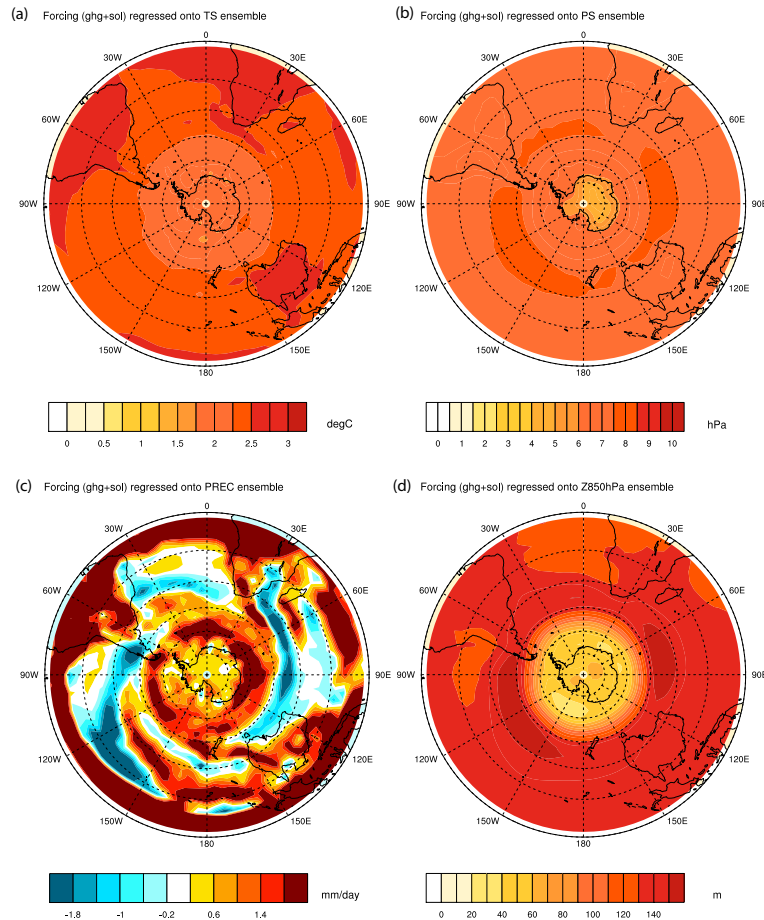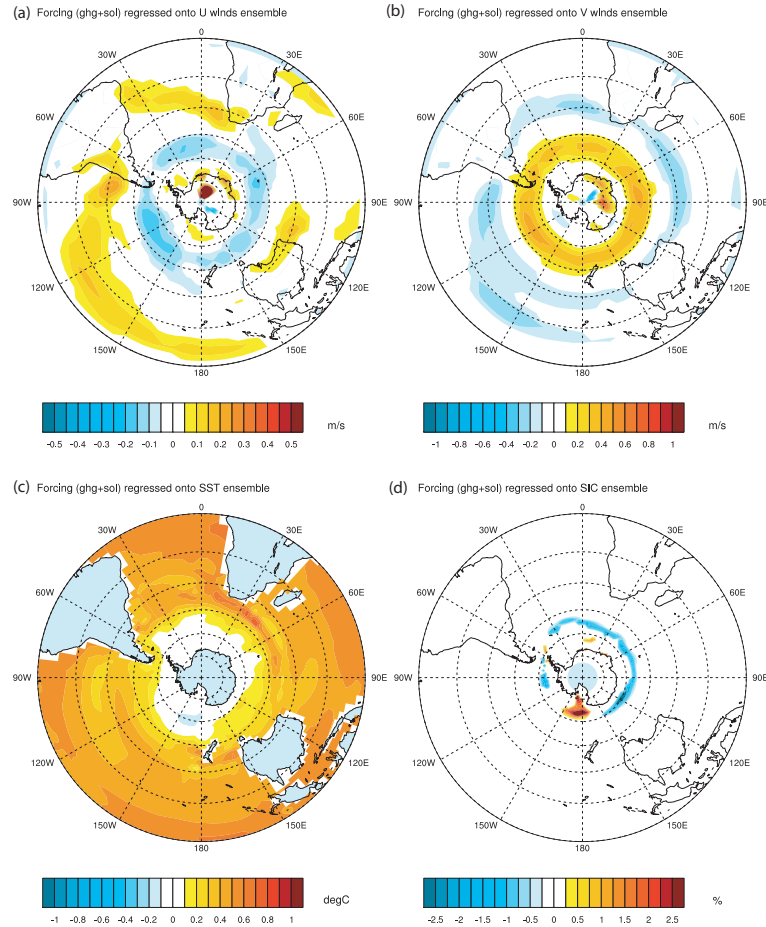
Figure 4.15: Regression of summed forcing (solar variability and GHG changes) onto (a) surface temperature, (b) surface pressure, (c) precipitation and (d) geopotential height at the 850hPa level. For (a), (b) and (d) all regression coefficients are shaded; for (c) only values significant at the 5% level are shaded.

4.6 Discussion

In this section the results of the transient simulations shall be discussed and evaluated. In the first section the changes in the variability modes shall be discussed. In the next section the regional climate change will be evaluated focusing especially on the mid and high latitudes of South America as most proxy records exist for this area. The temperature and precipitation evolutions of Australia and South Africa shall be touched on briefly and be compared to the existing reconstructions for these areas. Then, the discussion shall focus on the stability of the teleconnection patterns found in the transient simulations. Furthermore, the underlying dynamics of the temperature and precipitation variability and the impact of the external forcing shall be briefly discussed.

4.6.1 Changes in the variability modes

The most prominent changes occurring in the variability modes over the past 500 years in the ensemble of simulations can be seen for the Southern Annular Mode whereas the South

Figure 4.16: Regression of summed forcing (solar variability and GHG changes) onto (a) zonal surface winds, (b) meridional surface winds, (c) sea surface temperature and (d) sea ice concentration. Only values significant at the 95% level are shaded.

Pacific Dipole and the Zonal Wave 3 show few notable changes throughout the simulations. The changes in the Southern Annular Mode have also been observed during the last decades [*Thompson and Wallace*, 2000; *Gong and Wang*, 1999; *Marshall*, 2003] and have been attributed to both the ozone losses and the changes in GHG concentrations [*Arblaster and Meehl*, 2006] whereby the changes in the upper atmosphere were mainly driven by ozone and the trends at the surface were a result of the combined GHG and ozone forcing. The simulations used in this study neither included ozone nor aerosols as components of the external forcing. Nevertheless, the model is still able to reproduce the trends in the observations. This has also been found in several previous simulations [*Kushner et al.*, 2001; *Rauthe and Paeth*, 2004] driven solely with GHGs thus suggesting that next to the important trends in ozone GHG also play a role in the recent SAM trends [*Arblaster and Meehl*, 2006; *Cai and Cowan*, 2007; *Roscoe and Haigh*, 2007].

Indeed, the beginning of the increase in the SAM index corresponds closely to the increase in GHGs around 1850 AD. However, according to the regression analysis performed for both the CTRL1990 simulation and the ERA40 reanalysis the changes in surface temperature and

precipitation in the regions selected for analysis are very small and the majority is not significant thus making it hard to actually see impacts of the changes in this variability mode. This is supported by the low correlations between the regional temperature and precipitation timeseries for the CTRL1990 simulations. The highest correlations occurring between SAM and the timeseries are found for Southern South America (SAM1) and North-West Australia (AUS4) for temperature and precipitation but they explain a maximum of 3 and 8%, respectively, of the variability.

The regression analysis (Section 3.2.1) suggests that also a decrease in Antarctic Sea ice sea ice should take place over the Weddell Sea, indeed such a decrease commences around 1900 AD, however, it corresponds with a sea ice decrease around the whole of Antarctica which suggests that this may not be the SAM causing the sea ice decrease in this section but that it may rather be driven by an increase in the radiative forcing causing the ice to melt. Additionally, according to *Arblaster and Meehl* [2006] an increase in the strength of the Southern Hemisphere westerlies which corresponds to an increase in the SAM leads to a cooling over all of Antarctica except for the Weddell Sea and the Antarctic Peninsula. This should result in the currently observed sea ice increase around Antarctica [*Cavalieri and Parkinson*, 2008].

During the last years, several reconstructions of SAM variability have been published [*Jones and Widmann*, 2003; *Jones and Widmann*, 2004; *Jones et al.*, 2009] based on several different methods. The Jones and Widmann [*Jones and Widmann*, 2003; *Jones and Widmann*, 2004] method is based on principle component analysis whereas the Fogt reconstruction [*Jones et al.*, 2009] is derived from the station-based Marshall index [*Marshall*, 2003]. The reconstructions presented in *Jones et al.* [2009] show a stable SAM index between 1870 AD and 1960 AD, around 1960 AD a peak in the SAM index occurred which was followed by a sharp drop which is especially prominent in the DJF reconstructions. Thereafter a significant trend in the index is visible. Neither the monthly SAM index nor the seasonal indices calculated from the transient simulations show this behavior. Furthermore, as noted earlier the increase in the SAM index in the model began earlier than expected from the reconstructions. *Fogt et al.* [2009] assess the performance of the IPCC AR4 models in reproducing the observed and reconstructed SAM trends. They find that differences appear between models which include ozone forcing and those that do not - those that implement ozone changes simulate a somewhat stronger change from 1980 AD onwards when ozone levels began to decrease. The models are able to resolve the observed seasonal differences, i.e. the strong trend during austral summer (DJF) and the lack in the trend in winter (JJA). The coarse resolution version of CCSM3 used in this study is not able to pick up on these differences and significant trends appear for both seasons. Also, a feature which the models lack is the representation of multiyear peaks in the SAM index which are found in the reconstructions at 1960 AD and 1930 AD thus suggesting that they are not able to capture the full dynamics of this variability mode. The authors note that the reason for this may be lacking 'communication' with the tropics and insufficient coupling of troposphere and stratosphere.

No significant trends in the Zonal Wave 3 and the South Pacific dipole can be seen over the course of the transient simulations. On the one hand this may be the result of the strong baroclinity of CCSM3 [*Yeager et al.*, 2006] preventing tropical and extratropical anomalies from propagating to the polar latitudes and masking meridional variations. A further possibility

may also be given by the very regular ENSO in the model which also shows no significant shifts in variability strength and frequency throughout the course of the 500 model years. As ENSO also influences the South Pacific to Atlantic wave train [*Kiladis and Mo*, 1998] it is thus not surprising that no changes in this variability mode occur. No trends in the ZW3 show up as a result of the external forcing. This result is consistent with *Raphael and Holland* [2006] who found that the slightly positive trend in the NCEP/NCAR reanalysis data was presumably a result of internal variability as it could not be verified by any of the different models they used. Thus, these two modes should also not lead to major changes in Southern Hemisphere climate over the past 500 model years even though the ZW3 appears to have a much greater impact on climate in Southern South America (in CTRL1990 it explains 15% of temperature and precipitation variability).

No significant changes in ENSO variability occur during the five centuries analyzed however a shift towards higher variability does appear during the late 17th and early 18th century. This is contrary to the findings of *McGregor et al.* [2010] who compiled a unified proxy for ENSO and PDO variability ranging back to 1650 AD. Their work indicates that ENSO variability during this period was significantly reduced whereas the 20th century represents a period of high variance. They find that this signal is robust, does not originate from dating uncertainties and can also be found in various climate archives independent of the proxies used for the reconstructions. Further they cannot exclude that periods with low solar activity correspond with periods of low ENSO variability which indicates that variations in the external forcing may well impact on ENSO. The simulations in this study do not show this relationship. Also the wavelet analysis conducted in the previous section shows that no significant changes in ENSO frequency occurred. A reconstruction by *Cobb et al.* [2003] indicates that ENSO variability during the early and mid 17th century was significantly increased and that a shift to higher frequencies occurred. This feature again does not correspond to the model findings. Similarly, this does also not support the hypothesis by *Mann et al.* [2005] that higher ENSO variability corresponds to periods of low solar activity. These findings indicate that ENSO variability in the model may be somewhat too robust against the external forcing which then of course would also have implications for climate variability at the mid and high latitudes which are either directly impacted by ENSO or show indirect impacts through for example the South Pacific dipole pattern.

The stability of the teleconnection patterns on a month-to-month basis is an important result of this study especially in the light of reconstructing the internal variability of the climate system. The correlation patterns for each of the analzed modes appear very stable over time and no significant changes in the correlations between the respective modes of variability. Proxy archives and observational data, however, suggest that the link is not as straightforeward and that changes over time may well occur, e.g., through the modification of one mode through another. For example, *Gregory and Noone* [2008] showed that the ENSO imprint on δ^{18}O in Antarctic ice cores was modified according to the state SAM was in. A further study by *Richard et al.* [2001] indicates that the relationship between ENSO and precipitation patterns has shown pronounced shift during the last 50 years over Africa due to changes in convection over the Indian Ocean. *Marshall* [2007] point out a reversal in the SAM - temperature relationship over East Antarctica which occurred during the 1980s due to a change in the long-wave patters over Antarctica. In this study, 50 year windows were chosen for the correlation analysis whereas most of the analysis carried out with data from the last

century uses data where global coverage is not obtained until the begin of the satellite era thus giving merely 30 years of data for the high latitude Southern Hemisphere. Also, the linkage between diffent proxy archives is hampered by dating uncertainties, reconstruction methods and regional changes as *Wilson et al.* [2010] demostrate. They show that a number of ENSO reconstructions show a similar spectral behaviour that, however, the spacial and temporal constistency is not given. Again this points to the varying influence of the main modes of internal variability on remote areas. For the Northern Hemisphere *Raible et al.* [2006] find that proxies show notable shifts in teleconnectivity especially during the Maunder Minimum which partly explain changes in temperature and precipitation. In contrast, their model (CCSM2.0 which is the precursor model of the one used for this study) showed much more stable teleconnections for both a perpetual CTRL1990 and a future projection. Therefore, even though the model used for this study points towards stable teleconnection a number of proxy and observational records do not; hence, the results of this study need to be treated with care and require further investigation.

4.6.2 Changes in the ocean system

Both the changes in the Antarctic Circumpolar Current and the Agulhas leakage were analysed for the transient simulations. In comparison to the CTRL1990 simulation no significant changes occur. However, the comparison between different time periods of the simulations e.g. 1700 AD versus 1800 AD does suggest that changes in the strength of both current systems occurred. Also, the variability of the both of the currents appears higher for a perpetual external forcing than for a time varying external forcing. As mentioned in the discussion in Chapter 3 in the low resolution version of CCSM3 the ACC appears less sensitive to a change in external forcing which is at least partly related to a biased position and reduced sensitivity of the Southern Hemisphere westerly winds [*Otto-Bliesner et al.*, 2006]. This might provide an explanation for the non-significance of the variations in the ACC. As seen from the analysis of the changes in the Southern Annular Mode indeed a shift of the position of the Southern Hemisphere westerly winds occurs, however it is weak and only significant during the last decades of the 20th century. A variety of authors note that an increasing external forcing would result in an increase of the Southern Hemisphere westerlies and thus to an increase in the strength of the ACC [*Fyfe and Saenko*, 2006], however an analysis of Argo floats and historical oceanographic data *Böning et al.* [2008] to date shows that to date both the density profiles of the ACC and the meridional overturning in the Southern Ocean have shown no significant changes in response to the changes in wind stress.

Biastoch et al. [2009] found a significant trend to a stronger flow of the Agulhas current in high resolution simulations of the Agulhas leakage driven with surface forcing fields for the time period 1958 to 2004 AD. They note that this is the impact of a poleward shift in the westerly winds during the past three decades. The authors also stress that an increased leakage would correspond to a decreased Agulhas current and they indeed find a reduction in the transport through both the Mozambique Channel and a decreased recirculation in the Southwest Indian Ocean subgyre. Indeed, these trends can also be observed in the model. Both the Mozambique Current and the Madagascar Current which are the main contributors to the Agulhas current show a decrease of several Sverdrup, hence suggesting that indeed

changes in these current systems are occurring which affect the Agulhas leakage and pointing towards the model being able to capture the dynamics of the interplay of the different current systems. These changes may show far reaching impacts, for example, on the Atlantic overturning circulation by influencing the salt budget. Throughout the course of the simulations performed by *Böning et al.* [2008] the salt export via the Agulhas leakage increased by 25% and the salinity of the North Brazil Current through which the largest portion of the northward volume transport takes place shows an increasing trend. This result is confirmed with historical oceanographic data. In an earlier paper *Böning et al.* [2008] find a further process by which changes in the Agulhas leakage may affect the meridional overturning in the North Atlantic (AMOC). Low-frequency undulations in the thermocline depth in the Agulhas regime propagate through the Atlantic and dynamically influence the AMOC. Due to the low resolution it is, however, not possible to study such processes in CCSM3.

4.6.3   Regional changes

To date not many temperature and precipitation reconstructions from the mid and high latitude Southern Hemisphere exist. Two recently published studies [*Neukom et al.*, 2010; *Neukom et al.*, 2010] take a multi-proxy approach for reconstructing South-American temperature and precipitation fields and range as far back as 900 AD and 1500 AD, respectively. These reconstructions provide intriguing possibilities for comparison with the model results of this study. Their reconstruction area for both variables encompasses the land masses of Southern South America south of 20°S, thus corresponding to a compilation of the regions SAM1, SAM2 and the southernmost parts of SAM3 and SAM4.

Their temperature reconstructions for austral summer show that the period 1500 AD to 1700 AD was marked by cold conditions which was followed by a century of approximately 1°C warmer temperatures. Around 1825 AD an abrupt shift to colder conditions occurred after which temperatures began to rise steadily. The reconstruction for the winter months does not range as far back as the summer reconstruction due to differences in the proxy quality for the seasons. The reconstructions for the two seasons appear somewhat different: the winter record indicates cool temperatures between 1700 AD and 1750 AD which are followed by a period during which the values approximate the 1901 AD to 1995 mean. The 1825 AD cooling which is prominent in the summer record appears weaker for the winter season and a shift back to the previous levels occurs. Around 1870 AD a second stronger temperature drop occurs which cannot be seen for the summer months at this magnitude. Thereafter, the records show a temperature peak at 1950 AD which is followed by a slight cooling after which temperatures begin to increase. This study thus suggests that major variations in Southern South America temperatures occurred during the past 500 years and that additionally the seasonal timeseries of temperature differed significantly.

These findings are supported by several other temperature reconstructions from Southern South America. For example a summer temperature from Laguna Aculeo in Central Chile [*von Gunten et al.*, 2009] shows that temperatures were reduced by approximately 1°C in comparison to today. Clearly visible is also the temperature drop around 1825 AD and a second one at 1900 AD. *Villalba* [1994] presents similar results. He finds that a long cold and moist period existed from 1270 AD to 1660 AD in northern Patagonia which is contemporaneous with the Little Ice Age (LIA) in the Northern Hemisphere. In central Chile

the results indicate drought conditions during the periods 1570 AD to 1650 AD and 1770 AD to 1820 AD. Both periods were found to correspond with glacial advances in Northern Patagonia [*Villalba*, 1994; *Araneda et al.*, 2007].

The regional timeseries for the model ensemble simulations do not show the prominent changes that the proxy records exhibit. Also, the differences between the summer and the winter season appear much less pronounced. The records show very little variability on both seasonal and year-round timescales and appear to react rather to the increase in GHGs and the decreased radiative forcing during volcanic events which stands in contrast to the reconstructions.

The precipitation reconstructions [*Neukom et al.*, 2010] again present a distinctly different picture for the winter and summer seasons, however, in comparison to the temperature fluctuations precipitation values show much more consistent patterns. For the austral summer record precipitation values during the 16th century lie close to the 1905 AD to 1995 AD mean. Thereafter, the values appear somewhat reduced up to 1800 AD where peak precipitation levels are reached but followed by a short prominent dip around 1825 AD. From 1850 AD onwards, values approach the 1905 AD to 1995 AD mean again and towards the end of the 20th century even show a slight increase. The winter records shows very much the opposite picture of the summer record - during periods of anomalously increased precipitation during the summer the winter records show decreased precipitation levels and vice versa. Towards the end of the 20th centuries a slight decrease in precipitation levels can be seen. The precipitation reconstructions by *Tonello et al.* [2009] show a drop in annual precipitation in southern Patagonia in the late 18th and early 19th century which is followed by a strong increase during the 20th century and a reversal towards the end of the century. These records again indicate that precipitation in southern South America was highly variable during the past centuries. As for temperatures the simulations do not pick up the variations prior to about 1900 AD, however, thereafter, the trends seen in the model also appear for especially the SAM2 region which also shows a shift to more positive precipitation values during the summer months and very slight decrease in precipitation for the winter months. The slight increase could be related to the positive trend in Southern Annular Mode and the associated shift in the Southern Hemisphere westerlies owing to the significant correlations appearing for this area.

The proxy temperature records of South Africa closely resemble those of South America [*Holmgren et al.*, 1999; *Tyson et al.*, 2000]. Reconstructions from this area show that temperatures were low during the period 1300 AD to 1800 AD with the lowest temperatures occurring around 1700 AD [*Holmgren et al.*, 1999] and that temperatures were reduced by approximately 1°C during this period [*Tyson et al.*, 2000]. Unpublished borehole data from this area [*Pollack et al.*, 2006] indicates that the warming during the 19th and 20th century was somewhat stronger in South Africa than that measured for Australia. Again these are results which would agree with our model findings.

Riverflow reconstructions for the Great Barrier Reef and Queensland (north-east Australia; corresponding to AUS4) indicate that the timeperiod 1730 AD to 1820 AD was generally wetter whereas condition during the period 1820 AD to 1870 AD were generally much drier [*Lough*, 2007]. Lake levels measured for three lakes in Victoria (south-east Australia; corresponding to AUS2) show a decrease beginning in 1814 AD when the first measurements were

carried out [*Jones et al.*, 2001]. Neither of the two results can be verified by the simulated changes in precipitation. The model shows little to no change in precipitation over the past five century in contrary to observations. Borehole temperatures are not able to reflect short term fluctuations but provide an idea about long term trends and shifts in temperatures. Reconstructions for Australia suggest that a warming trend began around 1800 AD and that temperatures increased by approximately 0.5°C up to 2000 AD with most of the warming occurring during the latter two centuries [*Pollack et al.*, 2006]. These values would fit reasonably well with the estimates obtained from the model ensemble for the latter two centuries.

The modelled temperature changes in South America, South Africa and Australia appear to relate mainly to a combination of the GHG and volcanic forcing which is supported by the significant and high (in the case of GHGs) correlation coefficients showing that GHG variations explain between 16% for north-east Australia and 47% of the temperature variations for eastern South Africa. Unlike these findings, precipitation levels do not appear to be effected by changes in external forcing but also do also not show a clear linkage to any of the variability modes. This stands in contrast to the clear linkages between the regional precipitation and modes such as SAM or ENSO [*Garreaud et al.*, 2009] appearing in observations. One of the problems may be the resolution of the model reducing the impact of the variability modes and increasing the impact of the external forcing in the case of temperature variability. The low resolution also reduces the complexity of the topography which is an important factor in representing regional climatic variations accurately. A further effect damping the regional climate variations may be the lacking changes in oceanic variability. The areas that were analysed in this study are all surrounded to a significant degree by large water masses and thus influenced by variability in oceanic parameters such as currents or temperatures.

4.6.4   Impact of the forcing

It can be seen that changes in the forcing in the GHG and solar forcing lead to significant changes in Southern Hemisphere climate. As expected from basic physical principles an increase in the radiative forcing results in an increase in temperature. These are least pronounced in the Southern Ocean section due to the large heat capacity of this huge water mass. Also, as it is an area of widespread upwelling temperature changes are masked by the input of colder deep waters returning to the surface here. Due to the weak changes in external forcing during the first 350 years of the simulations (less than $0.5 \, \mathrm{W \, m^{-2}}$) internal variability presumably masks the impacts of the changes in external forcing. Related to this a significant decrease in sea ice can be seen due to the thermal forcing. This stands in contrast to the observations [*Cavalieri and Parkinson*, 2008] of a sea ice increase in Antarctica during the past 30 years. However, it is presumed that this increase is related to an increase and shift in the Southern Hemisphere westerlies. The increase in wind speeds around 60°S causes a northward Ekman drift and hence a flow diverging from the margins of the Antarctic continent and driving sea ice further northward [*Hall and Visbeck*, 2002]. If however, the position of the westerlies in the model is not correct as discussed in the previous chapter, this dynamical effect may not be realistically simulated and the thermal forcing of GHG changes becomes the dominating influence.

The changes in the atmospheric dynamics show a less clear picture than the temperature changes. For the last 150 years the results suggest GHG and solar forcing increases lead to

a pressure increase over the mid latitudes occurs whereas a very slight deepening of pressure over Antarctica takes place. This pattern corresponds to the increased SAM index that can be seen for both the transient simulations and observational data [*Marshall*, 2003]. One effect expected due to these changes in pressure would be an increase in mid latitude westerly winds. This however, cannot be observed. The changes in the westerly winds are very small in comparison to the year-round and interannual fluctuations and thus suggest that the Southern Hemisphere westerlies in the model appear fairly robust against the forcing. This corresponds to results for the Southern Annular Mode where it was noted that a strengthening and southward shift in the westerly winds can only be observed during the last years of the transient simulations. One problem in this context is presumably the low resolution of the model. The observed recent poleward shifts of the westerlies noted by e.g., *Biastoch et al.* [2009] takes place on sub-grid scales; thus, even if the model was able to correctly represent the dynamics behind the shift it would not be able to actually show the shift. Also, it is believed that ozone is one major contributor to the strengthening of the winds; the model used for this study, however, does not incorporate ozone changes. The pattern for the meridional winds corresponds well to the changes for geopotential height. An increase in the northward component over the Southern Ocean can be seen whereas a slight southward increase of the winds can be seen over the mid latitudes. This pattern corresponds to the mechanism noted by [*Hall and Visbeck*, 2002] however it comes without the increase in the westerlies which simulated by a large range of models [*Fyfe and Saenko*, 2006].

Chapter 5

Conclusion and Outlook

In this study several different approaches were taken in order to analyze climate change in the Southern Hemisphere mid and high latitudes over the past 500 years as an ensemble of simulations conducted with CCSM3 with time varying external.

Firstly, changes in the main modes of variability were evaluated by first calculating in the patterns in the CTRL1990 simulation and then projecting them onto the transient simulations to obtain a measure of the state of the mode. No changes were found for the South Pacific Dipole, the Zonal Wave 3 and ENSO variability. All of the three showed no shifts under the changing external forcing and the patterns remained robust throughout the simulations, thus suggesting stability under a certain range of external forcing. This, however, does not exclude that changes in the future with even higher GHG levels may occur.

However, it could be seen that a shift in the Southern Annular Mode occurred during the last century of the simulations. It is related to an increase in pressure over the mid latitudes increasing the gradient between the mid and high latitudes. An increase in the strength of the Southern Hemisphere westerlies and a poleward shift of the wind system does not occur until the end of the 20th century; therefore, providing one explanation why oceanic systems such as the Antarctic Circumpolar Current or the Agulhas leakage show little change over the course of the simulations. The changes in the Southern Annular Mode correspond to a variety of recent observation but also model simulations. It is important to note that the simulations conducted for this study did not use ozone forcing; thus, one important result is that the recently observed changes in SAM may at least in part be driven by GHG changes.

A further important result is the stability of the teleconnection patterns with regional climate in the mid latitude Southern Hemisphere over time. No significant changes in the correlations between regional temperature and precipitation and the respective modes of atmospheric variability could be seen. The stability of the teleconnections provides helpful conclusions for the proxy community as it suggests the spatial patterns of the modes remained the same over time, and thus could provide the opportunity for reliably reconstructing the atmospheric variability modes over time, as previously done for e.g. ENSO or SAM. However, as discussed in the previous section, these results need to be treated with care, as a stronger external forcing may well change the teleconnection patterns, and they may be biased by errors in the model.

Regional temperature changes are dominated by the changes in the external forcing, i.e. the increase in the Greenhouse gasses during the last century and volcanic eruptions throughout the course of the simulations. No significant trends or shifts in precipitation are found for either of the analyzed regions. The underlying dynamics of the regional temperature variations rarely point to only one single atmospheric mode; mostly, at least two modes are identified in the geopotential height field at 850 hPa. For precipitation, however, the influence of the Southern Annular Mode on the variability can clearly be seen which is associated with the strength and position of the mid latitude storm tracks influencing the amounts of regional precipitation.

However, as noted, previously especially temperature rarely reflects only one mode of variability, thus making it hard to find distinct locations which solely reflect the signal of only one mode. Thus, one important conclusion of this study is that much care needs to be taken when reconstructing Southern Hemisphere variability modes from precipitation or temperature proxies, as the inferred signals may be an overlap of several different dynamical modes.

The impact of the combined external forcing, i.e. solar and greenhouse gas forcing, after the impact of the volcanic eruptions has been removed shows that an increase in the external forcing results in an increase of both surface and sea surface temperature which is most pronounced over the mid and tropical latitudes whereas the weakest changes can be seen over the Southern Ocean. Consistent with the temperature increase in the Southern Hemisphere a decrease in sea ice concentration, especially at the margins, can be seen for most of Antarctica. No large changes in the zonal winds can be seen, however, for the meridional winds a strengthening of the northerly component close to Antarctica can be observed. Furthermore, geopotential height increases with a shift in the external forcing to higher values which at least partly explains the increase in the SAM index over this period. The changes in precipitation are very regional, however, in general, an increase in precipitation over the mid latitude continents values occurs with increasing forcing.

After performing this study with just one model it would be interesting to carry out the same analyses on a whole set of models in order to reduce the errors and uncertainties of the individual models. For example, the set of AR4 models used for the IPCC AR4 would provide a good basis for performing a millennium scale set of ensemble simulations. Also, this study used the coarse resolution version of CCSM3; an increase in resolution to e.g. the T85 setup could lead to an improvement of the results. In addition, it would be intriguing to perform simulations which reached further in the past to see how Southern Hemisphere atmospheric variability change, e.g. throughout the Holocene, and whether teleconnection patterns remain stable under stronger external forcing and in a different model set. Of course, a further related step would be to assess the evolution of variability of the modes with increasing external forcing applying different scenarios.

Then, further emphasis should be laid on connecting the proxy records and extending the network of reconstructions for, e.g., South Africa and Australia where up to date only few high resolution records of climate over the past millennium exist. Once more records exist it would be interesting to perform a set of simulations with data assimilation where the reconstructions serve as described by *Goosse et al.* [2006] in order to increase the currently, in comparison to the Northern Hemisphere, limited knowledge on climate variability in the mid and high latitudes of the Southern Hemisphere.

Chapter 6

Acknowledgements

I would very much like to thank my supervisor Christoph C. Raible for all his help and and the very fruitful input he gave me for this study. A thank you also goes to Thomas Stocker for the comments on this work. Also I would like to thank my office colleagues (the 'Partybüro') for making the time so enjoyable and especially Claudia for distracting me with various climbing trips to Fribourg. Also, I very much appreciated my parent's support and would like to especially thank Toby for all the loving encouragement he gave me during the last months of completing this work.

List of Tables

List of Figures

Bibliography

Ackerley, D., and J. A. Renwick, The Southern Hemisphere semiannual oscillation and circulation variability during the Mid-Holocene, *Climate of the Past, 6*(4), 415–430, 2010.

Ammann, C. M., and P. Naveau, Statistical analysis of tropical explosive volcanism occurrences over the last 6 centuries, *Geophysical Research Letters, 30*(5), 1210, 2003.

Araneda, A., F. Torrejn, M. Aguayo, L. Torres, F. Cruces, M. Cisternas, and R. Urrutia, Historical records of San Rafael glacier advances (North Patagonian Icefield): another clue to 'Little Ice Age' timing in southern Chile?, *The Holocene, 17*(7), 987–998, 2007.

Arblaster, J. M., and G. A. Meehl, Contributions of External Forcings to Southern Annular Mode Trends, *Journal of Climate, 19*(12), 2896–2905, 2006.

Biastoch, A., C. W. Boning, and J. R. E. Lutjeharms, Agulhas leakage dynamics affects decadal variability in Atlantic overturning circulation, *Nature, 456*(7221), 489–492, 2008.

Biastoch, A., C. W. Boning, F. U. Schwarzkopf, and J. R. E. Lutjeharms, Increase in Agulhas leakage due to poleward shift of Southern Hemisphere westerlies, *Nature, 462*(7272), 495–498, 2009.

Blunier, T., J. Chappellaz, J. Schwander, B. Stauffer, and D. Raynaud, Variations in atmospheric methane concentration during the Holocene, *Nature, 374*(6517), 46–49, 1995.

Böning, C., A. Dispert, M. Visbeck, S. Rintoul, and F. Schwarzkopf, The response of the Antarctic Circumpolar Current to recent climate change, *Nature Geoscience, 1*, 864–869, 2008.

Bromwich, D. H., and R. L. Fogt, Strong Trends in the Skill of the ERA-40 and NCEP-NCAR Reanalyses in the High and Midlatitudes of the Southern Hemisphere, 1958-2001, *Journal of Climate, 17*(23), 4603–4619, 2004.

Cai, W., and T. Cowan, Impacts of increasing anthropogenic aerosols on the atmospheric circulation trends of the Southern Hemisphere: An air-sea positive feedback, *Geophysical Research Letters, 34*(23), L23709, 2007.

Cavalieri, D. J., and C. L. Parkinson, Antarctic sea ice variability and trends, 1979-2006, *Journal of Geophysical Research, 113*, C07004, 2008.

Cobb, K. M., C. D. Charles, H. Cheng, and R. L. Edwards, El Nino/Southern Oscillation and tropical Pacific climate during the last millennium, *Nature, 424*(6946), 271–276, 2003.

Collins, W. D., C. M. Bitz, M. L. Blackmon, G. B. Bonan, C. S. Bretherton, J. A. Carton, P. Chang, S. C. Doney, J. J. Hack, T. B. Henderson, J. T. Kiehl, W. G. Large, D. S. McKenna, B. D. Santer, and R. D. Smith, The Community Climate System Model Version 3 (CCSM3), *Journal of Climate, 19*(11), 2122–2143, 2006.

Crowley, T. J., Causes of Climate Change Over the Past 1000 Years, *Science, 289*(5477), 270–277, 2000.

Deser, C., A. Capotondi, R. Saravanan, and A. Phillips, Tropical Pacific and Atlantic Climate Variability in CCSM3, *Journal of Climate, 19*, 2451–+, 2006.

Diaz, H., and V. Markgraf, *El Niño: Historical and paleoclimatic aspects of the Southern Oscillation*, Cambridge: Cambridge University Press, 1992.

Dlugokencky, E. J., S. Houweling, L. Bruhwiler, K. A. Masarie, P. M. Lang, J. B. Miller, and P. P. Tans, Atmospheric methane levels off: Temporary pause or a new steady-state?, *Geophysical Research Letters, 30*(19), 1992–, 2003.

Drost, F., J. Renwick, B. Bhaskaran, H. Oliver, and J. McGregor, Variability of the atmospheric circulation in the Southern Hemisphere during the last glacial maximum, *Journal of Geophysical Research, 112*(D10), D10101–, 2007.

Etheridge, D. M., L. P. Steele, R. L. Langenfelds, R. J. Francey, J.-M. Barnola, and V. I. Morgan, Natural and anthropogenic changes in atmospheric CO2 over the last 1000 years from air in Antarctic ice and firn, *Journal of Geophysical Research, 101*(D2), 4115–4128, 1996.

Flueckiger, J., A. Daellenbach, T. Blunier, B. Stauffer, T. F. Stocker, D. Raynaud, and J.-M. Barnola, Variations in Atmospheric N2O Concentration During Abrupt Climatic Changes, *Science, 285*(5425), 227–230, 1999.

Flueckiger, J., E. Monnin, B. Stauffer, J. Schwander, T. F. Stocker, J. Chappellaz, D. Raynaud, and J.-M. Barnola, High-resolution Holocene N2O ice core record and its relationship with CH4 and CO2, *Global Biogeochemical Cycles, 16*(1), 1010–, 2002.

Fogt, R. L., J. Perlwitz, A. J. Monaghan, D. H. Bromwich, J. M. Jones, and G. J. Marshall, Historical SAM Variability. Part II: Twentieth-Century Variability and Trends from Reconstructions, Observations, and the IPCC AR4 Models, *Journal of Climate, 22*(20), 5346–5365, 2009.

Fröhlich, C., and J. Lean, Solar radiative output and its variability: evidence and mechanisms, *Astronomy and Astrophysics Review, 12*(4), 273–320, 2004.

Fyfe, J. C., and O. A. Saenko, Simulated changes in the extratropical Southern Hemisphere winds and currents, *Geophysical Research Letters, 33*, L06701, 2006.

Garreaud, R., and D. S. Battisti, Interannual (ENSO) and interdecadal (ENSO-like) Variability in the Southern Hemisphere Tropospheric Circulation, *Journal of Climate, 12*(7), 2113–2123, 1999.

Garreaud, R. D., M. Vuille, R. Compagnucci, and J. Marengo, Present-day South American climate, *Palaeogeography, Palaeoclimatology, Palaeoecology, 281*(3-4), 180 – 195, 2009.

Gent, P. R., W. G. Large, and F. O. Bryan, What sets the mean transport through Drake Passage?, *Journal of Geophysical Research, 106* (C2), 2693–2712, 2001.

Gille, S. T., Warming of the Southern Ocean since the 1950s, *Science, 295* (5558), 1275–1277, 2002.

Gillett, N. P.; Kell, T. D. J. P. D., Regional climate impacts of the Southern Annular Mode, *Geophysical Research Letters, 33*, L23704, 2006.

Gong, D., and S. Wang, Definition of Antarctic Oscillation Index, *Geophysical Research Letters, 26*, 459–462, 1999.

Goosse, H., H. Renssen, A. Timmermann, R. Bradley, and M. Mann, Using paleoclimate proxy-data to select optimal realisations in an ensemble of simulations of the climate of the past millennium, *Climate Dynamics, 27*, 165–184, 10.1007/s00382-006-0128-6, 2006.

Gordon, A. L., Interocean Exchange of Thermocline Water, *Journal of Geophysical Research, 91(C4)*, 5037–5046, 1986.

Gregory, S., and D. Noone, Variability in the teleconnection between the El niño Southern Oscillation and West Antarctic climate deduced from West Antarctic ice core isotope records, *Journal of Geophysical Research, 113*, D17110, 2008.

Hall, A., and M. Visbeck, Synchronous Variability in the Southern Hemisphere Atmosphere, Sea Ice, and Ocean Resulting from the Annular Mode, *Journal of Climate, 15* (21), 3043–3057, 2002.

Haug, G. H., D. Gnther, L. C. Peterson, D. M. Sigman, K. A. Hughen, and B. Aeschlimann, Climate and the Collapse of Maya Civilization, *Science, 299* (5613), 1731–1735, 2003.

Hofer, D., 2010, *Simulations of the Last Millenium Using a Comprehensive Climate Model: The Impact of the External Forcing on the Climate*, Ph. D. thesis, Physics Institute, University of Bern.

Hofer, D., C. C. Raible, and T. F. Stocker, Variations of the atlantic meridional overturning circulation in control and transient simulations of the last millennium, *Climate of the Past, 7*, 133–150, 2011.

Holland, M., C. Bitz, E. Hunke, W. Lipscomb, and J. Schramm, Influence of the Sea Ice Thickness Distribution on Polar Climate in CCSM3, *Journal of Climate, 19*, 2398, 2006.

Holmgren, K., W. Karln, S. E. Lauritzen, J. A. Lee-Thorp, T. C. Partridge, S. Piketh, P. Repinski, C. Stevenson, O. Svanered, and P. D. Tyson, A 3000-year high-resolution stalagmitebased record of palaeoclimate for northeastern South Africa, *The Holocene, 9* (3), 295–309, 1999.

Jansen, E., J. Overpeck, K. Briffa, J.-C. Duplessy, F. Joos, V. Masson-Delmotte, D. Olago, B. Otto-Bliesner, W. Peltier, S. Rahmstorf, R. Ramesh, D. Raynaud, D. Rind, O. Solomina, R. Villalba, and D. Zhang, 2007, *Palaeoclimate [in: Climate Change 2007: The Physical Science Basis. Contribution of Working Group I to the Fourth Assessment Report of the Intergovernmental Panel on Climate Change]*, Cambridge University Press, Cambridge, United Kingdom and New York, NY, USA.

Jones, J. M., and M. Widmann, Instrument- and Tree-Ring-Based Estimates of the Antarctic Oscillation, *Journal of Climate, 16*(21), 3511–3524, 2003.

Jones, J. M., and M. Widmann, Atmospheric science: Early peak in Antarctic oscillation index, *Nature, 432*(7015), 290–291, 2004.

Jones, P., K. Briffa, T. Osborn, J. Lough, T. van Ommen, B. Vinther, J. Luterbacher, E. Wahl, F. Zwiers, M. Mann, G. Schmidt, C. Ammann, B. Buckley, K. Cobb, J. Esper, H. Goosse, N. Graham, E. Jansen, T. Kiefer, C. Kull, M. Kttel, E. Mosley-Thompson, J. Overpeck, N. Riedwyl, M. Schulz, A. Tudhope, R. Villalba, H. Wanner, E. Wolff, and E. Xoplaki, High-resolution palaeoclimatology of the last millennium: a review of current status and future prospects, *The Holocene, 19*(1), 3–49, 2009.

Jones, P. D., and M. E. Mann, Climate over past millennia, *Reviews of Geophysics, 42*(2), RG2002, 2004.

Jones, P. D., T. J. Osborn, and K. R. Briffa, The Evolution of Climate Over the Last Millennium, *Science, 292*(5517), 662–667, 2001.

Kalnay, E., M. Kanamitsu, R. Kistler, W. Collins, D. Deaven, L. Gandin, M. Iredell, S. Saha, G. White, J. Woollen, Y. Zhu, A. Leetmaa, B. Reynolds, M. Chelliah, W. Ebisuzaki, W. Higgins, J. Janowiak, K. Mo, C. Ropelewski, J. Wang, R. Jenne, and D. Joseph, The NCEP/NCAR 40-Year Reanalysis Project., *Bulletin of the American Meteorological Society, 77*, 437–472, 1996.

Karoly, D., Southern Hemisphere Circulation Features Associated with El Niño-Southern Oscillation Events., *Journal of Climate, 2*, 1239–1252, 1989.

Keeling, C.D., W. T., 2005, Atmospheric CO2 records from sites in the SIO air sampling network, Trends: A Compendium of Data on Global Change., Carbon Dioxide Information Analysis Center, Oak Ridge National Laboratory, Oak Ridge, Tenn., USA.

Kidson, J. W., Principal Modes of Southern Hemisphere Low-Frequency Variability Obtained from NCEP/NCAR Reanalyses, *Journal of Climate, 12*(9), 2808–2830, 1999.

Kiladis, and Mo, 1998, *Meteorology of the Southern Hemisphere*, Chapter Interannual and Intraseasonal Variability in the Southern Hemisphere. Meteorology Monographs, Vol. 27, No. 49, American Meteorological Society, 307-336.

Kushner, P., I. Held, and T. Delworth, Southern Hemisphere Atmospheric Circulation Response to Global Warming., *Journal of Climate, 14*, 2238–2249, 2001.

Kwok, R., and J. C. Comiso, Southern Ocean Climate and Sea Ice Anomalies Associated with the Southern Oscillation, *Journal of Climate, 15*(5), 487–501, 2002.

Lean, J., J. Beer, and R. Bradley, Reconstruction of solar irradiance since 1610: Implications for climate change, *Geophysical Research Letters, 22*(23), 3195–3198, 1995.

Lefebvre, W., and H. Goosse, Influence of the Southern Annular Mode on the sea ice-ocean system: the role of the thermal and mechanical forcing, *Ocean Science, 1*(3), 145–157, 2005.

Lefebvre, W., H. Goosse, R. Timmermann, and T. Fichefet, Influence of the Southern Annular mode on the sea ice-ocean system, *Journal of Geophysical Research, 109*(C9), C09005, 2004.

Lough, J., 2007, *Climate Change, the Great Barrier Reef: A Vulnerability Assessment*, Chapter Climate and climate change on the Great Barrier Reef, pp. 15–50. Great Barrier Reef Marine Park Authority, Townsville, Australia.

Lutjeharms, J., Three decades of research on the greater Agulhas Current, *Ocean Science Discussions, 3*, 939–995, 2006.

Mann, M. E., M. A. Cane, S. E. Zebiak, and A. Clement, Volcanic and Solar Forcing of the Tropical Pacific over the Past 1000 Years, *Journal of Climate, 18*(3), 447–456, 2005.

Marshall, G. J., Trends in the southern annular mode from observations and reanalyses., *Journal of Climate, 16*, 4134–4143, 2003, December.

Marshall, G. J., Half-century seasonal relationships between the Southern Annular mode and Antarctic temperatures, *International Journal of Climatology, 27*(3), 373–383, 2007.

Marshall, G. J., A. Orr, N. P. M. van Lipzig, and J. C. King, The Impact of a Changing Southern Hemisphere Annular Mode on Antarctic Peninsula Summer Temperatures, *Journal of Climate, 19*(20), 5388–5404, 2006.

Masiokas, M., B. Luckman, R. Villalba, S. Delgado, P. Skvarca, and A. Ripalta, Little Ice Age fluctuations of small glaciers in the Monte Fitz Roy and Lago del Desierto areas, south Patagonian Andes, Argentina, *Palaeogeography, Palaeoclimatology, Palaeoecology, 281*(3-4), 351 – 362, 2009.

Masson, V., F. Vimeux, J. Jouzel, V. Morgan, M. Delmotte, P. Ciais, C. Hammer, S. Johnsen, V. Y. Lipenkov, E. Mosley-Thompson, J.-R. Petit, E. J. Steig, M. Stievenard, and R. Vaikmae, Holocene Climate Variability in Antarctica Based on 11 Ice-Core Isotopic Records, *Quaternary Research, 54*(3), 348 – 358, 2000.

McGregor, S., A. Timmermann, and O. Timm, A unified proxy for ENSO and PDO variability since 1650, *Climate of the Past, 6*(1), 1–17, 2010.

Meehl, G. A., J. W. Hurrell, and H. van Loon, A modulation of the mechanism of the semiannual oscillation in the Southern Hemisphere, *Tellus A, 50*(4), 442–450, 1998.

Mo, K. C., and R. W. Higgins, The Pacific-South American Modes and Tropical Convection during the Southern Hemisphere Winter, *Monthly Weather Review, 126*(6), 1581–1596, 1998.

Montecinos, A., A. Daz, and P. Aceituno, Seasonal Diagnostic and Predictability of Rainfall in Subtropical South America Based on Tropical Pacific SST, *Journal of Climate, 13*(4), 746–758, 2000.

Nakicenovic, N., J. Alcamo, G. Davis, B. de Vries, J. Fenhann, S. Gaffin, K. Gregory, A. Grbler, T. Y. Jung, T. Kram, E. L. La Rovere, L. Michaelis, S. Mori, T. Morita, W. Pepper, H. Pitcher, L. Price, K. Riahi, A. Roehrl, H.-H. Rogner, A. Sankovski, M. Schlesinger,

P. Shukla, S. Smith, R. Swart, S. van Rooijen, N. Victor, and D. Zhou, *IPCC Special Report on Emission Scenarios*, Cambridge University Press, UK. pp 570, 2000.

Neukom, R., J. Luterbacher, R. Villalba, M. Kttel, D. Frank, P. Jones, M. Grosjean, H. Wanner, J.-C. Aravena, D. Black, D. Christie, R. DArrigo, A. Lara, M. Morales, C. Soliz-Gamboa, A. Srur, R. Urrutia, and L. von Gunten, Multiproxy summer and winter surface air temperature field reconstructions for southern South America covering the past centuries, *Climate Dynamics,*, 1–17, 10.1007/s00382-010-0793-3, 2010.

Neukom, R., J. Luterbacher, R. Villalba, M. Kttel, D. Frank, P. D. Jones, M. Grosjean, J. Esper, L. Lopez, and H. Wanner, Multi-centennial summer and winter precipitation variability in southern South America, *Geophysical Research Letters, 37*(14), L14708–, 2010.

Otto-Bliesner, B. L., E. C. Brady, G. Clauzet, R. Tomas, S. Levis, and Z. Kothavala, Last Glacial Maximum and Holocene Climate in CCSM3, *Journal of Climate, 19*(11), 2526–2544, 2006.

Parry, M., O. Canziani, J. Palutikof, P. van der Linden, and C. Hanson, *Contribution of Working Group II to the Fourth Assessment Report of the Intergovernmental Panel on Climate Change*, Cambridge University Press, Cambridge, United Kingdom and New York, NY, USA, 2007.

Pickard, G., and W. Emery, *Descriptive Physical Oceanography, 6th edition*, Pergamon Press, Oxford, England, 1992.

Pollack, H. N., S. Huang, and J. E. Smerdon, Five centuries of climate change in Australia: the view from underground, *Journal of Quaternary Science, 21*(7), 701–706, 2006.

Raible, C. C., C. Casty, J. Luterbacher, A. Pauling, J. Esper, D. Frank, U. Büntgen, A. Roesch, P. Tschuck, M. Wild, P.-L. Vidale, C. Schär, and H. Wanner, Climate Variability-Observations, Reconstructions, and Model Simulations for the Atlantic-European and Alpine Region from 1500-2100 AD, *Climatic Change, 79*, 9–29, 10.1007/s10584-006-9061-2, 2006.

Randall, D., R. Wood, S. Bony, R. Colman, T. Fichefet, J. Fyfe, V. Kattsov, A. Pitman, J. Shukla, J. Srinivasan, R. Stouffer, A. Sumi, and K. Taylor, 2007, *Climate Change 2007: The Physical Science Basis. Contribution of Working Group I to the Fourth Assessment Report of the Intergovernmental Panel on Climate Change*, Chapter Climate Models and Their Evaluation. Cambridge University Press, Cambridge, United Kingdom and New York, NY, USA.

Raphael, M., and M. Holland, Twentieth century simulation of the Southern Hemisphere climate in coupled models. part 1: large scale circulation variability, *Climate Dynamics, 26*(2), 217–228–228, 2006.

Raphael, M. N., A zonal wave 3 index for the Southern Hemisphere, *Geophysical Research Letters, 31*(23), L23212–, 2004.

Raphael, M. N., The influence of atmospheric zonal wave three on Antarctic sea ice variability, *Journal of Geophysical Research, 112*, D12112, 2007.

Rauthe, M., and H. Paeth, Relative Importance of Northern Hemisphere Circulation Modes in Predicting Regional Climate Change, *Journal of Climate, 17*(21), 4180–4189, 2004.

Rayner, N. A., D. E. Parker, E. B. Horton, C. K. Folland, L. V. Alexander, D. P. Rowell, E. C. Kent, and A. Kaplan, Global analyses of sea surface temperature, sea ice, and night marine air temperature since the late nineteenth century, *Journal of Geophysical Research, 108*(D14), 4407, 2003.

Renwick, J. A., Southern Hemisphere Circulation and Relations with Sea ice and Sea Surface Temperature, *Journal of Climate, 15*(21), 3058–3068, 2002.

Renwick, J. A., and M. J. Revell, Blocking over the south pacific and rossby wave propagation, *Monthly Weather Review, 127*(10), 2233–2247, 1999.

Richard, Y., N. Fauchereau, I. Poccard, M. Rouault, and S. Trzaska, 20th century droughts in southern Africa: spatial and temporal variability, teleconnections with oceanic and atmospheric conditions, *International Journal of Climatology, 21*, 873–885, 2001.

Rind, D., The Sun's Role in Climate Variations, *Science, 296*(5568), 673–677, 2002.

Rintoul, S., C. Hughes, and D. Olbers, 2001, *Ocean Circulation and Climate*, Chapter The Antarctic Circumpolar Current System, pp. 271–302. New York : Academic Press.

Roscoe, H. K., and J. D. Haigh, Influences of ozone depletion, the solar cycle and the QBO on the Southern Annular Mode, *Quarterly Journal of the Royal Meteorological Society, 133*(628), 1855–1864, 2007.

Russell, J., K. Dixon, A. Gnanadesikan, R. Stouffer, and J. Toggweiler, The Southern Hemisphere Westerlies in a Warming World: Propping Open the Door to the Deep Ocean, *Journal of Climate, 19*, 6382–+, 2006.

Stammerjohn, S. E., and R. C. Smith, Opposing Southern Ocean Climate Patterns as Revealed by Trends in Regional Sea Ice Coverage, *Climatic Change, 37*, 617–639, 10.1023/A:1005331731034, 1997.

Thompson, D. W. J., and S. Solomon, Interpretation of Recent Southern Hemisphere Climate Change, *Science, 296*(5569), 895–899, 2002.

Thompson, D. W. J., and J. M. Wallace, Annular Modes in the Extratropical Circulation. Part I: Month-to-Month Variability, *Journal of Climate, 13*(5), 1000–1016, 2000.

Thompson, D. W. J., J. M. Wallace, and G. C. Hegerl, Annular Modes in the Extratropical Circulation. Part II: Trends, *Journal of Climate, 13*(5), 1018–1036, 2000.

Thompson, T., J. H. Butler, B. C. Daube, G. S. Dutton, J. W. Elkins, B. D. Hall, D. F. Hurst, D. B. King, E. S. Kline, B. G. Lafleur, J. Lind, S. Lovitz, D. J. Mondeel, S. A. Montzka, F. L. Moore, J. D. Nance, J. L. Neu, P. A. Romashkin, A. Scheffer, and W. J. Snible, 2004, *Halocarbons and other Atmospheric Trace Species, in Climate Monitoring and Diagnostics Laboratory, Summary Report No. 27, 2002-2003, pp. 115-133, edited by R. C. Schnell, A.-M. Buggle, and R. M. Rosson, NOAA CMDL, Boulder, CO, 2004.*, Chapter 5., pp. 115–133. NOAA CMDL, Boulder, CO.

Timmermann, A., L. Menviel, Y. Okumura, A. Schilla, U. Merkel, O. Timm, A. Hu, B. Otto-Bliesner, and M. Schulz, Towards a quantitative understanding of millennial-scale Antarctic warming events, *Quaternary Science Reviews, 29*(1-2), 74 – 85, 2010.

Tonello, M. S., M. V. Mancini, and H. Sepp, Quantitative reconstruction of Holocene precipitation changes in southern Patagonia, *Quaternary Research, 72*(3), 410 – 420, 2009.

Trenberth, K., and K. Mo, Blocking in the Southern Hemisphere, *Monthly Weather Review, 113*, 3, 1985.

Turner, J., J. C. Comiso, G. J. Marshall, T. A. LachlanCope, T. Bracegirdle, T. Maksym, M. P. Meredith, Z. Wang, and A. Orr, Non-annular atmospheric circulation change induced by stratospheric ozone depletion and its role in the recent increase of Antarctic sea ice extent, *Geophysical Research Letters, 36*, L08502, 2009.

Tyson, P., W. Karlen, K. Holmgren, and G. Heiss, The Little Ice Age and medieval warming in South Africa, *South African Journal of Science, 96*, 121–126, 2000.

Uppala, S. M., P. W. Kllberg, A. J. Simmons, U. Andrae, V. D. C. Bechtold, M. Fiorino, J. K. Gibson, J. Haseler, A. Hernandez, G. A. Kelly, X. Li, K. Onogi, S. Saarinen, N. Sokka, R. P. Allan, E. Andersson, K. Arpe, M. A. Balmaseda, A. C. M. Beljaars, L. V. D. Berg, J. Bidlot, N. Bormann, S. Caires, F. Chevallier, A. Dethof, M. Dragosavac, M. Fisher, M. Fuentes, S. Hagemann, E. Hlm, B. J. Hoskins, L. Isaksen, P. A. E. M. Janssen, R. Jenne, A. P. Mcnally, J.-F. Mahfouf, J.-J. Morcrette, N. A. Rayner, R. W. Saunders, P. Simon, A. Sterl, K. E. Trenberth, A. Untch, D. Vasiljevic, P. Viterbo, and J. Woollen, The ERA-40 Re-Analysis, *Quarterly Journal Of The Royal Meteorological Society, 131*(612), 2961–3012, 2005.

van Loon, H., The Half-Yearly Oscillations in Middle and High Southern Latitudes and the Coreless Winter, *Journal of the Atmospheric Sciences, 24*(5), 472–486, 1967.

van Loon, H., and R. Jenne, The Zonal Harmonic Standing Waves in the Southern Hemisphere, *Journal of Geophysical Research, 77(06)*, 992–1003, 1972.

Villalba, R., Tree-ring and glacial evidence for the medieval warm epoch and the little ice age in southern South America, *Climatic Change, 26*, 183–197, 10.1007/BF01092413, 1994.

Villalba, R., M. Grosjean, and T. Kiefer, Long-term multi-proxy climate reconstructions and dynamics in South america (LOTRED-SA): State of the art and perspectives, *Palaeogeography, Palaeoclimatology, Palaeoecology, 281*, 175–179, 2009.

von Gunten, L., M. Grosjean, B. Rein, R. Urrutia, and P. Appleby, A quantitative high-resolution summer temperature reconstruction based on sedimentary pigments from Laguna Aculeo, central Chile, back to AD 850, *The Holocene, 19*(6), 873–881, 2009.

Wanner, H., J. Beer, J. Bütikofer, T. J. Crowley, U. Cubasch, J. Flückiger, H. Goosse, M. Grosjean, F. Joos, J. O. Kaplan, M. Küttel, S. A. Müller, I. C. Prentice, O. Solomina, T. F. Stocker, P. Tarasov, M. Wagner, and M. Widmann, Mid- to Late Holocene climate change: an overview, *Quaternary Science Reviews, 27*(19-20), 1791 – 1828, 2008.

Weijer, W., W. P. M. D. Ruijter, A. Sterl, and S. S. Drijfhout, Response of the Atlantic overturning circulation to South Atlantic sources of buoyancy, *Global and Planetary Change, 34*(3-4), 293 – 311, 2002.

Whitworth, T., Monitoring the transport of the Antarctic Circumpolar Current at Drake Passage, *Journal of Physical Oceanography, 13(11)*, 2045–2057, 1983.

Whitworth, T., and R. G. Peterson, Volume transport of the Antarctic Circumpolar Current from bottom pressure meaurements, *Journal of Physical Oceanography, 15(6)*, 810 – 816, 1985.

Wilson, R., E. Cook, R. D'Arrigo, N. Riedwyl, M. N. Evans, A. Tudhope, and R. Allan, Reconstructing ENSO: the influence of method, proxy data, climate forcing and teleconnections, *Journal of Quaternary Science, 25*(1), 62–78, 2010.

Yeager, S. G., C. A. Shields, W. G. Large, and J. J. Hack, The Low-Resolution CCSM3, *Journal of Climate, 19*(11), 2545–2566, 2006.

Yoshimori, M., C. C. Raible, T. Stocker, and M. Renold, Simulated decadal oscillations of the Atlantic meridional overturning circulation in a cold climate state, *Climate Dynamics, 34*(1), 101–121, 2010.

Yoshimori, M., T. F. Stocker, C. C. Raible, and M. Renold, Externally-forced and internal varibility in ensemble climate simulations of the maunder minimum, *18*, 4253–4270, 2005.

Yuan, X., and C. Li, Climate modes in southern high latitudes and their impacts on Antarctic sea ice, *Journal of Geophysical Research (Oceans), 113*, C06S91, 2008.

Yuan, X., and D. Martinson, The Antarctic Dipole and its predictability, *Geophysical Research Letters, 28*, 3609–3612, 2001.

Erklärung

gemäss Art. 28 Abs. 2 RSL 05

Name, Vorname: Wilmes, Sophie-Berenice

Matrikelnummer: 09-130-139

Studiengang: Climate Sciences
                         Master

Titel der Arbeit: Climate Variability of the Mid and High Latitudes of the Southern
                         Hemisphere in Ensemble Simulations from 1500 to 2000 AD

LeiterIn der Arbeit: Christoph C. Raible
                         Thomas F. Stocker

Ich erkläre hiermit, dass ich diese Arbeit selbständig verfasst und keine anderen als die angegebenen Quellen benutzt habe. Alle Stellen, die wörtlich oder sinngemäss aus Quellen entnommen wurden, habe ich als solche gekennzeichnet. Mir ist bekannt, dass andernfalls der Senat gemäss Artikel 36 Absatz 1 Buchstabe o des Gesetzes vom 5. September 1996 über die Universität zum Entzug des auf Grund dieser Arbeit verliehenen Titels berechtigt ist.

Bern, 29. August 2011

Unterschrift